TECHNISCHE
UNIVERSITÄT
WIEN
Vienna, Austria

DISSERTATION

Neutronic modelling of the new TRIGA core and experimental validation

ausgeführt zum Zwecke der Erlangung des akademischen Grades einer Doktorin der technischen Wissenschaften unter der Leitung von

Ao. Prof. Dipl.-Ing. Dr. techn. Helmuth Böck
Atominstitut, Technische Universität Wien
und
Dipl.-Ing. Dr. techn. Mario Villa
Atominstitut, Technische Universität Wien

eingereicht an der Technische Universität Wien
Fakultät für Physik
von

Marcella Cagnazzo
Matrikelnummer: 01229634
marcella.cagnazzo@tuwien.ac.at

To Giulia and Niccolo',

my children, who arrived during the course of this work.

Abstract

One of the key issues concerning the design and management of new generation nuclear power plants and research reactors and related fuel cycles is the development of flexible computational methods for determining the critical parameters of the cores (such as excess of reactivity, shut-down margin, reactivity coefficients, etc.), the distribution of neutron fluxes and the time evolution of nuclear fuel composition (production and depletion of uranium, plutonium and minor actinides, kinetics of saturable and unsaturable poisons, etc.).

The flexibility of the methodology is of paramount importance in order to allow to study nuclear reactors that present a wide variability of core geometries, structural materials' compositions, fuel composition and neutron energy spectra.

In this regard, the primary objective of this Ph.D. Thesis is to develop a methodology, based on the use of Monte Carlo codes, for the evaluation of the above-mentioned parameters and quantities and validate it by benchmarking the results of the calculations with direct measurements. A second objective of this Ph.D. Thesis is to estimate, using the validated methodology, the time-evolution of the fuel composition in the TRIGA Mark II reactor of TU Wien.

In specific, the Research Project focused on the evaluation of the following parameters and quantities:

1) the neutron fluxes distribution in- and out-core;
2) the critical parameters such as core excess of reactivity, shut-down margin and control rods reactivity worth;
3) the transmutation rates (production and depletion) of nuclides relevant for the study and analysis of the time-evolution of the nuclear fuel composition under irradiation, focusing on major and minor actinides and on fission products.

Measurements are performed to obtain a substantial set of data to benchmark Monte Carlo calculations on both neutron flux distributions and transmutation rates. The measurement are carried out in order to:

(a) map the neutron fluxes and related energy distributions in-core (along both vertical and radial axes) and out-core positions (from the Lazy Susan facility to one horizontal beam tube) at the TRIGA Mark II reactor of TU Wien; the measurements were performed using a method based on activation of different material foils followed by a flux de-convolution analysis using the iterative code SAND II;

(b) determine, by means of gamma-ray spectrometry, the neutron-induced transmutation rates in natural uranium and thorium target foils after irradiation in one of the positions characterized in (a);
(c) detect the activity distribution of fission products along the axial dimension of irradiated fuel elements (FEs) at the TU Wien TRIGA reactor; the activity distribution is measured by means of a fuel gamma scanning device and different fission products are detected (self-absorption coefficients and geometric efficiencies are evaluated by means of Monte Carlo calculation performed using the MCNP6 code).

The results of the measurements are used to benchmark different Monte Carlo computation models developed using MCNP6 code and Serpent-2 code. The validation procedure is as follows:

(d) The MCNP6 model and the Serpent-2 model for the new LEU (Low Enriched Uranium) core of the TRIGA Mark II reactor of TU Wien are developed and calculations for neutron fluxes distributions are performed in correspondence of the experimentally characterized positions (a). The validation of the MCNP6 and Serpent-2 reactor models are performed based on the good agreement between the calculations and the measurements of the neutron flux distributions and related neutron energy spectrum across the reactor.
(e) The MCNP6 and Serpent-2 validated models are used to calculate the neutron fluxes and energy spectra in other positions of the reactor core, including inside the FEs, other than those where measurements are performed.
(f) The Serpent-2 model is used to calculate the neutron-induced transmutation rates in uranium and thorium target foils and in irradiated fuel elements (FEs) under the same irradiation conditions of the measurements performed respectively in (b) and (c); the good agreement between calculation and measurement results validates the methodology for the evaluation of the burn-up of the FEs.
(g) Serpent-2 reactor model is additionally used to evaluate the critical parameters of the first LEU core configuration of the TU Wien TRIGA reactor which show a good agreement with the experimental values available from the reactor historical data sheets.

Kurzfassung

Eines der zentralen Themen der Auslegung und des Betriebes von Kernkraftwerken inklusive deren Brennstoffzyklus, ist die Entwicklung flexibler, computerbasierter Methoden, um die kritischen Parameter des Kernes (z.B.. Überschuss- und Abschalt-Reaktivität, Reaktivitätskoeffizienten, etc.), die räumliche Verteilung des Neutronenflusses, sowie die zeitliche Entwicklung der nuklearen Brennstoffzusammensetzung (Produktion und Verbrauch von Uran, Plutonium und weiterer Aktiniden, Kinetik gesättigter und ungesättigter Neutronengifte, etc.) zu bestimmen.

Dabei ist die Flexibilität dieser Methodik von zentraler Bedeutung, um die Entwicklung von Reaktoren, die sich in ihrer Kerngeometrie, in der Materialzusammensetzung, der Komponenten, der Zusammensetzung des Brennstoffes oder in ihren Neutronenenergiespektren unterscheiden können, zu ermöglichen.

Dementsprechend ist das Hauptziel dieser Dissertation, eine auf verschiedenen Monte Carlo Codes basierende Methodik auszuarbeiten, die es ermöglicht, die oben genannten Parameter und Größen zu ermitteln und die Resultate der Berechnungen mit direkten Messungen zu validieren.

Der zweite Schwerpunkt dieser Dissertation liegt darin, mit der validierten Methode, die zeitliche Entwicklung der Brennstoffzusammensetzung des TRIGA MARK II der TU Wien zu berechnen.

Dabei konzentriert sich diese Arbeit auf folgende Parameter:

1) Neutronenflussverteilung innerhalb und außerhalb des Kernes
2) Kritische Parameter wie Überschuss- und Abschalt-Reaktivität sowie die Reaktivitätswerte der Absorberstäbe
3) Umwandlungsraten (Auf- und Abbau), der für die Analyse der zeitlichen Entwicklung der Brennstoffzusammensetzung unter Bestrahlung wichtiger Nuklide, mit Augenmerk auf zeitliche Veränderung von Aktiniden und Zerfallsprodukte.

Die Monte Carlo Berechnungen der Umwandlungsraten und der Neutronenflussverteilungen wurden mit experimentell ermittelten Datensets verglichen, dazu wurden folgende Messungen vorgenommen.

(a) Bestimmung der Neutronenflüsse und der damit verbundenen Energieverteilung innerhalb des Reaktorkernes (sowohl vertikal als auch radial) und an Positionen außerhalb der Kernes (wie zB Probendrehkranz und horizontalem Strahlenrohr) des TRIGA MARK II Reaktors. Die Messungen wurden unter Verwendung der Folien-

Aktivierungsmethode und anschließender Flussentfaltung mit dem iterativen SAND II Code, durchgeführt;

(b) Ermittlung der neutroneninduzierten Umwandlungsraten in Uran- und Thorium-Folien nach der Bestrahlung in den unter (a) beschriebenen Positionen durch Gammaspektroskopie;

(c) Messung der Aktivitätsverteilung von Spaltprodukten entlang der axialen Ebene der bestrahlten Brennelemente am TRIGA Reaktor. Die Aktivitätsverteilung wurde mit einer vorhandenen Scanning Anlage für TRIGA Brennelemente untersucht und damit verschiedene Spaltprodukte analysiert. Die Evaluierung der Selbstabsorptionskoeffizienten und geometrischen Koeffizienten erfolgt durch Monte Carlo Analyse mit dem MCNP6-Code.

Die Ergebnisse der experimentellen Daten wurden zur Validierung verschiedener Monte Carlo Berechnungsmodellen unter Verwendung von MCNP6 und Serpent-2 herangezogen. Die Validierung erfolgt in folgenden Schritten:

(d) Nach Vorliegen der neuen MCNP6 und Serpent-2 Modelle des neuen LEU TRIGA Reaktorkernes erfolgten die Berechnungen für die Neutronenflussverteilungen an den experimentell festgelegten Positionen wie in (a) beschrieben.

(e) Anschließend wurden die verifizierten MCNP6 und Serpent-2 Modelle dazu verwendet, die Neutronenflüsse und Energiespektren in den restlichen Positionen im Kern zu bestimmen. Die Methodik wurde auch für den Bereich innerhalb der Brennelemente angewendet, da dort keine Messungen durchgeführt werden können.

(f) Das Serpent-2 Modell ermöglicht es, die neutroneninduzierten Umwandlungsraten in Uran- und Thoriumfolien und Brennelementen zu berechnen. Diese wurden unter denselben Bedingungen, wie auch bei den Messungen (b) und (c), bestrahlt. Die gute Übereinstimmung zwischen Theorie und Experiment erlaubt es, diese Methode auch zur Bestimmung des Abbrandes der Brennelemente anzuwenden.

(g) Zusätzlich wird das Serpent-2 Reaktormodell herangezogen, um die kritischen Parameter der ersten LEU-Kernkonfiguration des TRIGA MARK II Reaktors zu bestimmen. Diese weisen eine sehr gute Übereinstimmung mit den zur Verfügung stehenden historischen Reaktordaten auf.

Content

Introduction

The present thesis develops a methodology, based on the use of Monte Carlo codes and validated on experimental data, to determine the critical parameters of nuclear reactors core, such as excess of reactivity, shut-down margin, reactivity coefficients, etc.. It includes the distribution of the neutron flux and the time evolution of nuclear fuel composition, such as production and depletion of uranium, plutonium and minor actinides, kinetics of saturable and not-saturable poisons, etc..

At the Technische Universität Wien (TU Wien) a TRIGA Mark II research reactor with thermal power of 250kW, is operated. In this work, the reactor is modelled by two Monte Carlo computation codes, the MCNP6 and the Serpent-2 codes. Additionally, measurements are performed at the reactor to obtain a substantial set of data to benchmark Monte Carlo calculations on both neutron flux distributions and transmutation rates.

This thesis is divided into five chapters:

- Chapter 1 represents a summary of the main concepts about nuclear reactors and their parameters that are of interest for the performed work. It includes a description of the main reactor categories and, in particular, of the TRIGA reactor as reference for the reactor Monte Carlo modelling described in the next chapters.
- Chapter 2 describes the experimental procedure and presents the results of the measurement of the neutron fluxes and their energy distribution. The measurements were performed adopting a method based on activation of different material foils followed by a flux de-convolution analysis using the iterative code SAND II. Several positions were characterized both in-core (along vertical and radial core axes) and out-core (extending from the reflector to one of the horizontal beam tubes). Neutron fluxes and neutron energy distribution results obtained are used as data base for the validation of the Monte Carlo calculation models.
- Chapter 3 describes the implementation of a new model of the TRIGA reactor using the MCNP6 code and its validation against the experimental data reported in Chapter 2. The comparison of calculated and experimental results is discussed and an evaluation is performed about the MCNP6 reactor model capability to reproduce the reactor parameters, such as the neutron flux and the neutron spectrum.

- Chapter 4 describes the experiments conducted at the TRIGA reactor in order to estimate the transmutation rates of nuclides relevant for the study and analysis of nuclear fuel composition under irradiation. The first experiment was a dedicated irradiation of target foils containing these nuclides and consequent determination of the transmutation rates by means of the gamma-ray spectrometry technique. The second experiment consisted in the detection of fission product activity distribution along the vertical axis of the fuel elements (FEs) irradiated during the operation of the TRIGA reactor. Both experiments provided a data set of experimental results useful for the validation of the new TRIGA reactor model developed in the next chapter by means of the Serpent code.
- Chapter 5 describes the utilization of the Serpent-2 Monte Carlo calculation code to implement a new model for the TRIGA reactor and the procedure for its validation. Experiments performed in Chapters 2 and Chapter 4 respectively for neutron spectrum evaluation and burn-up determination are reproduced with Serpent. The results are compared both with experiments and with MCNP6 calculated results (Chapter 3). The validated Serpent reactor model is then utilized to reproduce the core parameters measured in occasion of the first criticality reached with the fully converted LEU (Low Enriched Uranium) core at the TRIGA reactor.

In summary, in the present academic work, the TRIGA Mark II reactor was modelled by the MCNP6 and the Serpent-2 codes and the model were successfully validated against experimental data. This study was necessary as in 2012 the TRIGA reactor core was completely refurbished with new Low Enriched Uranium (LEU) fuel elements, which had an important impact on all reactor parameters.

Chapter 1

Nuclear reactors fundamentals

This Chapter represents a summary of the main concepts about nuclear reactors and their processes that are of interest for the work performed during the present PhD project.
After a recall about nuclear fission reaction (see 1.1) characteristics, the nuclear reactor physics fundamentals and nuclear reactor kinetics (see 1.2) are described.
The following paragraph (see 1.3) is dedicated to the fuel burn-up definition and discussion. This includes the description of fuel modification during reactor operation, the depletion-transmutation equations, as well as the effects of fuel burn-up and of fuel poisoning during the reactor operation.
As different classification for nuclear reactors are possible, the main reactor categories will be presented (see 1.4), as thermal, fast and breeding reactors.
Finally, as the experimental part of the present PhD work was conducted at the TRIGA MARK II reactor of Technische Universität Wien (TU Wien), the TRIGA research reactor will be described with its distinguishing characteristics. The reactor description is of interest as reference in the reactor modelling performed by means of both MCNP (see Chapter 3) and Serpent (see Chapter 5) Monte Carlo codes.

1.1. Nuclear fission

1.1.1. Fission reaction

The fission reaction is the fundamental process in which a heavy nucleus splits into two lighter nuclei, with release of energy and emission of gamma-rays and neutrons [1].

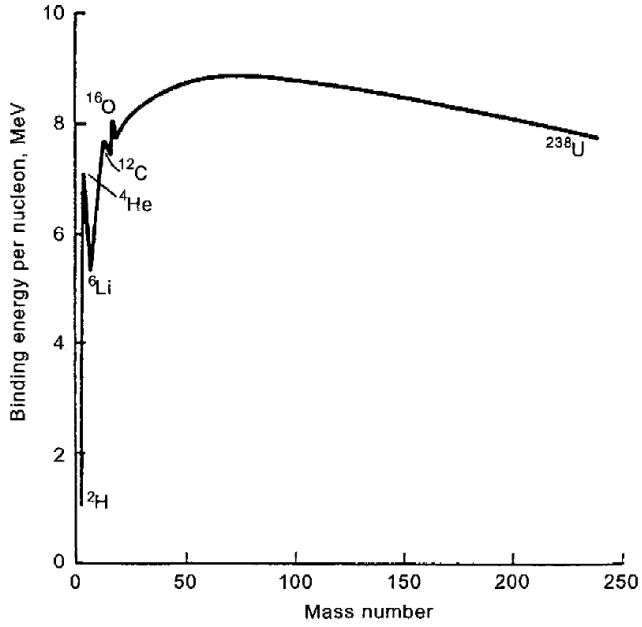

Figure 1. 1: Binding energy per nucleon as a function of mass number [2].

Even if certain heavy nuclei undergo spontaneous fission (i.e. without any externally supplied excitation energy), for application of the fission process in nuclear reactors, here we consider the neutron induced fission.

Considering that the mass of each nucleus (M_A) is slightly lower than the sum of the masses of all neutrons (M_n) and protons (M_p) in the nucleus, the *mass defect* (Δ) is defined as:

$$\Delta = ZM_p + NM_n - M_A$$

The mass defect expressed in energy unit correspond to the *binding energy*, that is the energy needed to break the nucleus into its nucleons [2]. Thus, a process that converts nuclides into another configuration with higher binding energy per nucleon will result in the conversion of mass into energy. The behaviour of the binding energy as a function of the atomic number A is shown in Figure 1.1: the nuclei that present a high binding energy are particularly stable, while a lower binding energy indicates that nuclei can be divided more easily. In the region above A = 50, the curve has a decreasing trend for increasing of A; when A becomes large, a more stable condition is reached if the nucleus splits into two parts. This is the case for the fissile nuclide, like U-235: the fission process causes a gain in the binding energy of the system and this energy represents the energy source in nuclear reactors.

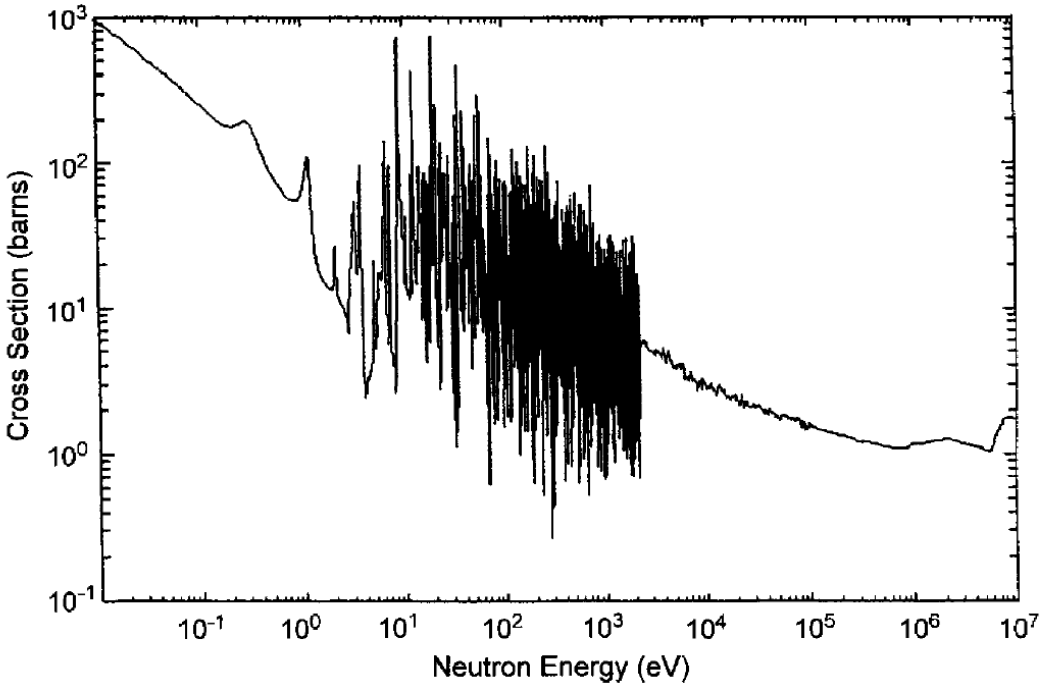

Figure 1. 2: Fission cross section for U-235 [2].

Fissile nuclides can undergo fission by the absorption of a neutron. The probability that a neutron induces fission is related to the fission cross section (σ_f) for the particular nuclide. As an example, Figure 1.2 shows the fission cross section of U-235: as σ_f is larger in the thermal energy region, it is clear that a thermal neutron will be more likely to induce fission on U-235.

1.1.2. Mass distribution

As a consequence of the fission of heavy mass nuclides, several different nuclides (fission products) are formed, but the distribution of these fission fragments is maximum in the mass ranges 90 <A < 100 and 135 <A < 145, as shown in Figure 1.3[1]. The majority of the fission products are not stable and decay, toward stability configuration: several decay steps can be required to reach a stable isotope.

Typically in a fission event, two or three neutrons are emitted promptly (i.e. at the same time of the fission products), and one or more neutrons appear later, subsequently upon the decay of neutron-rich fission fragments over the next second or minutes.

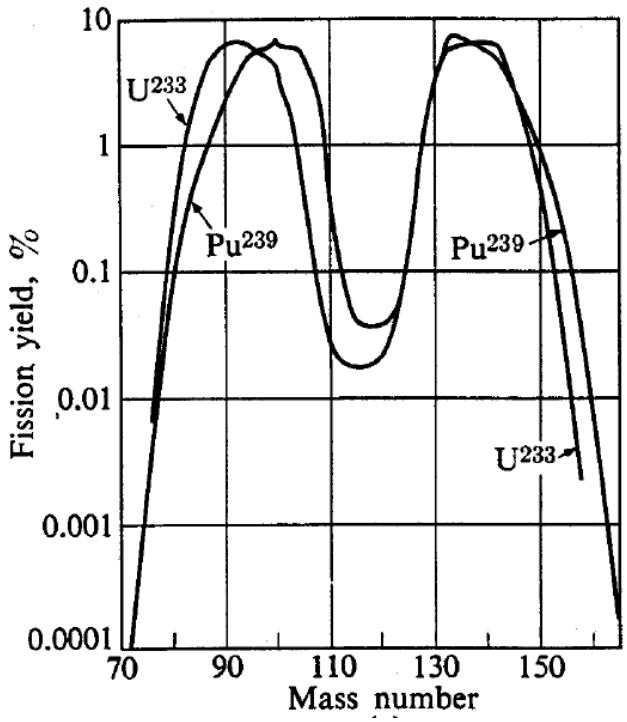

Figure 1. 3: Fission product yield for the thermal fission of U-233 and Pu-239 [1].

The number of neutrons (v) which, on average, are emitted in the fission process depends on the fissile nuclide and on the energy of the neutron inducing fission.

1.1.3. Energy release

The total released energy (E_e) in a fission event is in general different from the recoverable energy (E_r), that can be available in a reactor for the production of thermal energy.

Taking as a reference U-235, E_e correspond to 207 MeV, where the dominant part is the kinetic energy (168 MeV) of the two fission products.

From the decay of the fission fragments, additional kinetic energy is generated: about 8 MeV from electrons, 7 MeV from gammas and 12 MeV from neutrinos. Since neutrinos rarely interact with matter, the neutrino energy is lost.

The prompt neutrons released in the fission event also bring 5 MeV of kinetic energy and are distributed in energy as shown in Figure 1.4, with a maximum at energy of 0.7 MeV. A fraction of these neutron absorption events result in neutron capture followed by gamma emission, producing energy for 3-12 MeV.

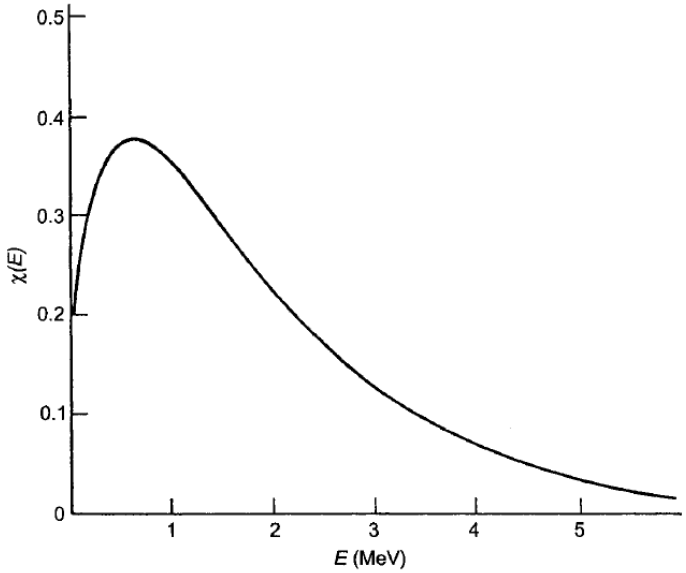

Figure 1. 4: Fission spectrum for thermal neutron induced fission in U-235 [2].

Direct gamma rays emission from fission is responsible for about 7 MeV energy release. Total and recoverable energies are shown in Table 1.1 for U-235 [1].
Thus, in one fission event, about 200 MeV of heat energy is produced.
One Watt of heat energy then corresponds to the fission of 3.1 x 10^{10} nuclei per second. In 1 g of any fissile nuclide there are about 2.5 x $l0^{21}$ nuclei, then the fission of 1 g of fissile material produces about 1 Megawatt-day (MWd) of thermal energy.

1.2. Reactor physics fundamentals and kinetics

As mentioned above, more than one neutron is emitted during a fission reaction. These neutrons, in a proper environment, can induce other fissions and subsequent release of more neutrons (Figure 1.5). This sequence is called chain reaction and is the process that governs nuclear reactors. The essential features of nuclear reactor kinetics[1] are recalled in the present paragraph.

1.2.1. Prompt and delayed neutrons

Among the products of fission there is a certain number (different from fission to fission) of neutrons, called *prompt neutrons*, produced within about 10^{-17} seconds of the fission. The average number of neutrons released per fission (ν) depends

	E_e (MeV)	E_r (MeV)
Fission fragments	168	168
Fission fragments - electrons - gammas - neutrinos	 8 7 12	 8 7 -
Prompt gammas	7	7
Fission neutrons (prompt)	5	5
Capture gammas	-	3-12
Tot	207	198-207

Table 1.1: Emitted (E_e) and Recoverable (E_r) energies for the fission of U-235.

on the fissile nuclide and on the incident neutron energy, increasing almost linearly with energy.

In addition, after a fission event, the decay of the fission products leads to the production of a small number (<1% of fission neutrons) of neutrons: they are called *delayed neutrons* and play an important role in the operation of a reactor. The number of delayed fission neutron with respect to the total number of emitted neutrons is called *total delayed fraction* (β). β value depends on the fissile isotope and incident neutron energy: for example, in thermal fission on U-235, β = 0.0065. Six groups of delayed neutrons, each with its delayed fraction (β_i), are identified and divided based on the half-lives of the fission products that lead to their emission, the so called *delayed neutron precursors*. The *total delayed fraction* (β) can be written as:

$$\beta = \sum_{i=1}^{6} \beta_i \qquad (1.1)$$

1.2.2. Chain reaction and K_{eff} [1, 2]

Due to the emission of two or three neutrons in every fission reaction, there is the possibility to sustain a neutron reaction chain (Figure1.5), when one or more of the neutrons produced survive and produce another fission event. In fact fission neutrons can also be both absorbed in the fuel material or in other non-fuel components, and leak out of the assembly.

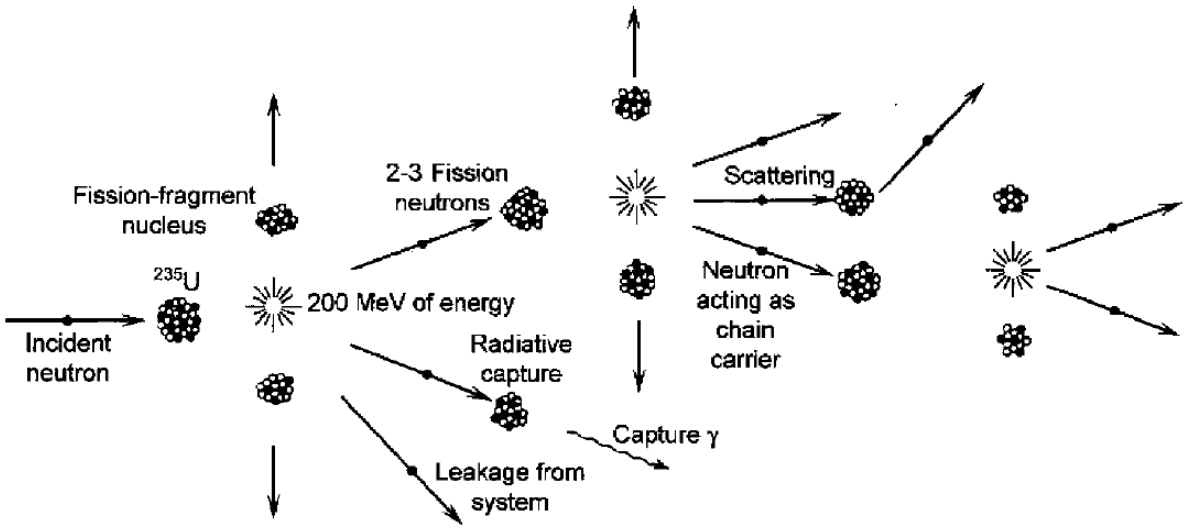

Figure 1. 5: Schematic of a fission chain reaction [2].

For a fissile nuclide, both the fission and the capture cross sections increase (≈l/v) with decreasing the neutron energy. When a neutron is captured in a fissile nuclide, the *fission probability* is $\sigma_f/(\sigma_f + \sigma_c) = 1/(1+ \sigma_c/\sigma_f) = 1/(1+ \alpha)$,where $\alpha=\sigma_c/\sigma_f$ is *the capture-to-fission ratio.*

Then the number of fission neutrons per neutron absorbed in fuel is given as the product of the defined *fission probability* and the average number of neutrons released per fission (ν):

$$\eta = \frac{\nu}{(1+\sigma)} \tag{1.2}$$

This quantity it's typical of a specific fissile nuclide and represents its capability to sustain a fission chain reaction.

To estimate the probability that a neutron is absorbed by a fissile nuclide instead of by another nuclide or leaking from the system, the neutron *thermal utilization factor* is defined as:

$$\frac{absorb\ fissile}{absorb\ fissile+absorb\ other+leak} = \frac{absorb\ fissile}{absorb\ total}\ \frac{1}{(1+leak/absorb\ total)} = f\,P_{NL}$$

where $\boldsymbol{P_{NL}}$ refers to the non-leakage probability and f is the fraction of the absorbed neutrons which are absorbed in the fissile nuclides:

$$f = \frac{N_{fis}\boldsymbol{\sigma}_a^{fis}}{N_{fis}\boldsymbol{\sigma}_a^{fis} + N_{other}\boldsymbol{\sigma}_a^{other}} = \frac{\bar{\boldsymbol{\Sigma}}_a^{fis}}{\bar{\boldsymbol{\Sigma}}_a^{fis} + \bar{\boldsymbol{\Sigma}}_a^{other}} \tag{1.3}$$

In fissile material, the absorption cross section ($\boldsymbol{\sigma}_a^{fis}$) is much greater for thermal neutrons than for fast neutrons; conversely, in non-fissile and structural materials $\boldsymbol{\sigma}_a^{other}$ is comparable for fast and thermal neutrons. Hence, the utilization for a given composition is much greater for thermal neutrons than for fast neutrons.

The product ηf is the number of neutrons produced, on average, from the fission of fissile nuclides for each neutron absorbed in the assembly.

When considering the production of neutrons, one has also to take into account, the possibility that fast neutrons induce fission of some non-fissile fuel nuclides. The *fast fission factor* is then defined as:

$$\varepsilon = \frac{total\ fission\ neutron\ production\ rate}{fission\ neutron\ production\ rate\ in\ fissile\ nuclides} \tag{1.4}$$

Then, $\eta\ f\ \varepsilon$ is the total number of fission neutrons produced fur each neutron absorbed in the assembly, and $\eta f \varepsilon\ P_{NL}$ is the total number of fission neutrons produced, on average, for each neutron introduced into the assembly by a previous fission event.
Lastly, it has to be considered that a fission neutrons can be captured while slowing down to the thermal energy range, due to the capture resonances in the fuel nuclides cross section. The probability that a neutron is not captured during the slowing-down process is referred to as the *resonance escape probability* (*p*).

Effective Multiplication Factor

The quantity $\eta f \varepsilon\ p\ P_{NL}$ is called *effective multiplication factor* of a reactor. It represents the total number of fission neutrons produced, on average, by one fast neutron from a previous fission event:

$$k_{eff} = \eta f \varepsilon p P_{NL} = k_{\infty} P_{NL} \quad (1.5)$$

where k_{∞} refers to the multiplication factor of an infinite reactor with no leakage. If one neutron, on average, is produced to cause another fission, the neutron population remains constant and the condition of the reactor is called *criticality* (k_{eff} = 1). If less than one neutron, on average, is obtained to produce another fission, the neutron population in the reactor will decrease and the condition is referred to as *subcriticality* (k_{eff} < l). If more than one fission neutron, on average, survives to cause another fission, the neutron population in the reactor will increase and the condition is referred to as *supercriticality* (k_{eff} > I).

The k_{eff} depends on the composition (k_{∞}), the size (P_{NL}) of the system and on the arrangement of the materials within the system (*f* and *p*). The composition affects k_{eff} both by the relative number of different nuclides and by the neutron energy distribution. The arrangement of materials determines the spatial neutron distribution, that is the number of neutrons at the locations of the various nuclides.

1.2.3. Reactor Kinetics

If N_0 is the number of fission neutrons into a reactor system at t = 0 and *1* is the average time required for a fission neutron to slow down and be absorbed or leak out, the number of neutrons at time t = *l* is kN_0, while the number of neutrons at time t = *ml* (m integer) is $k^m N_0$.

Typically the value of *1* is about 10^{-4} s for thermal reactors and about 10^{-6} s for reactors in which the fission is produced by fast neutrons[2]. The equation describing the change of the neutron population with time is:

$$\frac{dN(t)}{dt} = \frac{k-1}{l} N(t) + S(t) \quad (1.6)$$

That takes into account the excess of neutron production (by fission), the neutron loss (by absorption or leakage in a neutron lifetime) and any external neutron source S(t) if present. For a constant source, the solution of equation (1.6) is:

$$N(t) = N(0)e^{\frac{(k-1)t}{l}} + \frac{S\,l}{k-1}\left[e^{\frac{(k-1)t}{l}} - 1\right] \quad (1.7)$$

which displays an exponential time behaviour. The reactor *period*[1], representing the variation of neutron population by a factor of "e" results:

$$T = \frac{l}{k-1} \quad (1.8)$$

and provides information on the capability of controlling the fission chain reaction, that is the reactor time behaviour.

For example, considering to increase *k* of 0.1% (from k(0)=1.000 to k=1.001), the period for a thermal reactor will result T = 0.1 s. This is a very short period (in 1 second the neutron population would increase of the equivalent of 10 periods, i.e. of a factor e^{10} = 2.2 x 10^4) and the reactor would be very difficult to control.

In the example above, the reactor period is evaluated without the contribution of the delayed neutrons, that is the neutron generation time is regulated by the prompt neutron life time only. Including the delayed neutrons means in fact increasing considerably the generation time, and the *mean-life* of all neutrons can be written as follows:

$$l = (1-\beta)l_p + \sum_{i=1}^{6}\beta_i\, l_i \quad (1.9)$$

Where l_p is the prompt neutron lifetime and l_i the mean life of a delayed neutron in the i-th group (measured from the instant of fission to the time when it disappears in the system). As the delayed neutrons slow down and are captured in a time much shorter than the mean lifetime of their precursors ($\bar{t}_i$) and $\beta \ll 1$ for all fissile nuclides, the equation1.9 becomes:

$$l \approx l_p + \sum_{i=1}^{6}\beta_i\,\bar{t}_i \quad (1.10)$$

In case of U-235, the term $\sum_{i=1}^{6}\beta_i\,\bar{t}_i = 0.085\ s \approx 0.1\ s$ and again $l_p \approx 10^{-4}$ [1].

For the 0.1% increase in the k value (from k(0)=1.000 to k=1.001), the reactor period evaluated with the delayed neutron according to the equation 1.8, would be T = 0.1/0001=100 s. This value is much greater than what obtained with the prompt neutron only and allows to easily control the reactor by the motion of the control rods. Hence, it results that the delayed neutrons are responsible for the determination of both the mean generation life and the reactor period.

Another important parameter in the reactor kinetics is the reactivity, defined as:

$$\rho = \frac{k-1}{k} \tag{1.11}$$

The reactivity is commonly measured in dollars [$], where 1 $ is defined by the relation 1$= β , with β fraction of delayed neutrons.

1.2.4. Neutron flux

Neutrons produced from fission have relatively high energies (about 2 MeV) and they are called *fast neutrons*. After being emitted, they interact by elastic and inelastic collisions with the fuel and other reactor materials. They then slow down until they reach energy equilibrium with their surroundings: once slowed down, they are named *thermal neutrons* with typically energy of 0.025 eV at 20°C.

A thermal neutron is much more likely to interact with a nucleus than a fast neutron. The effect of the thermal neutrons in the reactor depends on both the number of neutrons (*neutron population*) and their speeds.

A measure of the intensity of the neutron population, is the neutron flux (ϕ). The neutron flux is calculated as $\phi(r) = n(r)v$, being n the neutron density (expressed as neutrons/cm3) and v the neutron velocity (expressed in cm/sec). Consequently, ϕ is measured in neutrons/cm2/sec.

The neutron energy distribution (neutron spectrum) typical of a nuclear reactors is shown in Figure 1.6. Three neutron flux components are usually defined to describe a neutron spectrum:

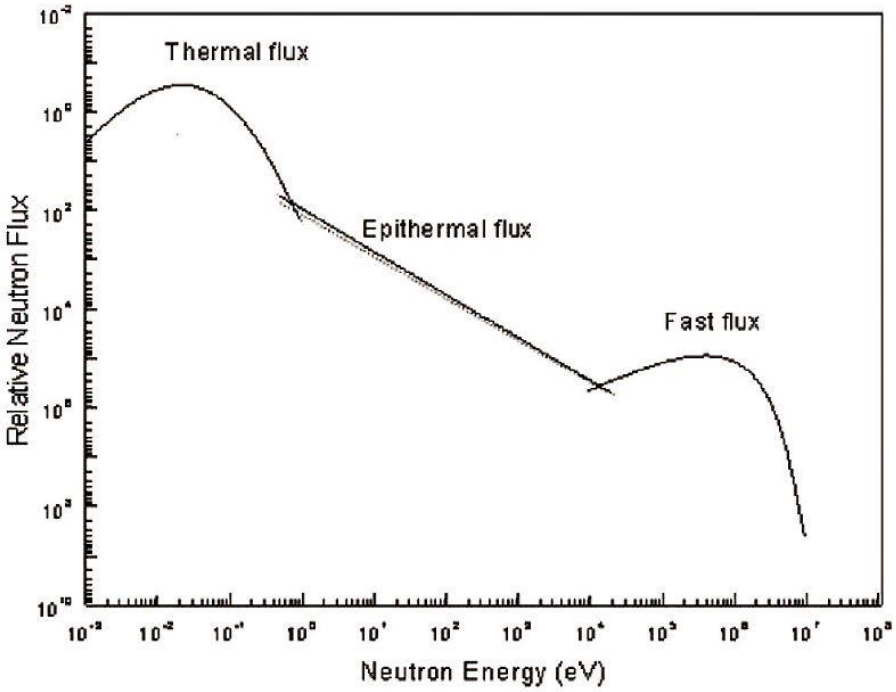

Figure 1. 6: A typical reactor neutron energy spectrum showing the various components used to describe the neutron energy regions.

- Fission or *fast neutrons* component with energy distribution ranges from 100 keV to 25 MeV with a maximum fraction at about 2 MeV. These neutrons are slowed down by interaction with a moderator, to enhance the probability of them causing a fission chain reaction in the 235U.
- The *epithermal neutron* component consists of neutrons with energies from 0.5 eV to 100 keV.
- The *thermal neutron* component consists of low-energy neutrons (below 0.5 eV) in thermal equilibrium with atoms in the reactor's moderator. At room temperature, the energy spectrum of thermal neutrons is best described by a Maxwell-Boltzmann distribution with a mean energy of 0.025 eV and a most probable velocity of 2200 m/s.

1.3. Fuel burn-up and poisoning effects

1.3.1. Burn-up

The changes in the properties of a nuclear reactor over a fuel cycle are determined by the changes in composition due to fuel burnup and the way in which these are compensated[2].

For reactors operating on the uranium cycle, the initial composition of a fuel element contains a mixture of U- 234, U-235 and U-238 developed from the natural uranium: the fissile U-235 percentage varies from 0.72% (for natural uranium) to more than 90%, depending on the enrichment. For reactors operating on the thorium cycle, the initial composition contains instead Th-232 (natural) and U-233 or U-235.

During the reactor operation changes occur in the composition of the fuel. The nuclei in the fuel undergo transmutation by neutron capture and subsequent decay. Transmutation produces, in case of uranium cycle reactors, a variety of transuranic elements in the actinide series of the periodic table; and in case of thorium cycle reactors, a number of uranium isotopes.

In addition, the original fissile isotope (e.g., U-235) abundance decreases with reactor operation. Instead, the neutron transmutation of a fertile isotope (e.g., U-238) produces a fissile isotope (e.g., Pu-239) which in turn can be transmuted by neutron capture (e.g., into Pu-240 and higher actinide isotopes). As an example, the build-up of the various Pu isotopes as a function of fuel burn-up for a typical LWR (Light Water Reactor) is shown in Figure 1.7.

Fuel burnup is a measure of how much energy is extracted from a nuclear fuel and a measure of fuel depletion.

1.3.2. Depletion-Transmutation equations

Time dependent concentrations of the various isotopes in the fuel of a reactor are described by a coupled set of production-destruction equations.

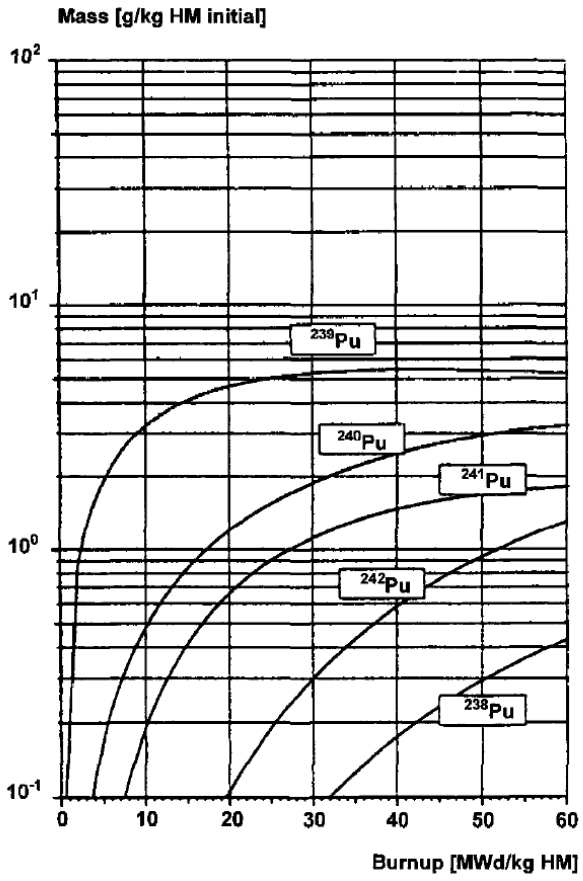

Figure 1. 7: Bild-up of Pu isotopes in a Light Water Reactor (LWR) with 4% enriched Uranium fuel.

For reactors operating on the uranium cycle, the isotopic concentrations are described by equations in Figure 1.8 [2]. A two-digit superscript convention is adopted for isotopes identification: the first digit is the last digit in the atomic number and the second digit is the last digit in the atomic mass. The neutron reaction rate then writes as $\sigma_x^{nm}\varphi n^{nm}$.

In particular, the fission products generated by fission tend to be neutron-rich and undergo radioactive decay. Additionally, they also undergo neutron capture, with cross sections ranging from a few tenths of a barn (1barn = 10^{-24} cm^2) to millions of barns. The general production-destruction equation satisfied by a fission product j can be written as:

$$\frac{dn_j}{dt} = Y_j\overline{\boldsymbol{\Sigma}}_{\boldsymbol{F}}\Phi + \sum_i(\lambda^{i\to j} + \sigma^{i\to j}\Phi)n_i - (\lambda^j + \sigma_a^j\Phi)n_j \qquad (1.12)$$

$$\frac{\partial n^{24}}{\partial t} = -\sigma_a^{24}\phi n^{24}$$
$$\frac{\partial n^{25}}{\partial t} = \sigma_\gamma^{24}\phi n^{24} - \sigma_a^{25}\phi n^{25}$$
$$\frac{\partial n^{26}}{\partial t} = \sigma_\gamma^{25}\phi n^{25} - \sigma_a^{26}\phi n^{26} + \lambda_{ec}^{36} n^{36}$$
$$\frac{\partial n^{27}}{\partial t} = \sigma_\gamma^{26}\phi n^{26} + \sigma_{n,2n}^{28}\phi n^{28} - \lambda^{27} n^{27}$$
$$\frac{\partial n^{28}}{\partial t} = -\sigma_a^{28}\phi n^{28}$$
$$\frac{\partial n^{29}}{\partial t} = \sigma_\gamma^{28}\phi n^{28} - (\lambda^{29} + \sigma_a^{29}\phi) n^{29}$$
$$\frac{\partial n^{36}}{\partial t} = \sigma_{n,2n}^{37}\phi n^{37} - (\lambda^{36} + \sigma_a^{36}\phi) n^{36}$$
$$\frac{\partial n^{37}}{\partial t} = \lambda^{27} n^{27} - \sigma_a^{27}\phi n^{37}$$
$$\frac{\partial n^{38}}{\partial t} = \sigma_\gamma^{37}\phi n^{37} - (\lambda^{38} + \sigma_a^{38}\phi) n^{38}$$
$$\frac{\partial n^{39}}{\partial t} = \lambda^{29} n^{29} - (\lambda^{39} + \sigma_a^{39}\phi) n^{39}$$
$$\frac{\partial n^{48}}{\partial t} = \lambda^{38} n^{38} - \sigma_a^{48}\phi n^{48}$$
$$\frac{\partial n^{49}}{\partial t} = \lambda^{39} n^{39} - \sigma_a^{49}\phi n^{49} + \sigma_\gamma^{48}\phi n^{48}$$

$$\frac{\partial n^{40}}{\partial t} = \sigma_\gamma^{49}\phi n^{49} - \sigma_a^{40}\phi n^{40} + \sigma_\gamma^{29}\phi n^{29} + \sigma_\gamma^{39}\phi n^{39}$$
$$\frac{\partial n^{41}}{\partial t} = \sigma_\gamma^{40}\phi n^{40} - (\lambda^{41} + \sigma_a^{41}\phi) n^{41}$$
$$\frac{\partial n^{42}}{\partial t} = \sigma_\gamma^{41}\phi n^{41} - \sigma_a^{42}\phi n^{42}$$
$$\frac{\partial n^{43}}{\partial t} = \sigma_\gamma^{42}\phi n^{42} - (\lambda^{43} + \sigma_a^{43}\phi) n^{43}$$
$$\frac{\partial n^{51}}{\partial t} = \lambda^{41} n^{41} - (\lambda^{51} + \sigma_a^{51}\phi) n^{51}$$
$$\frac{\partial n^{52}}{\partial t} = \sigma_\gamma^{51}\phi n^{51} - \sigma_a^{52}\phi n^{52}$$
$$\frac{\partial n^{53}}{\partial t} = \lambda^{43} n^{43} - \sigma_a^{53}\phi n^{53} + \sigma_\gamma^{52}\phi n^{52}$$

Figure 1. 8: system of equation to express the modification of fuel isotopic concentrations for reactors operating on the uranium cycle [2].

where Y_j is the fraction of fissions that produces a fission product j, $\lambda^{i\to j}$ is the decay rate of isotope *i* to produce isotope *j*, and $\sigma^{i\to j}$ is the transmutation cross section of the neutron capture reaction that produce isotope *j* from isotope *i*. The last term in equation 1.12 represent the disappearance of any isotope j by radioactive decay or capture reaction.

The equations reported in Figure 1.8 can be integrated to determine composition changes over the lifetime of the reactor core loading if the time dependence of the flux is known. A number of computer codes exist that solve the production-destruction equations for input neutron fluxes.
Nevertheless, the neutron flux distribution depends on the composition (i.e. it is modified during one reactor cycle with fuel burn-up). Hence, the accuracy of the solution depends on Δt_{burn} being chosen so that $(\lambda^j + \sigma_a^j \Phi)\Delta t_{burn} << 1$ for all of the isotopes involved. For this reason, the physical production-destruction equations should be adapted to eliminate short-time-scale phenomena that do not affect the overall result.

The most commonly used measure of fuel burnup is the fission energy release per unit mass of fuel. One Megawatt-day is equal to one Megawatt of power produced by a nuclear reactor over a period of one day.
Therefore fuel burnup of nuclear fuel normally has units of Megawatt-days per metric tonne (MWd/T), where tonne refers to a metric ton of uranium metal. and the Megawatt-day refers to the thermal power of the reactor (not the fraction which is converted to electricity). For example, a reactor with 100,000 kg of fuel operating at 3000MW power level for 1000 days would have a burnup of 30,000 MWd/T.

1.3.3. Burn-up effect in fuel

Several reactivity effects, both negative and positive, are associated with the change in fuel composition.

Among the negative effects, as a consequence of fission reaction, the number of fissile nuclei is reduced and fission products are created, many of which have large neutron capture cross sections. Instead, the transmutation of a fertile isotope into a fissile isotope has a positive reactivity effect. The transmutation of one fertile isotope into another non-fissile isotope can have both a positive or negative reactivity effect, depending on the cross sections for the isotopes involved.

The reactivity effects of fuel depletion must be compensated to maintain the reactor in a critical state over the fuel burnup cycle. The primary way to compensate reactivity effects is to use the control rods: insertion of control rods compensates positive depletion reactivity effects; while withdrawn compensates negative depletion reactivity effects. Another possibility to compensate fuel-depletion reactivity effects is the adjustment of the concentration of a neutron absorber (e.g., boron in the form of boric acid) in the water coolant. Soluble poisons can also be used to compensate fuel-depletion reactivity under certain limits, as they introduce a positive coolant temperature reactivity coefficient.

In general, fuel depletion and the compensating control actions affect the reactor flux and power distribution over a fuel cycle. As a consequence, depletion of fuel will be greatest where the power is higher. The positive reactivity effect will then enhance the power peaking; while the negative reactivity effects will cause the power to shift away to regions with higher k_{eff}.

At a certain time, a reactor core configuration will consist of several batches of fuel elements that have been in the core for different lengths of time. At each refueling, the batch of fuel with the highest burnup is discharged, the batches with lower burnup may be moved to different locations, and a fresh batch is added to replace the discharged one.

The analysis to determine the distribution of the different fuel batches within the core in order to meet the safety and operational (e.g. power distribution, maximum burnup, etc.) constraints of a reactor is known as *fuel management analysis*.

1.3.4. Poisons in nuclear fuel

In a nuclear reactor, same fission products act like poisons due to their great thermal absorption cross section. The poisons are divided into two groups: *saturable* poisons (e.g. Sm-149 and Xe-135) which saturate after a certain reactor operation time; and *non-saturable* poisons which are continuously accumulated during the reactor operation.

Considering an infinite homogeneous reactor, the reactivity associated to poisons in a previously critical reactor state (k) is affected by the thermal utilization factor only and can be written as:

$$\rho = \frac{k^p - k}{k^p} = \frac{f^p - f}{f^p} \tag{1.13}$$

Where k^p and f^p refer to the poisoned reactor. In absence of poison, f is given by equation 1.3. With poisons, this becomes:

$$f^p = \frac{\bar{\Sigma}_a^{fis}}{\bar{\Sigma}_a^{fis} + \bar{\Sigma}_a^{other} + \bar{\Sigma}_a^{p}} \tag{1.14}$$

where $\bar{\Sigma}_a^{p}$ is the macroscopic cross section of the poison. The reactivity due to the poison can be expressed from equation 1.13 as:

$$\rho = \frac{f^p - f}{f^p} = -\frac{\bar{\Sigma}_a^{p}}{\bar{\Sigma}_a^{fis} + \bar{\Sigma}_a^{other}} \tag{1.15}$$

To express this reactivity in a form suitable for calculation of fission product poisoning, the factor $\bar{\Sigma}_a^{fis} + \bar{\Sigma}_a^{other}$ can be deducted by solving the following equation for the multiplication factor of the un-poisoned reactor:

$$k_\infty = 1 = \eta f \varepsilon\, p = \frac{\eta \varepsilon\, p\, \bar{\Sigma}_a^{fis}}{\bar{\Sigma}_a^{fis} + \bar{\Sigma}_a^{other}} = \frac{\nu \varepsilon\, p\, \bar{\Sigma}_F}{\bar{\Sigma}_a^{fis} + \bar{\Sigma}_a^{other}} \tag{1.16}$$

where $\bar{\Sigma}_F$ is the macroscopic fission cross section. The reactivity due to the poison effect can then be calculated as:

$$\rho = -\frac{\bar{\Sigma}_a^p / \bar{\Sigma}_F}{\nu \varepsilon\, p} \qquad (1.17)$$

As an example, we consider the most important fission product poison, that is Xe-135.

Xenon-135 has a thermal absorption cross section of 2.6×10^{-18} cm^2 ($T_{1/2}$=9.1 h). It is produced directly from fission (with yield Y_X), and from the decay of I-135 (λ_I and $T_{1/2}$=6.6 h), which in turn is produced by the decay of the direct fission product Te-135 ($T_{1/2}$=19 s). The Xe-135 (X = Xe-135 concentration in atoms/cm^3) disappears both for radioactive decay (λ_X) and for neutron absorption ($\bar{\sigma}_{a-X}$= average thermal absorption cross section for Xe-135). Then the xenon rate equation can be written as [1] :

$$\frac{dX}{dt} = \lambda_I I + Y_X \bar{\Sigma}_F \varphi_{th} - \lambda_X X - \bar{\sigma}_{a-X} \varphi_{th} X \qquad (1.18)$$

In a reactor $\bar{\Sigma}_F$ and φ_{th} are time dependent, as well as the solution of equation 1.18.

Due to short I-135 and Xe-135 half-lives and to large Xe-135 absorption cross section, the concentration of the two isotopes quickly reaches saturation (equilibrium) values (I_∞ and X_∞ respectively).

When a reactor is shut down, Xe-135 production by fission stops, but the isotope continues to be produced by the decay of I-135. In fact, as it can be seen in Figure 1.9, the xenon concentration increases immediately after shut-down. The maximum of Xe-135 concentration (that corresponds to the maximum negative xenon reactivity) is reached after about 10 hours from shut-down and then decrease to zero. In particular, if a certain time the negative reactivity due to xenon built-up exceeds the positive reactivity given by the extraction of the control rods, the reactor cannot be restarted. This effect is grater for high flux reactors because the Xe-135 accumulation is grater in these reactors.

This is especially true at the end of a reactor fuel cycle when the available *excess of reactivity* may be very small.

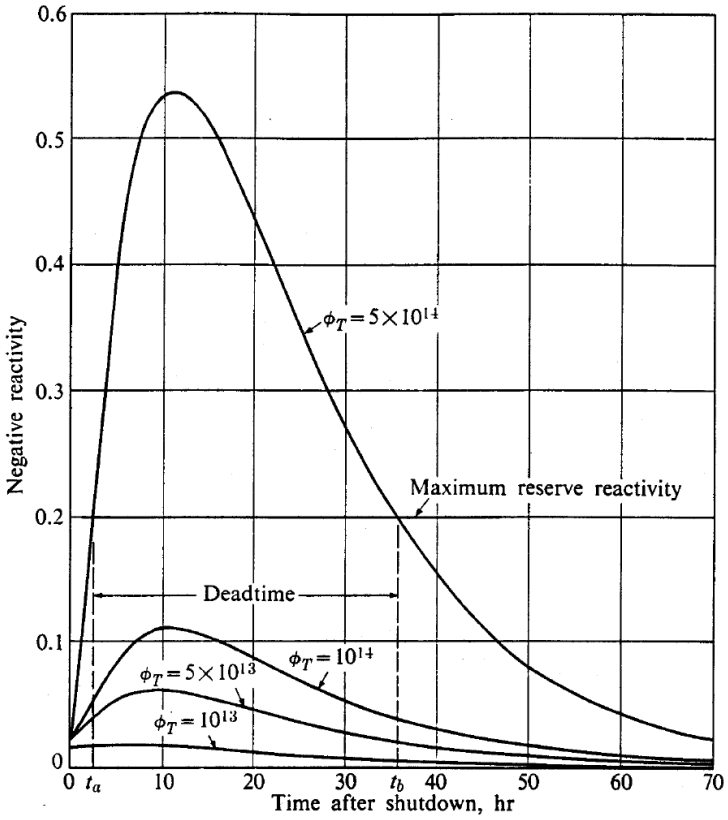

Figure 1. 9: Xe-135 builup after reactor shutdown. Cureves for different flux values before shutdown are shown [1].

1.4. Types of nuclear reactors

1.4.1. Thermal and fast reactors

The main classification of reactor types is done on the basis of differences in the neutron energy distribution, or spectrum. Then it is distinguished among *thermal reactors* and *fast reactors*, corresponding to the majority of the fission reactions involving neutrons in the thermal energy range (E < 1 eV) and to the majority of the neutron nuclear reactions involving neutrons in the fast energy range (E > 1 keV), respectively. Representative neutron spectra for thermal (LWR) and fast (LMFBR) reactor cores are shown in Fig. 1.10.

The majority of reactors up to date are thermal reactors: this is mainly due to the fact that the amount of fissile material needed for reach the criticality is much lower than required for fast reactors.

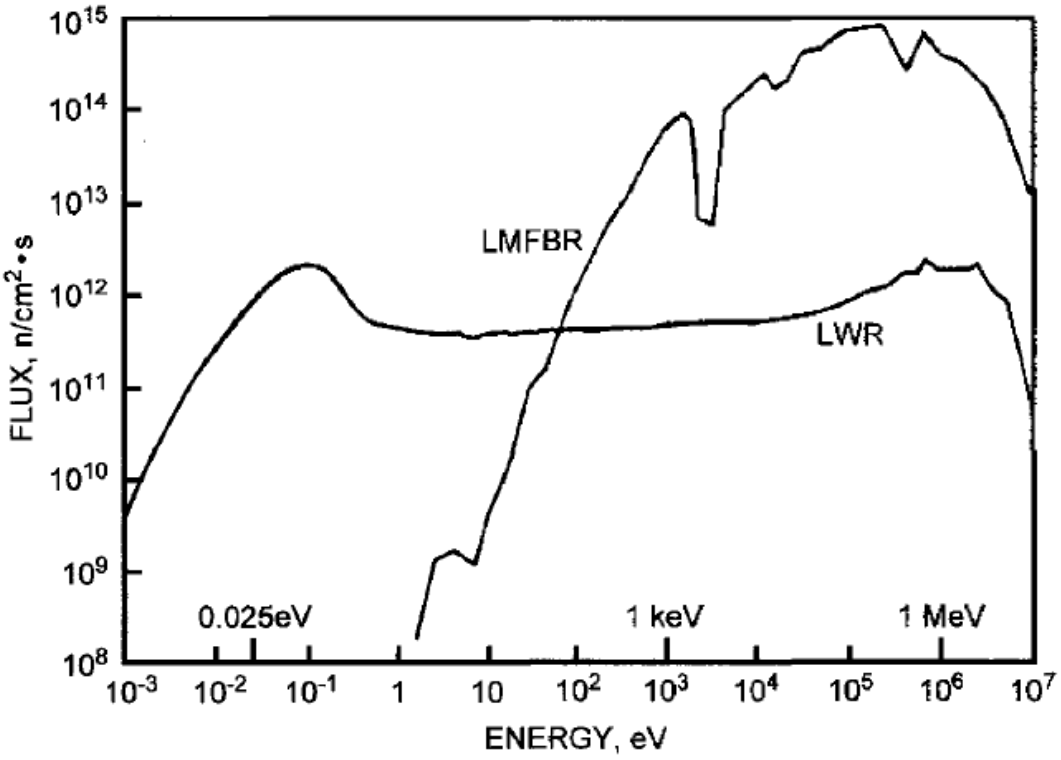

Figure 1. 10: typical neutron spectra for thermal (LWR) and fast (LMFBR) reactor cores [2].

A thermal reactor also presents a lightweight *moderator* material that slows down the fission neutrons; and a *reflector* surrounding the core in order to reduce the leakage of neutrons. On the other side, fast reactors require a large mass of fuel to become critical, do not involve any moderator material and their coolant must not be a lightweight material (to avoid neutron moderation).

1.4.2. Nuclear Power reactors

Nuclear Power reactors, or Nuclear Power Plants (NPPs), in operation at the present time are more than 400 and about 60 new NPPs are under construction. The main types of NPPs are here listed with description of main characteristics:

Pressurized Water Reactors (PWR) represent the majority of NPPs built in the world. They utilize low enriched (2-4%) UO_2 fuel and light water as both coolant and moderator; the pressure vessel (about 160 bars) is kept constant by means of the pressurizer. For long-term reactivity control, coolant (water)

contains boric acid which is gradually removed parallel to uranium consumption (fuel burn-up).

Boiling Water Reactors (BWR), as PWRs, use light water as coolant and moderator, but the pressure in the water-steam cycle is much lower (about 70 bar) and the water is boiling in the core. A steam-water separator is present above the core, then in a BWR the control rods enter the core from the bottom.

Pressurized Heavy Water reactors (PHWR), like CANDU (CANadian Deuterium Uranium reactor), are pressurized reactors that use heavy water (D_2O) as coolant-moderator and UO_2 as fuel. The on-line refuelling is one of the main characteristics of CANDU reactors.

Graphite moderated, Light water cooled, Pressure Tube reactors (RBKM) were developed in the former Soviet Union, originally for military application (Plutonium production). The fuel utilized is slightly enriched uranium, while one characteristic of this type of reactor is the positive void coefficient than affects reactor stability.

Graphite moderated, gas cooled reactors were developed in UK (MAGNOX, AGR) an France (HTR). The efficiency was improved from MAGNOX to AGR by using UO_2 ceramic fuel (about 3-4% enrichment) instead of natural uranium. The coolant is CO_2 in MAGNOX and AGR, and helium in HTR. In HTR, higher gas temperatures (up to 1000°C) are involved in order to increase the thermal efficiency.

Liquid metal fast breeder reactors (LMFBR) present a core surrounded by a blanket in which the extra neutrons diffuse: the breeding process takes place in the blanket (typically composed of depleted U-238). Typical coolant for LMFBR is liquid sodium.

Gas-cooled Fast Reactors (GFR) have not been built so far. Like other helium-cooled reactors, will be high-temperature units (850°C), suitable for power generation, thermochemical hydrogen production or other process heat. Fuel would include depleted uranium and any other fissile or fertile materials. Spent fuel would be reprocessed on site and all the actinides recycled to minimise production of long-lived radioactive wastes.

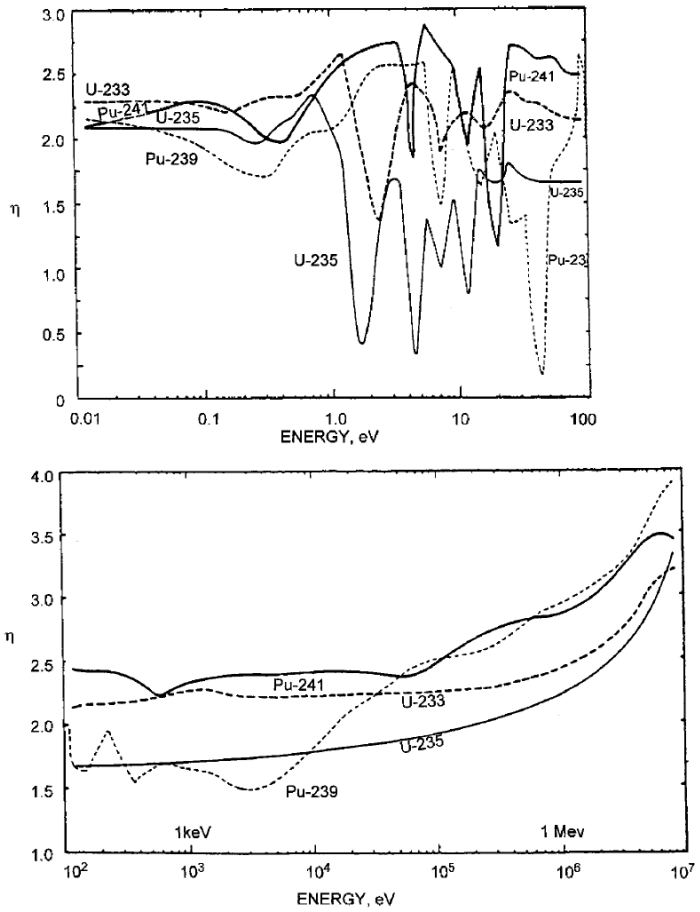

Figure 1. 11: Behaviour of the parameter η for the main fissile nuclei [2].

1.4.3. Breeding reactors

The number of neutrons emitted per neutron absorbed by a fissile nucleus (**η**) is considerably greater than unit and there are some neutron in excess (**η** – 1) of the number of neutron needed to obtain criticality. The excess neutrons can then be used to convert fertile material into fissile isotopes. The transmutation rate of fertile-to-fissile isotopes depends on the available number of neutrons in excess of those needed to maintain the chain fission reaction.

The transmutation rate of fertile-to-fissile isotopes depends on the available number of neutrons in excess of those needed to maintain the chain fission reaction.

The energy dependent behaviour of **η** is shown in Figure 1.11 for the principal fissile isotopes.

For a thermal neutron spectrum (E < 1 eV), U-233 presents the largest value of and the best possibility for fertile-to-fissile conversion in a thermal spectrum is with the Th-232/U-233 fuel cycle. Instead, for a fast neutron spectrum (E > 5 x 10^4 eV), U-238/Pu-239 have the largest values of η of the fissile nuclei.

The instantaneous *conversion ratio* is defined as the ratio of the rate of creation of new fissile isotopes to the rate of destruction of fissile isotopes. When this ratio is greater than unity, it is called *breeding ratio*, and the *breeding reactor* produces more fissile material than it consumes.

It has to be noted that, as it's easy to build reactors that converts fertile into fissile isotopes (η>1), it is much more difficult to build breeding reactors. In fact, in order to breed, for each fission neutron inducing another fission the number of neutrons absorbed by fertile material should be greater than unit. Conversion (or breeding) ratios for various types of reactor are shown in Table 1.2 [2].

Reactor Type	Initial Fuel	Convertion cycle	Convertion Ratio
BWR	2-4 wt% U-235	U-238 ➔ Pu-239	0.6
PWR	2-4 wt% U-235	U-238 ➔ Pu-239	0.6
PHWR-CANDU	U natural	U-238 ➔ Pu-239	0.8
HTR	5 wt% U-235	Th-232 ➔ U-233	0.8
LMFBR	10-20 wt% Pu	U-238 ➔ Pu-239	1.0 – 1.6

Table 1. 2: Conversion (or breeding) ratios for various types of reactor

1.5. TRIGA Mark II reactor

TRIGA[3] (Training, Research, Isotopes production, General Atomics) reactor, produced by General Atomics (GA), is a widely used research nuclear reactor in the world. They are used in several different applications, such as production of radioisotopes for medicine and industry, tumors treatment, non-destructive testing, basic research and for education and training. These reactors operate at thermal power levels from 20 kilowatts to 16 Megawatts, and can be pulsed up to 22 Megawatts. The high power pulsing is possible due to the unique properties of TRIGA uranium-zirconium hydride fuel, which provides this reactor with a real "inherent safety" behavior. Starting from the 50s, more than 60 TRIGA reactors were installed at universities, government and industrial laboratories, and medical centers in 24 countries.

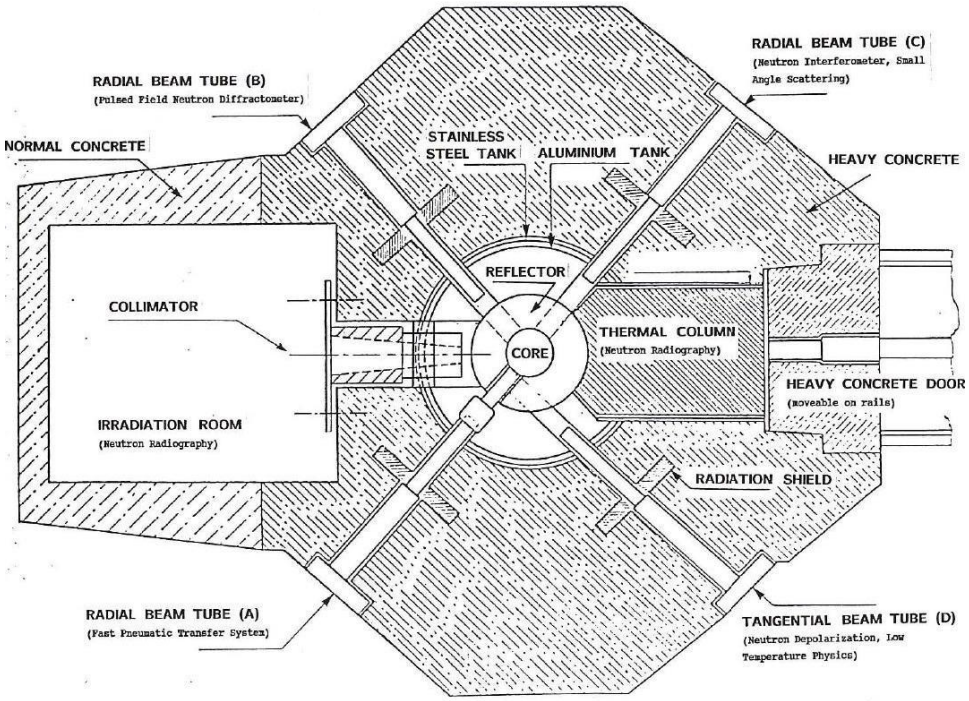

Figure 1. 12: Horizontal section of the TRIGA Mark II Reactor at TU Wien.

One of these reactors was installed at the Technische Universität Wien (TU Wien) and achieved its first criticality on March 7, 1962. As the TRIGA reactor at TU Wien was used to perform the experimental part of the present doctorate project, it will be here described in detail.

1.5.1. TRIGA Mark II reactor at TU Wien

The TRIGA MARK II reactor [4, 5, 6] of the TU Wien is a pool-type research reactor moderated and cooled by light water, licensed for 250 kW steady state and up to 250 MW pulse operation.

At the beginning of the present doctorate project, the reactor was converted from a highly heterogeneous core, which included HEU (High Enriched Uranium) fuel elements, to a full LEU (Low Enriched Uranium) core. As a result, the current core load consists out of 76 stainless steel clad zirconium-hydride fuel elements (8.5%-wt enriched 19.95%-wt in U-235), in a cylindrical geometry.

The reactor is equipped with various irradiation facilities inside and outside the reactor core. It incorporates facilities for neutron and gamma irradiation studies as well as for isotopes production, samples activation and students training.
The horizontal section of the reactor is shown in Figure 1.12 where the reactor core, the graphite reflector, the four horizontal beam tubes, the thermal column, the thermalizing column (that incorporate the neutron collimator), the reactor tank and the biological shield in concrete are displayed.

The four beam tubes (i.e. A, B, C and D) penetrate the biological shield and the aluminium tank reaching reactor reflector. These tubes provide both irradiation facilities for large specimen (up to 15 cm) in a region close to the core; and neutron beams and gamma radiation for experiments installed externally to the biological shielding.

Since its start-up, the reactor operates on average about 220 days per year, without any long outages. The heat produced is dissipated by means of a primary and secondary cooling system. They are separated by a heat exchanger: while the primary circuit is filled with de-ionized, distilled water at temperature between 20 to 40 degrees Celsius; the secondary circuit works with ground water at temperatures between 12 and 18 degrees Celsius.

Among the FE(s), two are instrumented FE(s), that means they have thermocouples in the fuel meat which to allow the measure the fuel temperature during reactor operation. Typically, the fuel temperature at nominal power (250 kW) is about 200 ^{o}C. Three control rods (Regulating, Shim and Transient-safety), made of boron carbide as absorber material, control the power level of the TRIGA reactor.

On the reactor top, the reactor core can be directly observed through a 5 m vertical water shield.
The main components of the reactor are displayed in Figure 1.12 and Figure 1.13, and are now described in detail.

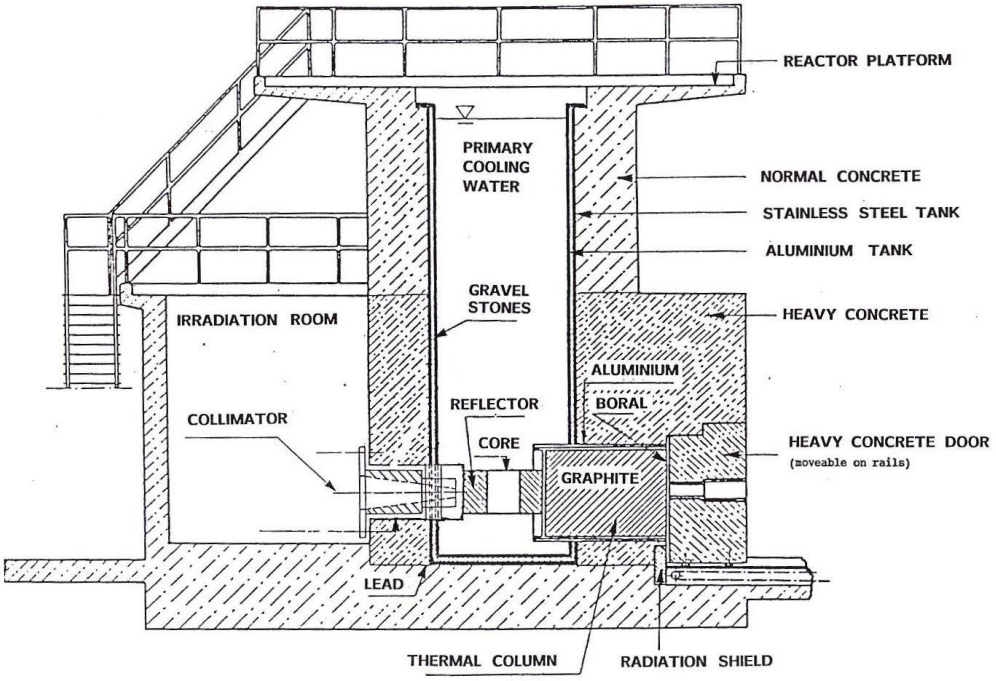

Figure 1. 13: Vertical section of the TRIGA Mark II Reactor at TU Wien.

1.5.2. Reactor core components

The reactor core is placed 60 cm from the bottom of the tank. About 4.9 meters of water above it act as vertical screen; in addition, in the radial direction, it is shielded by 30.5 cm of reflector graphite, 45.7 cm of tank water and a minimum of 2.3 meters of ordinary cement (2.3 g / cm^3).

The geometry of the core is characterized by cylindrical symmetry: together with the reflector, it forms a cylinder of about 1.09 meters in diameter and 58 cm high.

The core consists of a lattice of elements (90 positions available for fuel, graphite elements, control rods and irradiation channels) arranged on five concentric rings, around the central channel (Figure 1.14).

In the first ring (B) there are 6 fuel elements; in the second ring (C) there are a total of 12 positions, 11 filled with fuel and one with a control rod (SHIM); in the third ring (D) there are 18 positions, of which 17 with fuel and one with a second control rod (TRANS = transient); in the fourth ring (E) 24 positions are available, of which 23 of fuel and one with the 3rd control rod (REG =

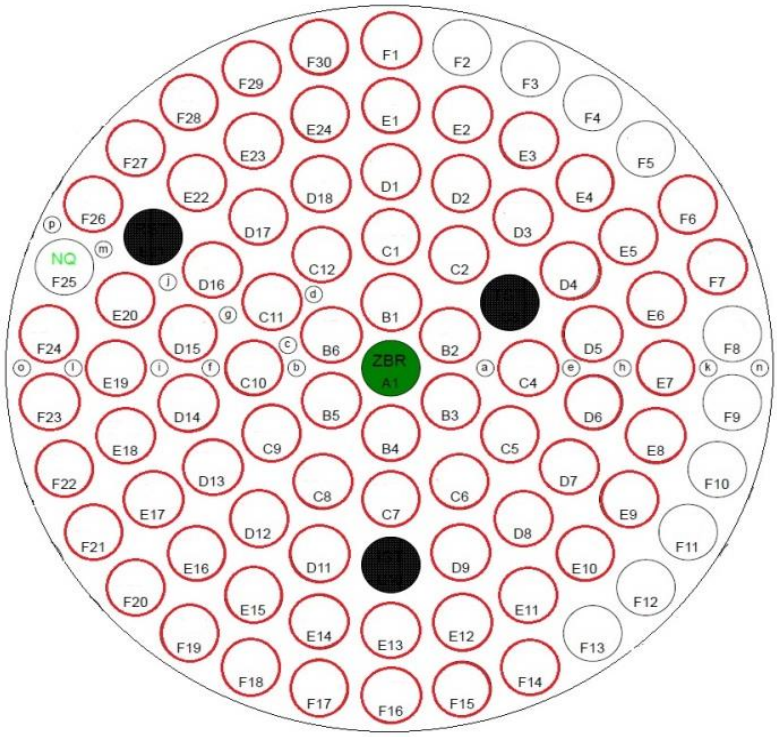

Figure 1. 14: Current core configuration at the TRIGA Mark II reactor of TU Wien.

regulating); in the fifth ring (F) there are, finally, 30 positions, including 19 of fuel, 8 elements of graphite (dummy), a neutronic source (NQ) and two pneumatic-transfer irradiation channels (positions F8 and F11). The central core position is the Central Thimble (CT), the reactor irradiation facility with the higher flux available.

The core is cooled by natural circulation of water and by a forced cooling system (primary circuit of the reactor). The water occupies about 1/3 of the volume of the core, filling the space between the occupied positions.

Fuel Elements

The fuel elements (FE(s)) made by General Atomic for the use in TRIGA reactors, can be of different types as for dimensions and fuel component ratios. At the TRIGA reactor of TU Wien, all the FE(s) are currently of the same type, that is stainless steel clad standard or 104-type FE.

They have a cylindrical geometry and consist of a central bar of fuel-moderator material of 38.1 cm height and 3.64 cm diameter (Figure 1.15). The overall dimensions of all types of FE(s) are same i.e. 3.75 cm in diameter and 72.06 cm in length. One disk of consumable poison (Moly) is place at one end of the fuel

meat length and a small cylinder of graphite (vertical reflector) is placed on both ends of the fuel meat; in addition, this type of fuel presents a central zirconium rod.

The fuel itself is a homogeneous solid mixture of zirconium hydride (HZr) and uranium (U), containing 8.5% by weight of low enriched uranium (U-235 enrichment is about 20%). The average weight of the fuel meat per FE is 2259.85 g containing 2067.02 g of HZr, 191.27 g of uranium: the amount of U-235 in a fuel element is then about 38.19 g. The fuel specification for a TRIGA fuel elements type 104 are shown in Table 1.3.

Each fuel element presents a stainless steel cladding with a thickness of 0.51 mm: the ends are shaped in a way that the lower one positions and supports the element in the lower core grid, and the upper one is useful for handling and moving of the fuel element.

The zirconium hydride (HZr) is responsible for the TRIGA fuel moderating capacities, strongly dependent on the temperature of this compound.

Fuel Type	**104 SS-clad**
Fuel meat	
Density (g/cm^3)	5.8624
Length (cm)	38.1
Diameter (cm)	3.6449
Burnable Poison	**1 Moly disk**
Density (g/cm^3)	10.28
Thickness (cm)	0.02
Diameter (cm)	3.63
Axial Reflectors	**Graphite**
Density (g/cm^3)	1.6
Upper refl. Length (cm)	6.8
Lower refl. Length (cm)	9.31
Diameter (cm)	3.63
Central Zr-rod	**Zr**
Density (g/cm^3)	6.49
Length (cm)	38.1
Diameter (cm)	0.635
Fuel Cladding	**SS-304**
Density (g/cm^3)	7.9
Thickness (cm)	0.051
Total Length	72.06
Total diameter	3.75

Table 1. 3: Fuel specification for the TRIGA fuel elements type 104.

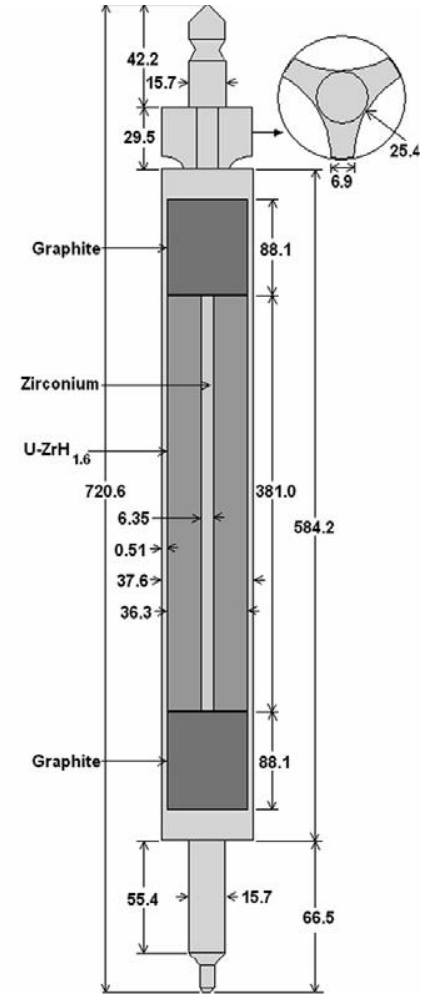

Figure 1. 15: TRIGA fuel element type 104 (all dimensions are in millimetres).

In fact, although in the molecule of HZr the hydrogen is placed at the center of a regular tetrahedron, for energies higher than the thermal ones (E> 0.5MeV) it can be supposed free, allowing the slowing of the neutron by means of the elastic diffusion on the hydrogen. Instead, for thermal energies it is necessary to take into account the molecular structure of HZr; thus, since the mass of the neutron is negligible compared to that of the crystal ($m_n<m_{HZr}$), the energy transferred by the neutron in an elastic collision is extremely small, and makes this process ineffective. To explain what happens to thermal neutrons when they interact with zirconium hydride, it is useful to refer to the Einstein model; since the crystal lattice of HZr has discrete levels with $\Delta E = h\nu = 0.13\,eV$ or multiples of this value, if a neutron has an energy $E_n > h\nu$ it can transfer to the lattice one or more quantum of energy ; if, conversely, $E_n < h\nu$, the neutron can not be further thermalized and can receive a quantum of energy from the lattice,

with probability proportional to $e^{-h\nu/kT}$. Therefore, thermal neutrons with E_n <0.13 eV, rather than being moderate, have a finite probability of being accelerated, which increases proportionally with the temperature.

It is clear that a temperature increase induces the reduction of the thermal population and, therefore, of the probability of fission, guaranteeing an automatic limitation of the reactor power (it is then possible to perform power pulses with peaks up to 250 MW and width at half height of 30 ms).

Control Rods

The reactor is controlled by three control rods: one fine adjustment rod (REGULATING), one safety rod (SHIM) and one pneumatic transient rod (TRANSIENT). The positions of all three control rods can be seen in Figure 1.14. The control rods are cylinder shaped with length of 51 cm, while the diameter of each rod is different as described in Table 1.4. They are made of boron carbide and can adapt to any of the 90 positions available in the core lattice. The choice of the material is justified by the high capture cross section ($3.8 \cdot 10^{-21}$ cm^2) of boron for thermal neutrons. The fast insertion (scram) of the control rods in the core causes a significant decrease in the neutron population, slowing down the chain reaction; instead, the extraction generates the multiplication of the neutron population and therefore the increase in power.

Control Rod	Dimension (cm)	Material	Density (g/cm^3)
SHIM		B_4C	2.48
Outer diameter	3.2		
Length	51		
Cladding Thickness	0.071	Al	2.7
REGULATING		B_4C	2.48
Outer diameter	2.2		
Length	51		
Cladding Thickness	0.071	Al	2.7
TRANSIENT		B_4C	2.48
Outer diameter	2.5		
Length	51		
Cladding Thickness	0.071	Al	2.7

Table 1. 4: Specification of the SHIM, REGULATING and TRANSIENT control rods at the TRIGA reactor of TU Wien.

For the insertion and extraction mechanism, two rods (REGULATING and SHIM) are connected to an electromagnet that is hooked and moved by means of an electric motor; removing the power supply to the electromagnet, the free fall of the bar in the core occurs, with consequent switching off of the reactor. The TRANSIENT rod, on the other hand, is extracted by means of a compressed air pneumatic system: with reactor critical at low power, through the rapid extraction of the TRANSIENT, power pulses can also be performed.

Neutron Source

The cylindrical photo-neutron Sb-Be neutron source element is placed in the reactor core to trigger the chain reaction and obtain the minimum fission yield that can be measured by the instrumentation. The source presents two different cylinders one inside the other (inner Sb cylinder and outer Be cylinder). The inner Sb cylinder has a diameter of 1 cm while outer Be cylinder has thickness of 0.5 cm. This source element has total length of 40.4 cm. The Sb emits gamma radiation; (γ, n) reactions with Be take place in the outer cylinder, producing the neutron needed for the reactor start-up. During the normal operation this source emits 6×10^6 neutrons per second.

Graphite Dummy Element

These elements are filled with nuclear grade graphite and occupy those grid positions which are not filled by FE(s). Their dimensions are same as a FE. The current reactor core has 8 graphite elements in F-ring as shown in Figure 1.14.

1.5.3. Graphite Reflector

The core of the TRIGA reactor is entirely surrounded by a radial graphite reflector, which has the task of reflecting part of the neutrons towards the core, to increase and homogenize the flux inside it. The reflector consists of a ring-shaped graphite block having a radial thickness of 30.5 cm, with an internal diameter of 45.7 cm and a height of 55.9 cm. As a result, the reflector and core assembly form a cylinder of about 1.09 m in diameter and high 0.58 m.

Immersed in the water tank of about 1.98 m in diameter and 6.2 m deep, the reflector rests on a platform placed about 61 cm from the bottom of the tank.

To prevent the water from entering the tank into graphite, the entire reflector is enclosed in a sealed aluminum container; in the upper part of the reflector there is an "annular seat" for the rotatory specimen rack (Lazy Susan), also covered in aluminum. The rotatory specimen rack is self-contained unit and does not penetrate the sealed reflector assembly at any point.

The reflector block rests on the reflector platform and provides support for two grids, one upper and one lower. The upper grid, an aluminum sheet of 49.5 cm in diameter and 1.9 cm thick, allows the accurate radial positioning of the core components (by means of 90 holes with a diameter of 3.82 cm applied at the elements, plus a central hole with a diameter of 3.84 cm to accommodate the Central Thimble). The lower grid, an aluminum sheet with a diameter of 40.7 cm and a thickness of 1.9 cm, supports the entire weight of the core and provides for the accurate spacing between the fuel elements; it is supported by six L-shaped lugs welded to the lower part of the reflector housing. Both the holes of the upper grille and those of the lower grating are shaped to receive the fixing pins of the fuel elements; moreover, most of the cooling water enters the core through the lower grid.

1.5.4. Grid plates

Two aluminium grid plates are placed at the top and bottom of the reactor core.

The top grid plate is 49.5 cm in diameter and 1.9 cm in thickness. In this grid, 90 holes with diameter 3.82 cm are drilled in five concentric rings to locate the core components (FE(s), control rods, source element, dummy elements, etc.); an additional 91st central hole (with diameter 3.81 cm) accommodates the Central Thimble (CT). About sixteen smaller holes (diameter 8 mm) are present at various positions along radial directions of the core: those holes allow irradiation of small samples (e.g. foils for flux determination) in the core.

The bottom grid plate (40.7 cm in diameter and 1.9 cm in thickness) supports the entire weight of the core and provides the exact spacing between core components. The central hole of 39.9 mm diameter serves as a clearance hole for

the central thimble while the other ninety holes with 7.14 mm diameter provide alignment with the holes in the top plate.

1.5.5. Reactor tank

The reactor core and the graphite reflector are placed on the bottom of an aluminum container filled with water, the tank, 2 meters in diameter and 6.25 meters deep (Figures 1.12 and 1.13). The core is placed at 61 cm from the bottom of the tank, then about 4.9 m of water above it act as vertical screen, while 45.7 cm of water represent the radial shield together with the graphite of the reflector.

The tank is crossed by the four irradiation channels, the thermal column and the thermal column of the pool.

1.5.6. Experimental Facilities

This type of research reactor was particularly designed to allow the various fields of basic and applied nuclear research and education. The TRIGA Mark II of Vienna is equipped with many irradiation facilities inside and outside the reactor core. It incorporates facilities for neutron and gamma irradiation studies as well as for isotope production, sample activation and students training. The reactor and its experimental facilities are surrounded by a reinforced barite concrete (nominal density 3.35 g/cm^3) structure standing 6.55 meters above the reactor room floor.

In-core irradiation facilities

Inside the reactor core, there are several irradiation experimental facilities. One is a Central Thimble (CT) which is used to irradiate the relatively larger samples in the core at the maximum flux density. Ring F hosts two irradiation facilities (POS 8 and POS 11): in both cases, a high speed pneumatic transfer system permits to produce very short lived isotopes and to transfer them in to the laboratory for analysis. Additional irradiation positions in the core are defined by 16 holes in the top grid plate (Figure 1.14).

Out of core irradiation facilities

Among the out of core irradiation facilities, there are the thermal column, the annular groove irradiation facility (Lazy Susan) and the horizontal beam tubes (Figures 1.12 and 1.13).

The thermal column of the TRIGA reactor is used to supply thermal neutrons for special irradiation experiments. It is a large (1.2×1.2×1.6 meters outside dimensions), boral lined, graphite-filled aluminium irradiation facility.

The annular groove irradiation facility (Lazy Susan) in the upper part of the reflector body is the cavity that remains at the TRIGA reactor of TU Wien after the removal of the original rotary specimen rack. The cavity in the reflector is filed with the tank water and 5 vertical Aluminium irradiation tubes (namely LS1, LS2 ,…. LS5) are located at different positions. The dry irradiation tubes are accessible from the reactor top and allow the irradiation of small samples in the Lasy Susan facility.

The four horizontal beam tubes (i.e. A, B, C and D) penetrate the concrete shield and the aluminium tank and pass through the reactor tank water to the reflector. These irradiation facilities provide different shaped neutron spectra and gamma radiation for a variety of experiments. Additionally they allow to irradiate large samples (up to 15 cm) in a region close to the core. Three beam tubes (i.e. A, B and C) are oriented radially with respect to the center of the core, one (D) is tangential to the outer edge of the core. Among the radial tubes, two (B and C) stop at the outer edge of the reflector but are aligned with the cylindrical void in the reflector graphite. The third radial tube (i.e. A), penetrates into the graphite reflector and terminates at the inner surface of the reflector, just at the outer edge of the core. The fourth beam tube (i.e. tangential beam tube) terminates at the outer surface of the reflector, but is also aligned with the cylindrical void, which intersects the piercing tube in the graphite reflector. In order to avoid intersection with the Lazy Susan, their horizontal beam tubes axis are located 7 cm below the equatorial plane (z=0) of the core. Each horizontal beam tube consists of two parts: the inner one, towards the core, is delimited by an

aluminum tube of 15.2 cm in diameter; while the external part is defined by a 20.3 cm diameter steel tube.

1.5.7. The biological shield

The TRIGA MARK II reactor shield consists of a reinforced concrete structure that rises 6.55 meters from the floor of the reactor room. This structure completely surrounds the core and the plants for experiments.

Chapter 2

Neutron flux and spectrum measurements

The first objective of the present research project was to develop a methodology, based on Monte Carlo codes calculations validated by direct measurements, for the evaluation of neutron fluxes distribution in known operating research reactors (such as the TRIGA Mark II reactor of the TU Wien). The present chapter describes the experimental procedure and presents the results for the measurement of the neutron fluxes and their energy distribution.

By means of an extensive measurements campaign, different positions were characterized both in- and out-core. The in-core positions were defined along both vertical and radial core axes; the out-core positions extended from the Lazy Susan facility till one of the horizontal beam tubes. The measurements were performed adopting a method based on activation of different material foils followed by a flux de-convolution analysis using the iterative code SAND II.

Neutron fluxes and energy distribution measurement results are here reported and have been subsequently used for the validation of the Monte Carlo calculation models (see Chapter 3 and Chapter 5).

2.1 Measurement methodology

The methodology adopted for the experimental determination of the neutron flux and neutron energy distribution included the activation of different material foils in the reactor and the de-convolution analysis of the experimental activity values by means of the code SAND II. In this paragraph, a summary of the neutron activation technique and a

description of the SAND II code are provided, as well as the information about the selected reactions and materials used in the experiment.

2.1.1 Foils neutron activation technique

Since the typical neutron detectors are not always usable to determine the intensity and the spectrum in the energy of a neutron generic field (because they require directed beams or predominantly thermal or fast beams), a useful alternative to these detectors consists in the method of analysis for activation[7,8], which involves the irradiation and the activation of a sample by means of a neutron field and the subsequent counting of the radioactivity induced in it.

Through the activation technique, from the measurement of radioactive isotopes activities (generated by reactions (n,γ), (n, p), (n,α), (n, n') which have cross sections predominant in specific energy ranges) it is possible to determine the neutron flux. Condition for a satisfying result is the knowledge of involved cross sections; a good counting efficiency of the produced radioactive isotopes activities; as well as taking into account all the effects that may change the result of the measurement. The radioactive isotopes produced by the reactions are chosen in order to cover the energy spectrum of interest.

In general, if a material foil contains m_0 target nuclei at the time t=0, the variation of those nuclei in the time interval dt is:

$$\frac{dm}{dt} = -m_0\,\overline{\sigma}_m(t)\Phi(t) \tag{2.19}$$

where $\overline{\sigma}_m(t)$ is the average cross section on all energy spectrum and for every reaction responsible for removing any of the m_0 nuclei. The solution of equation 2.19 is:

$$m = m_0\, e^{-\int_0^t \overline{\sigma}_m(t')\Phi(t')\,dt'} \tag{2.2}$$

If n_0 is the number of radioactive nuclei at time t=0 and n(t) the number of nuclei at the time t, the average number of nuclei that undergo radioactive dacay in the interval of time dt is given as:

$$dn(t) = -\lambda\, n(t)\, dt \tag{2.3}$$

From which the radioactive decay low is obtained:

$$n(t) = n_0\, e^{-\lambda t} \tag{2.4}$$

where λ is the decay constant. Other parameters of a specific decay are the mean lifetime ($\tau = 1/\lambda$) and the half-life ($T_{1/2} = \ln 2/\lambda$), respectively the time required to reduce to n_0/e ant to $n_0/2$ the initial value n_0.

On the other side, the activity is defined as the average number of nuclei that dacay per second and it is obtained by the (2.3):

$$A = -\frac{dn(t)}{dt} = \lambda\, n(t) = n_0\, \lambda\, e^{-\lambda t} \tag{2.5}$$

Now we consider a sample with *m* target nuclei, exposed to an integral neutron flux $\Phi(t)$; if $\overline{\sigma}_{mn}$ is the average total cross section for the reaction producing "*n*" radioactive nuclei, then $m\overline{\sigma}_{mn}(t)\Phi(t)$ is the number of activated nuclei per second. Then the radioactive population will vary in the unit of time according to:

$$\frac{dn}{dt} = m\overline{\sigma}_{mn}(t)\Phi(t) - n\overline{\sigma}_{n}(t)\Phi(t) - n\lambda_n \tag{2.6}$$

where $(m\overline{\sigma}_{mn}(t)\Phi(t))$ is the number of produced radioactive nuclei from the "m" target nuclei, $-n\lambda_n$ is the number of radioactive nuclei that disappear due to the decay and $\overline{\sigma}_n(t)$ is the total average cross section for all those reactions that remove some of the "*n*" radioactive nuclei. Combining (2.6) and (2.2) we obtain:

$$\frac{dn}{dt} = m_0\, \overline{\sigma}_{mn}(t)\Phi(t)\, e^{-\int_0^t \overline{\sigma}_m(t')\Phi(t')dt'} - n\left[\lambda_n + \overline{\sigma}_n(t)\Phi(t)\right] \tag{2.7}$$

The solution of the linear differential equation (2.7) is:

$$n = m_0\, e^{\left[-\lambda_n t - \int_0^t \overline{\sigma}_n(t')\Phi(t')dt'\right]} \int_0^t \overline{\sigma}_{mn}(t')\Phi(t')\, e^{\left\{\lambda_n t' + \int_0^{t''}[\overline{\sigma}_n(t'') - \overline{\sigma}_m(t'')\Phi(t'')]dt''\right\}} dt' \tag{2.8}$$

In the hypotesis that the variation of target and produced nuclei number is negligible with exception of what concern the activation and radioactive decay

process ($\overline{\sigma}_n(t)\Phi(t)$, $\overline{\sigma}_m(t)\Phi(t) << \lambda_n$), the equation (2.8) can be written as:

$$n = m_0\, e^{-\lambda_n t} \int_0^t \overline{\sigma}_{mn}(t')\,\Phi(t')\, e^{\lambda_n t'} dt' \tag{2.9}$$

Hence, equation (2.9) provides the average number n(t) of radioactive nuclei at the time t. In case of constant flux ($\Phi(t) = \Phi$), the cross section is also independent from time ($\overline{\sigma}_{mn}(t) = \overline{\sigma}_{mn}$) and equation (2.9) becomes:

$$n = \frac{m_0\, \overline{\sigma}_{mn}}{\lambda_n} \Phi\,(1 - e^{-\lambda_n t}) \tag{2.10}$$

The *activity* of an irradiated sample results to be:

$$A(t) = \lambda_n\, n = -\frac{dn}{dt} = m_0\ \overline{\sigma}_{mn}\, \Phi\,(1 - e^{-\lambda_n t}) \tag{2.11}$$

And the *saturation activity*, that is the activity for long irradiation time such that the number of radioactive nuclei formed correspond to the number of decayed nuclei, is:

$$A_S = \lim_{t\to\infty} A(t) = m_0\, \overline{\sigma}_{mn}\, \Phi \tag{2.12}$$

The activation analysis technique is based of the equation (2.11): in fact, known the sample composition (m_0) and the decay mode ($\lambda_n, \overline{\sigma}_{mn}$), trought the measurement of the activity *A(t)* is possible to determine the neutron flux Φ .

In addition, equation (2.11) has to be corrected in order to take into account on one side the decay of the sample during the cooling down period between end of irradiation and start of the measurement; on the other side, the decay during the measurement itself (if $T_{1/2}$ is comparable with the counting time). If ($t_2 - t_1$) is the time elapsed between the end of irradiation and the starting of the measurment, equation (2.11) becomes:

$$A(t_2) = m_0\ \overline{\sigma}_{mn}\, \Phi\,(1 - e^{-\lambda_n t})\, e^{-\lambda_n (t_2 - t_1)} \tag{2.13}$$

Instead, the number of countings obtained in the time interval ($t_3 - t_2$) is obtained by integration of the activity $A(t_2)$ according to (2.5):

$$N_C = \int_0^{t_3-t_2} k \cdot A(t_2)\, e^{-\lambda t} dt = \\ = k \frac{m_0\, \overline{\sigma}_{mn}}{\lambda} \Phi \left(1 - e^{-\lambda t}\right) e^{-\lambda (t_2 - t_1)} \left(1 - e^{-\lambda (t_3 - t_2)}\right) \tag{2.14}$$

where k is the efficiency of the detector. From equation () is finally possible to determine the neutro flux Φ:

$$\Phi = \frac{\lambda\, N_C}{k\, m_0\, \overline{\sigma}_{mn} \left(1 - e^{-\lambda t_1}\right)\left(e^{-\lambda (t_2 - t_1)} - e^{-\lambda (t_3 - t_2)}\right)} \tag{2.15}$$

The equation (2.15) allows to determine the neutron flux for a monoenergetic beam with energy E. In case of a continuos neutron spectrum, several different activation measurements are required in order to obtain $\Phi(E)$ with appropriate deconvolution techniques: in this work, the deconvolution program SAND II was used as described in the following paragraph.

2.1.2 Sand II Code

The SAND II (*Spectrum Analysis by Neutrons Detectors II*)[9] code is designed to provide a *best fit* neutron flux spectrum for a given input set of infinitely dilute foils activities. The input activities are extrapolated to saturation and the solution spectrum is a differential flux. The code uses a 620 discrete intervals description of the neutron energy range between 10^{-10} and 18 MeV (45 per decade up to 1 MeV, and 170 between 1 and 18 MeV). The solution spectrum is presented in tabular form at 621 energy points.

The problem is to evaluate 621 unknown variables (differential flux values, Φ_i) in a system of *n* linear activity equations, with $n << i$, where *n* is the number of foils used. The computational procedure consists of selection of an initial approximation spectral form (*guess flux*) and iteration from that approximation to a form acceptable as an appropriate solution of the system. The solution is, of course, not unique since the number of equations is much smaller than the number of unknown variables. Appropriateness of the solution therefore depends, up to a certain extent, on a suitable choice of the guess flux which should be based on all available physical information in any given case.

The criterion incorporated into the code for achievement of an acceptable solution is based on a comparison of successive iterative differential flux calculated values: a solution is considered to have been achieved when the difference between two successive values is smaller than a percentage specified in the input at all 621 energy points.

The following iteration algorithm is utilized by SAND II:

$$\varphi_j^{[k+1]} = \varphi_j^{[k]} \exp\left\{C_j^{[k]}\right\} \tag{2.16}$$

$$C_j^{[k]} = \frac{\sum_{i=1}^{n} W_{i,j}^{[k]} \ln R_i^{[k]}}{\sum_{i=1}^{n} W_{i,j}^{[k]}} \tag{2.17}$$

$$R_i^{[k]} = \frac{A_i}{A_i^{[k]}} \tag{2.18}$$

where:

- $\varphi_j^{[k]}$: integral flux in the jth energy interval, between E_j and E_{j+1}
- $C_j^{[k]}$: activity-weighted correction term (based on the logarithm of $R_i^{[k]}$, since the $R_i^{[k]}$ often differs by several order of magnitude at the start of iteration, depending on the initial approximation spectrum)
- $R_i^{[k]}$: ratio of measured to calculated activity
- A_i: measured activity for the ith foil reaction (extrapolated to saturation and infinite dilution)
- $A_i^{[j]}$: calculated activity for the ith foil reaction, based on the kth iterative spectrum
- k=1, 2, 3, ... (iteration index)
- j=1, 2, ...620 (energy interval index)
- i=1,2, ... n (foil index).

Steps of iterative procedure can be summarized as follows:

- for each foil/reaction, activities are calculated based on the current iterative spectrum and the evaluated reaction cross section library which is part of the code;

- the calculated activities are compared with the measured activities to provide a correction factor for each foil/reaction;
- a weighting function (of energy) is obtained, for each foil/reaction, based on the sensitivity function (differential cross section multiplied by differential flux) for that foil/reaction calculated at the current iteration;
- the foil/reaction weighting functions are applied to an averaging procedure to obtain an average correction factor at each energy, based on the comparison of measured to calculated activity for each foil and on the relative contribution of the flux at the given energy to the activity of that foil;
- the average correction factors are then applied to the current iterative flux value at each energy to obtain the next iterative flux spectrum.

SAND II includes the option of selecting an initial approximation spectral form among a library of reference forms. Since no physical information is incorporated into this selection method, it is emphasized that the reference spectrum library is meant to be available for use only as a last resort, in cases for which so little information is available that no meaningful selection of an initial approximation can be made on the basis of physical knowledge of the measured environment. It is worthy to notice that SAND II best approximated solution is strongly dependent from the guess flux form (i.e. energy distribution) but almost independent from its integral value. Since one of the critical points of this methodology is the definition of the guess neutron flux, the decision was taken to use as input guess flux the result of previous modelling and computation[10] performed by means of the MCNP Monte Carlo code for a similar reactor.

2.1.3 Material foils selection

In order to apply the deconvolution technique described above, several experimental activity values needed to be determined. Then, the first step for the experimental determination of the neutron flux and spectrum in several reactor irradiation positions was the identification of proper reactions, i.e. material foils, to be used for irradiation with subsequent activation.

Element	Target Isotope	Isotopic abundance (%)	Nuclear Reaction	Effective Threshold[11] (MeV)	σ_0 (barn)	$T_{1/2}$
Au	^{197}Au	100	^{197}Au (n,γ) ^{198}Au	--	98.8	2.7 d
Cu	^{63}Cu	69.17	^{63}Cu (n,γ) ^{64}Cu	--	4.5	12.7 h
Fe	^{54}Fe	5.8	^{54}Fe (n,p) ^{54}Mn		0.4	312.7 d
Ni	^{58}Ni	68.27	^{58}Ni (n,p) ^{58}Co	3.45	0.6	70.78 d
In	^{115}In	95.7	^{115}In (n,n') ^{115}In*	1.65	0.35	4.36 h
Al	^{27}Al	100	^{27}Al (n,p) ^{27}Mg	5.30	0.08	9.46 m

Table 2.1: Nuclear reactions used for activation and neutron flux determination.

To reduce the indeterminacy of the system of linear equations, some of the target foils have been chosen in such a way that their reaction cross sections present an energy threshold[11] (i.e. these elements can be activated only if the energy of the incident neutron is above the threshold).

The material foils and nuclear reactions used to perform the measurements are listed in Table 2.1. The flux characterization in each in-core and out core position was performed with the same set of material foils.

As for their geometry, the selected foils presented a round disc shape, same diameter (d=6 mm) and thickness between 0.025 mm and 1 mm in order to compensate for the isotopic abundance and the difficulty of activating certain reactions. The foils were standard certificated material foils: characteristics such as the pureness, the nuclide of interest, the isotopic abundance for that particular nuclide, the dimensions and the mass of a typical set of irradiated foils are shown in Table 2.2.

To investigate the neutron flux spectrum in the epithermal energy region (0.2 eV - 0.5 MeV) and separating this contribution from the thermal neutrons contribution, some foils (Au) were irradiated also under a Cadmium cover.

Element	Pureness (%)	Target Isotope	Diameter (mm)	Thickness (mm)	Mass (mg)
Au	99.99	^{197}Au	6	0.025	13.66
Cu	99.99	^{63}Cu	6	0.5	126.58
Fe	99.99	^{54}Fe	6	1.0	222.63
Ni	99.999	^{58}Ni	6	0.5	125.85
In	99.999	^{115}In	6	0.5	103.34
Al	99.99	^{27}Al	6	0.25	19.09

Table 2.2: Characteristic of a typical foils set used for the neutron flux determination.

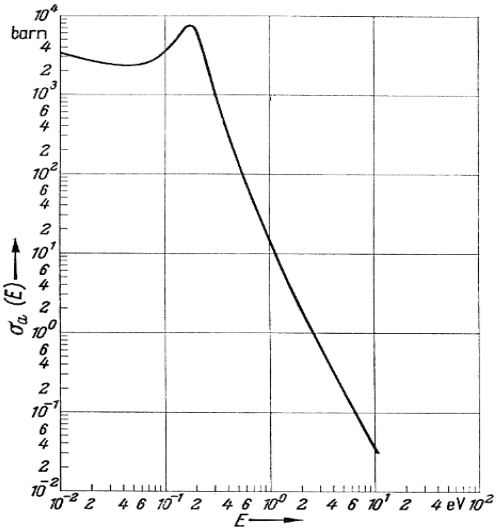

Figure 2.1: The absorption Cadmium cross section as a function of the energy of incident neutron[11].

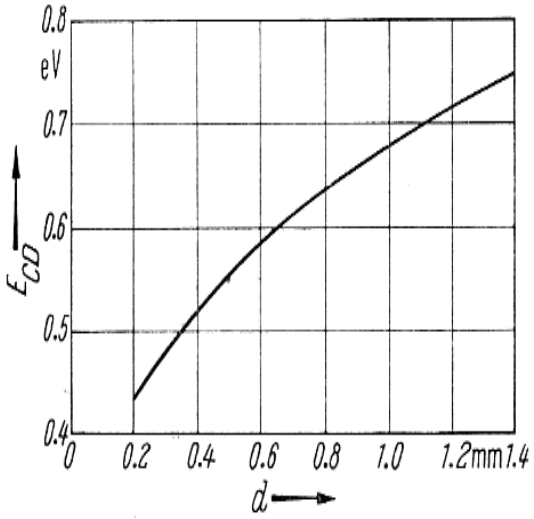

Figure 2.2: The Cadmium cut-off energy as a function of Cadmium cover thickness[11].

In fact, as it can be seen in Figure 2.1, Cadmium presents a hight absorption cross section in the thermal energy region. As a consequence, a foil in a cadmium cover is exposed to a neutron spectrum with energy above a certain energy value, named Cadmium cuf-off energy[11]. The value of E_{CD} varies with the thickness of the cadmium cover (Figure 2.2). The Cadmium covers used in the present irradiations had a thickness of about 0.5mm (corresponding to a cut-off energy of 0.55 eV).

Due to the otherwise high activation via (n,γ) reactions of other isotopes, indium foils were always covered with cadmium.

2.2 In-core flux determination along radial and vertical direction

The irradiation experimental facilities inside the reactor core for the in-core measurement campaign were the Central Thimble (CT) and a set of radial position defined by the holes in the core grid plates.

The Central Thimble (CT) was used for irradiation of foils along the vertical axis, while the positions defined by the holes in the core grid plates (see 1.5.4) were used for irradiating foils along the radial core direction.

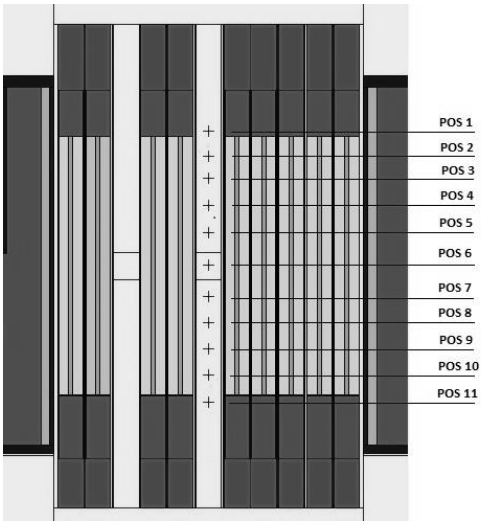

Figure 2.3 Errore. Nel documento non esiste testo dello stile specificato.**: Irradiation positions along the core vertical axis in the Central Thimble (CT): POS 6 correspond to core equatorial position.**

In the Central Thimble (CT), 11 positions were defined for irradiations along the reactor vertical axis. The locations of irradiation positions (POS1, POS2, …, POS11) are shown by the markers in Figure 2.3: the exact distances are taken from the core equatorial position along the vertical axis (z=0) and are reported in Table 2.3. A proper sample holder with 11 locations was designed and used for CT irradiations: every position in the sample holder hosted one foil per irradiation.

Along the radial direction, activity measurements were performed by irradiations in 3 (b, i, o) of the available positions defined by the holes in the top grid plate (Figure 2.4) at the equatorial level of the core (z=0). These selected positions (position b, i, o) are shown in Figure 2.4 and the radial distances from the center of the core (x=0) are listed in Table 2.3.

CT Irradiation position	**Vertical distance along Z axis (cm)**
POS 1	20
POS 2	16
POS 3	12
POS 4	8
POS 5	4
POS 6 (EQ)	0
POS 7	-4
POS 8	-8
POS 9	-12
POS 10	-16
POS 11	-20

RADIAL Irradiation position	**Radial distance along X axis (cm)**
POS 6 (EQ)	0
Position ***b***	-5
Position ***i***	-13.5
Position ***o***	-22

Table 2.3: Irradiation positions distances from core centre along Z (vertical positions) and X (radial positions) axis.

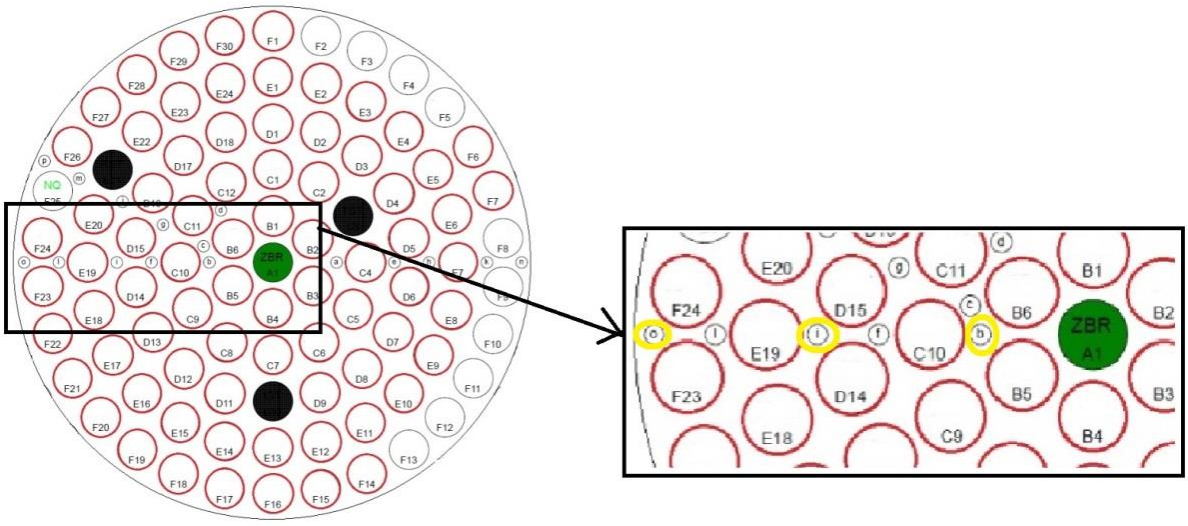

Figure 2.4. Current core configuration (left) and detail (right) of the three radial positions (b, i, o) used for flux characterization.

2.2.1 Target foils irradiation and measurements

In order to optimize irradiation and counting time, different irradiation shifts were needed to activate a set of foils (Table 2.2) in each of the defined positions: a total of eight irradiations, with fixed reactor power (1kW) and irradiation time from 10 to 30 minutes, were performed in the CT. Lastly, a copper (Cu) material foil was irradiated as flux monitor during every irradiation in a fixed position: its measured activity allowed to obtain the normalization factor for the specific irradiation. The general information about each irradiation in CT is reported in **Table 2.4**. The decision of irradiating same materials in different irradiations is due for optimization of the counting process by gamma spectrometry.

To cover the radial core positions, three irradiations (RAD1, RAD2, RAD3) were performed. Reactor power was set at 5 kW for 20 minutes irradiation time. As two foils could be allocated in the same irradiation position per time, in total one foil set was irradiated in each of the three positions (b, i, and o) according to the scheme in Table 2.4. The Aluminum foil was not irradiated due the need of long cooling down period (compared to the half-life of produced Mg-27).

Code of irradiation in CT	Irradiated foils	Reactor Power	Irradiation time (min)
CT1	Fe	1kW	30
CT2	Au (pos 1,2,3,9,10,11); Cu (pos 4,5,6,7,8)	1kW	10
CT3	Au (pos 4,5,6,7,8); Cu (pos 1,2,3,9,10,11)	1kW	10
CT4	Au(Cd) (pos 1,2,3,9,10,11); In(Cd) (pos 4,5,6,7,8)	1kW	30
CT5	Ni	1kW	30
CT6	Au(Cd) (pos 4,5,6,7,8); In(Cd) (pos 1,2,3,9,10,11)	1kW	30
CT7	Al (Pos. 1-5)	1kW	10
CT8	Al (Pos. 6-11)	1kW	10
Code of irradiation in the radial positions	Irradiated foils	Reactor Power	Irradiation time (min)
RAD1	Cu + In (positions b, i, o)	5 kW	20
RAD2	Au + Au+ Cd (positions b, i, o)	5 kW	20
RAD3	Ni + Fe (positions b, i, o)	5 kW	20

Table 2.4: Irradiations conducted in the Central Thimble (CT) positions and in the radial positions. For each irradiation, the irradiated foils and associated irradiation positions are reported.

Target foils activities were measured by means of a coaxial closed-ended HPGe n-type GAMMA-X (series C5020, CANBERRA) with 52.8% relative efficiency, 1.81 keV energy resolution at 1.33 MeV and Peak/Compton edge ratio equal to 73.6. The efficiency calibration of the detector was performed by means of a certified solid multi gamma calibration source (Type QCRB1186, Eckert&Ziegler) with dimension and geometry similar to those of the activated foils. An example of the obtained gamma spectrum for one of the gold foils is shown in Figure 2.5.

Characteristic of the foils and values of the detected specific activities extrapolated to saturation ($A_{spec-sat}$)[12] for each foil in the CT position and in radial positions are listed in the Table 2.5 and Table 2.6 (uncertainty of the measurements are discussed in detail in 2.4). The activity values $A_{spec-sat}$ are referred to end of irradiation (EOI) time, taking also into account decay during irradiation as described in 2.1.1. The reported values are also normalized through activity evaluation of Cu flux monitor foils, then the $A_{spec-sat}$ values in the different position can be directly compared.

The copper foil (flux monitor) activities were scaled for irradiation time and compared among the different irradiations. One irradiation (CT6) was set as reference irradiation (i.e. correction factor equivalent to 1) and correction factors (Table 2.7) were obtained and applied for all others irradiations in CT.

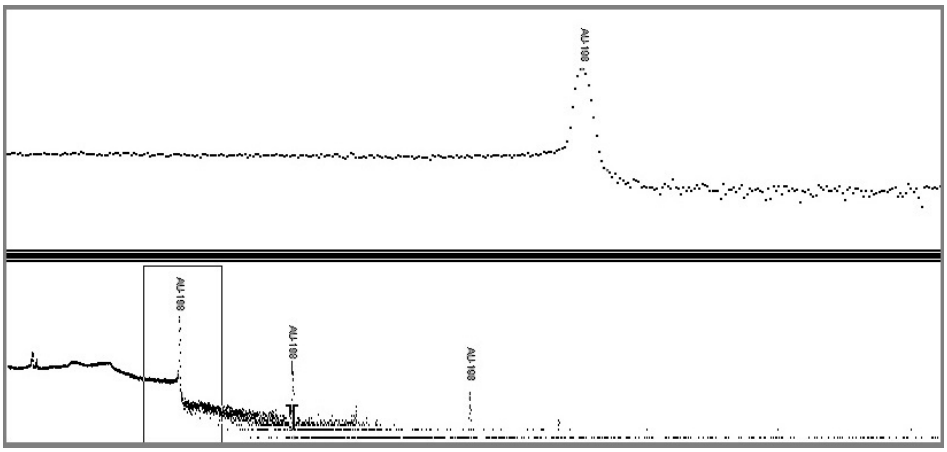

Figure 2.5: Typical gamma spectrum of an activated gold foil.

As an example, Figure 2.6 shows the plot along the vertical axis of detected activity values for gold foils; in the same way, Figure 2.7 shows results for Indium activity values. As expected, the activity value reaches its maximum in the central position (POS6) and decreases moving to the top or bottom of the vertical core extension with a typical cosine shape function.

2.2.2 Activity correction for foils self-absorption

SAND II code requires that all foil activities have to be adjusted to an infinite dilution of target nuclei, i.e. the code does not calculate the effects of self-shielding. Thus, all input (measured) activities must be corrected for self-absorption effect. However, when considering the reaction cross section values and the isotopic abundance of elements in the used target foils, the only self-absorbing correction needed for these measurements is for gold foils.

The self-absorption correction factors (C_{shield}) for gold foils were evaluated by means of a dedicated Monte Carlo computation. Using the MCNP6[13] Monte Carlo code, specific simulations of gold foils irradiation (plane and into a cadmium capsule) were performed using the In-ward Cosine card and with different foil density (varying from real density up to 10^6 diluted density). Thus, the C_{shield} for each gold foil was evaluated as the ratio between the reaction rates computed for real and for extremely diluted density[5].

Foil ID	Foil mass (mg)	Irradiation Position	$A_{spec-sat}$ (Bq/atoms)
Au1	13.77	POS1	$(3.28 \pm 0.16) \times 10^{-12}$
Au2	12.90	POS2	$(4.59 \pm 0.23) \times 10^{-12}$
Au3	13.26	POS3	$(5.91 \pm 0.30) \times 10^{-12}$
Au4	13.17	POS4	$(6.61 \pm 0.33) \times 10^{-12}$
Au5	12.26	POS5	$(7.19 \pm 0.36) \times 10^{-12}$
Au6	12.94	POS6	$(7.42 \pm 0.37) \times 10^{-12}$
Au7	12.62	POS7	$(7.19 \pm 0.36) \times 10^{-12}$
Au8	13.29	POS8	$(6.44 \pm 0.32) \times 10^{-12}$
Au9	13.68	POS9	$(5.43 \pm 0.27) \times 10^{-12}$
Au10	12.31	POS10	$(3.82 \pm 0.19) \times 10^{-12}$
Au11	13.29	POS11	$(2.64 \pm 0.13) \times 10^{-12}$
Cu1	122.88	POS1	(7.49 ± 0.37) E-14
Cu2	122.61	POS2	$(1.06 \pm 0.05) \times 10^{-13}$
Cu3	122.57	POS3	$(1.34 \pm 0.07) \times 10^{-13}$
Cu4	123.10	POS4	$(1.53 \pm 0.08) \times 10^{-13}$
Cu5	122.64	POS5	$(1.66 \pm 0.08) \times 10^{-13}$
Cu6	123.07	POS6	$(1.68 \pm 0.08) \times 10^{-13}$
Cu7	122.65	POS7	$(1.65 \pm 0.08) \times 10^{-13}$
Cu8	122.78	POS8	$(1.52 \pm 0.08) \times 10^{-13}$
Cu9	122.67	POS9	$(1.24 \pm 0.06) \times 10^{-13}$
Cu10	122.69	POS10	$(8.85 \pm 0.44) \times 10^{-14}$
Cu11	123.23	POS11	$(6.4 \pm 0.32) \times 10^{-14}$
AuCd1	12.24	POS1	$(1.90 \pm 0.09) \times 10^{-12}$
AuCd2	13.74	POS2	$(2.67 \pm 0.13) \times 10^{-12}$
AuCd3	13.10	POS3	$(3.26 \pm 0.16) \times 10^{-12}$
AuCd4	13.60	POS4	$(2.94 \pm 0.15) \times 10^{-12}$
AuCd5	12.59	POS5	$(3.10 \pm 0.16) \times 10^{-12}$
AuCd6	13.63	POS6	$(3.30 \pm 0.17) \times 10^{-12}$
AuCd7	13.83	POS7	$(3.25 \pm 0.16) \times 10^{-12}$
AuCd8	13.83	POS8	$(2.93 \pm 0.15) \times 10^{-12}$
AuCd9	13.62	POS9	$(2.85 \pm 0.14) \times 10^{-12}$
AuCd10	13.53	POS10	$(1.95 \pm 0.09) \times 10^{-12}$
AuCd11	13.07	POS11	$(1.24 \pm 0.06) \times 10^{-12}$
In1	99.32	POS1	$(1.71 \pm 0.08) \times 10^{-15}$
In2	99.55	POS2	$(2.76 \pm 0.14) \times 10^{-15}$
In3	100.50	POS3	$(3.54 \pm 0.18) \times 10^{-15}$
In4	99.21	POS4	$(4.16 \pm 0.21) \times 10^{-15}$
In5	100.31	POS5	$(4.5 \pm 0.22) \times 10^{-15}$
In6	98.86	POS6	$(4.67 \pm 0.23) \times 10^{-15}$

Foil ID	Foil Weight (mg)	Irradiation Position	$A_{spec-sat}$ (Bq/atoms)
In7	99.40	POS7	$(4.42 \pm 0.22) \times 10^{-15}$
In8	98.89	POS8	$(3.92 \pm 0.20) \times 10^{-15}$
In9	99.37	POS9	$(3.13 \pm 0.16) \times 10^{-15}$
In10	100.14	POS10	$(1.99 \pm 0.10) \times 10^{-15}$
In11	100.08	POS11	$(9.54 \pm 0.48) \times 10^{-16}$
Fe1	223.46	POS1	$(6.25 \pm 0.31) \times 10^{-16}$
Fe2	223.60	POS2	$(9.57 \pm 0.48) \times 10^{-16}$
Fe3	224.71	POS3	$(1.23 \pm 0.61) \times 10^{-15}$
Fe4	222.69	POS4	$(1.40 \pm 0.07) \times 10^{-15}$
Fe5	224.45	POS5	$(1.61 \pm 0.08) \times 10^{-15}$
Fe6	224.72	POS6	$(1.59 \pm 0.08) \times 10^{-15}$
Fe7	224.10	POS7	$(1.51 \pm 0.07) \times 10^{-15}$
Fe8	224.98	POS8	$(1.33 \pm 0.07) \times 10^{-15}$
Fe9	225.43	POS9	$(1.06 \pm 0.05) \times 10^{-15}$
Fe10	224.05	POS10	$(6.48 \pm 0.32) \times 10^{-16}$
Fe11	224.11	POS11	$(3.1 \pm 0.15) \times 10^{-16}$
Ni1	124.46	POS1	$(8.87 \pm 0.44) \times 10^{-16}$
Ni2	125.51	POS2	$(1.34 \pm 0.07) \times 10^{-15}$
Ni3	126.32	POS3	$(1.71 \pm 0.08) \times 10^{-15}$
Ni4	123.79	POS4	$(1.97 \pm 0.10) \times 10^{-15}$
Ni5	115.16	POS5	$(2.18 \pm 0.11) \times 10^{-15}$
Ni6	122.70	POS6	$(2.21 \pm 0.11) \times 10^{-15}$
Ni7	122.56	POS7	$(2.11 \pm 0.11) \times 10^{-15}$
Ni8	123.71	POS8	$(1.86 \pm 0.09) \times 10^{-15}$
Ni9	125.54	POS9	$(1.46 \pm 0.07) \times 10^{-15}$
Ni10	125.76	POS10	$(8.93 \pm 0.45) \times 10^{-16}$
Ni11	123.86	POS11	$(4.21 \pm 0.21) \times 10^{-16}$
Al1	17.40	POS1	$(2.99 \pm 0.15) \times 10^{-17}$
Al2	17.34	POS2	$(4.5 \pm 0.22) \times 10^{-17}$
Al3	17.29	POS3	$(6.16 \pm 0.31) \times 10^{-17}$
Al4	17.36	POS4	$(7.07 \pm 0.35) \times 10^{-17}$
Al5	17.40	POS5	$(8.28 \pm 0.41) \times 10^{-17}$
Al6	17.32	POS6	$(8.48 \pm 0.42) \times 10^{-17}$
Al7	17.42	POS7	$(8.06 \pm 0.40) \times 10^{-17}$
Al8	17.30	POS8	$(7.17 \pm 0.36) \times 10^{-17}$
Al9	17.47	POS9	$(5.87 \pm 0.29) \times 10^{-17}$
Al10	17.40	POS10	$(3.64 \pm 0.18) \times 10^{-17}$
Al11	17.42	POS11	$(1.64 \pm 0.08) \times 10^{-17}$

Table 2.5: Measured specific activities at saturation ($A_{spec-sat}$) for the foils irradiated in CT positions (POS1, POS2, …. , POS11).

Foil ID	Foil Weight (mg)	Irradiation Position	$A_{spec-sat}$ (Bq/atoms)
1Au	13.34	b	$(2.95 \pm 0.15) \times 10^{-11}$
2Au	12.86	i	$(2.06 \pm 0.10) \times 10^{-11}$
3Au	13.70	o	$(1.06 \pm 0.05) \times 10^{-11}$
1Cu	122.69	b	$(5.25 \pm 0.26) \times 10^{-13}$
2Cu	122.87	i	$(3.62 \pm 0.18) \times 10^{-13}$
3Cu	122.78	o	$(1.92 \pm 0.09) \times 10^{-13}$
1AuCd	12.37	b	$(1.66 \pm 0.08) \times 10^{-11}$
2AuCd	13.91	i	$(1.24 \pm 0.06) \times 10^{-11}$
3AuCd	13.63	o	$(6.33 \pm 0.32) \times 10^{-12}$

Foil ID	Foil Weight (mg)	Irradiation Position	$A_{spec-sat}$ (Bq/atoms)
1In	105.57	b	$(2.38 \pm 0.12) \times 10^{-14}$
2In	99.55	i	$(1.84 \pm 0.09) \times 10^{-14}$
3In	98.7	o	$(8.52 \pm 0.43) \times 10^{-15}$
1Fe	223.05	b	$(7.93 \pm 0.40) \times 10^{-15}$
2Fe	224.07	i	$(6.05 \pm 0.30) \times 10^{-15}$
3Fe	223.35	o	$(2.57 \pm 0.13) \times 10^{-15}$
1Ni	124.97	b	$(1.12 \pm 0.06) \times 10^{-14}$
2Ni	118.91	i	$(8.39 \pm 0.42) \times 10^{-15}$
3Ni	125.61	o	$(3.66 \pm 0.18) \times 10^{-15}$

Table 2.6: Measured specific activities at saturation ($A_{spec-sat}$) for the foils irradiated in the radial core positions b,i, and o.

The correction factors obtained with this simulation were as follows:

$$C_{shield} = 0.71$$

for plane foils, in the 5 CT central positions (Pos4, Pos5, Pos6, Pos7, Pos8);

$$C_{shield} = 0.64$$

for plane foils, in the remaining CT positions and in the radial core positions;

$$C_{shield} = 0.37$$

for cadmium covered foils.

Hence, for gold foils, the measured specific activity values were corrected dividing by the foils self-absorption factor (C_{shield}): $A_{spec\text{-}sat}$ values listed in Table 2.5and Table 2.6 are already corrected for self-absorption.

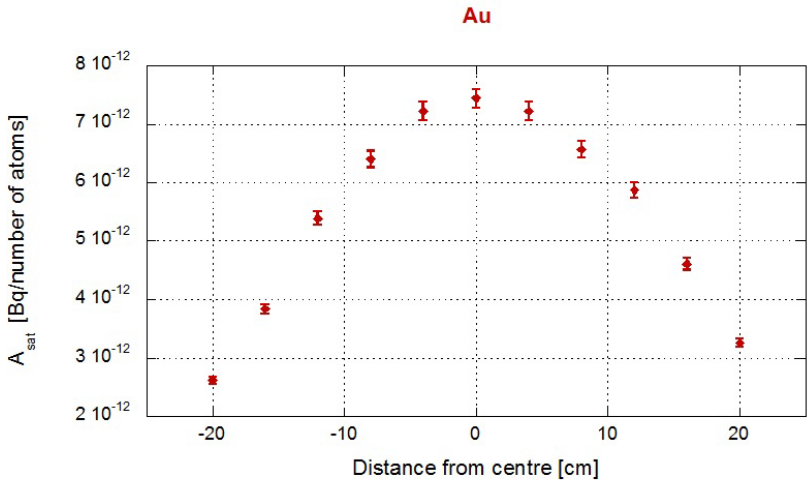

Figure 2. 6: Plot along the vertical core axis of Gold (^{197}Au (n,γ)^{198}Au) saturated activity values.

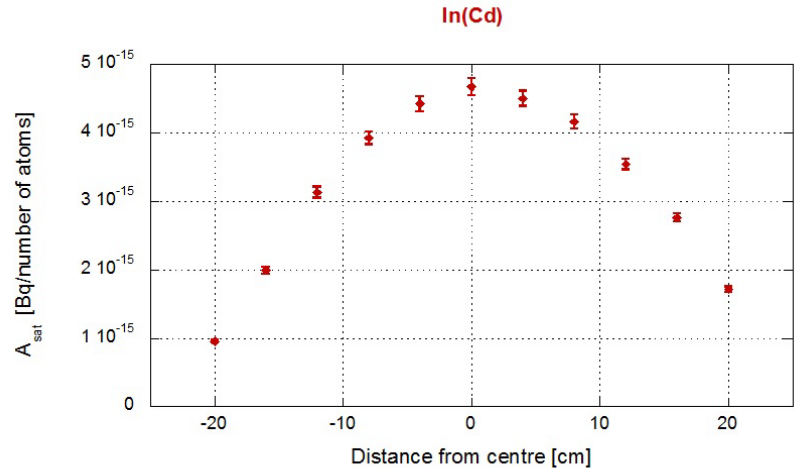

Figure 2. 7: Plot along the vertical core axis of Indium (^{115}In (n,n')^{115}In*) saturated activity values.

Irradiation Id.	$A_{spec-sat}$(Cu) (Bq/atoms)	Correction factor
CT1	$(1.23 \pm 0.04) \times 10^{-13}$	0.699
CT2	$(1.12 \pm 0.03) \times 10^{-13}$	0.636
CT3	$(1.73 \pm 0.05) \times 10^{-13}$	0.983
CT4	$(1.63 \pm 0.05) \times 10^{-13}$	0.926
CT5	$(1.88 \pm 0.05) \times 10^{-13}$	1.068
CT6	$(1.76 \pm 0.05) \times 10^{-13}$	1.000
CT7	$(2.12 \pm 0.06) \times 10^{-13}$	1.205
CT8	$(2.06 \pm 0.06) \times 10^{-13}$	1.170

Table 2.7: Copper (Cu) flux monitor foils saturation activity values ($A_{spec-sat}$) and correction factors used to normalize experimental results.

2.2.3 In-core neutron flux experimental results

For each measured activity (see Table 2.5 and Table 2.6) a set of 100 values fitting a Student's t-distribution with mean equal to the activity itself and standard deviation equal to the measure uncertainty was calculated. Thus, the SAND II program was run one hundred times for each irradiation position (i.e. 11 positions in CT, 3 positions in the radial direction) using, for each run, an input data set of specific activities at saturation previously calculated according to the Student's t-distribution. The program was set in order to accept the result when the difference between the calculated and the measured activities was less than the uncertainty of the gamma spectrometry measurements (see 2.4).

As a result, for each irradiation position, a set of one hundred solutions, i.e. neutron flux differential densities, was evaluated: each one distributed in 621 energy groups. Then, the average value of the flux differential density and the variance value were evaluated in each energy group in order to obtain, for each irradiation position, an average flux differential density with a standard deviation. This approach was chosen in order to be able to propagate directly, into the de-convolution process, the uncertainties of the measurements of the activated foils.

In Figure 2.8, the results in terms of neutron flux differential densities is shown for three of the characterised positions.

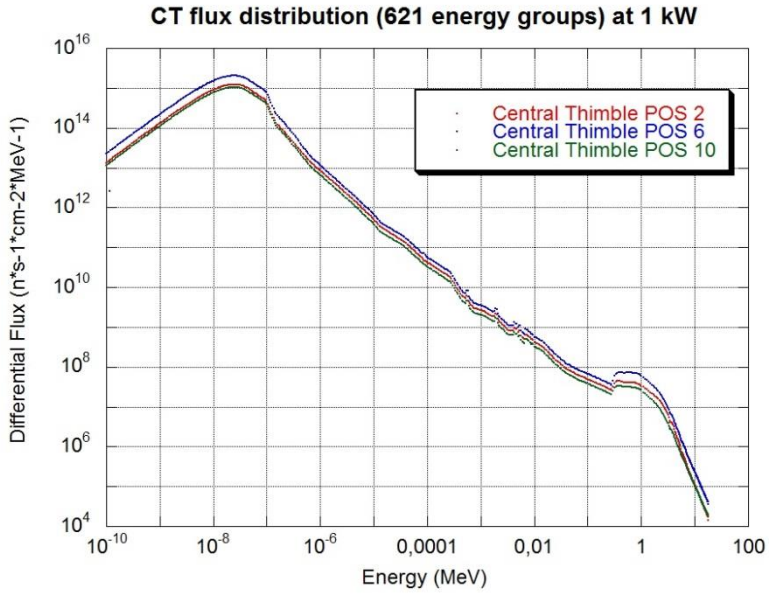

Figure 2. 8: Neutron flux differential spectrum in Central Thimble (CT) POS 2, POS 6, POS 10 at 1 kW reactor power.

The 621 energy groups were then collapsed to obtain the integral neutron flux densities for Thermal-, Epithermal- and Fast neutron regions.

The integral flux densities are reported in Table 2.8 for each characterized position (uncertainties reported in the tables are discussed in detail in 2.4) at 1kW reactor power.

Figures 2.9 shows the plot of the obtained flux values in the 11 CT positions: both Thermal- and Total-Flux values present the typical cosine profile along the reactor vertical axis.

Similarly, Figure 2.10 represents the Thermal- and Total-Flux values along the radial core direction: in this case four positions are utilized for the plot, 1 corresponding to the equatorial core position (POS6, x = 0) and 3 being the radial core positions *b, i, o* (x = 5cm; x = 13.5 cm; x = 22cm respectively).

Position	Thermal Flux (<0.69eV) [n •s^{-1} • cm^{-2}]	Epithermal Flux (0.69eV-110keV) [n •s^{-1} • cm^{-2}]	Fast Flux (110KeV-18MeV) [n •s^{-1} • cm^{-2}]	Total Flux [n •s^{-1} • cm^{-2}]
Vertical core direction				
Position 1	(1.75± 0.14) •10^{10}	(9.28± 0.74) •10^{9}	(1.04± 0.09) •10^{10}	(3.72± 0.30) •10^{10}
Position 2	(2.50± 0.20) •10^{10}	(1.23± 0.10) •10^{10}	(1.73± 0.16) •10^{10}	(5.46± 0.44) •10^{10}
Position 3	(3.18± 0.25) •10^{10}	(1.53± 0.12) •10^{10}	(2.19± 0.20) •10^{10}	(6.90± 0.55) •10^{10}
Position 4	(3.76± 0.30) •10^{10}	(1.48± 0.12) •10^{10}	(2.56± 0.23) •10^{10}	(7.80± 0.62) •10^{10}
Position 5	(4.11± 0.33) •10^{10}	(1.59± 0.13) •10^{10}	(2.72± 0.24) •10^{10}	(8.42± 0.67) •10^{10}
Position 6	(4.06± 0.32) •10^{10}	(1.61± 0.13) •10^{10}	(2.79± 0.25) •10^{10}	(8.46± 0.68) •10^{10}
Position 7	(4.08± 0.33) •10^{10}	(1.60± 0.13) •10^{10}	(2.71± 0.24) •10^{10}	(8.38± 0.67) •10^{10}
Position 8	(3.71± 0.30) •10^{10}	(1.46± 0.12) •10^{10}	(2.35± 0.21) •10^{10}	(7.51± 0.60) •10^{10}
Position 9	(2.96± 0.24) •10^{10}	(1.36± 0.11) •10^{10}	(1.90± 0.17) •10^{10}	(6.22± 0.50) •10^{10}
Position 10	(2.13± 0.17) •10^{10}	(9.43± 0.75) •10^{9}	(1.24± 0.11) •10^{10}	(4.31± 0.34) •10^{10}
Position 11	(1.54± 0.12) •10^{10}	(6.25± 0.50) •10^{9}	(6.30± 0.57) •10^{9}	(2.79± 0.22) •10^{10}
Radial core direction				
Position b	(3.69± 0.29) •10^{10}	(1.88± 0.15) •10^{10}	(1.69± 0.15) •10^{10}	(7.26± 0.58) •10^{10}
Position i	(2.44± 0.19) •10^{10}	(1.43± 0.11) •10^{10}	(1.20± 0.11) •10^{10}	(5.08± 0.41) •10^{10}
Position o	(1.33± 0.11) •10^{10}	(7.33± 0.59) •10^{9}	(5.76± 0.52) •10^{9}	(2.63± 0.21) •10^{10}

Table 2.8: Integral flux densities for each characterized in-core position referred at 1kW reactor power.

2.3 Out of core flux determination: Horizontal Beam Tube and Lazy Susan

Part of the present flux characterization at the TU Wien TRIGA reactor consisted in investigating some out of core irradiation facilities.

The first one was one of the reactor horizontal beam tubes, the Beam Tube B. In this case, the knowledge of the neutron energy spectrum along the beam tube was of interest for the study of a new thermal white neutron beam. The experimental data obtained were then utilized as input for the design of the new device, leading eventually to its installation[14] at the Beam Tube B.

The second investigated out of core facility was the so called Lazy Susan facility (see 1.5.6). The justification of this neutron flux measurement was directly related to the present research project. In fact, some fissile and fertile materials were supposed to be later irradiated in the reactor (see Chapter 4): that should require the utilization of a dry irradiation facility with a well known neutron spectrum, like the Lazy Susan.

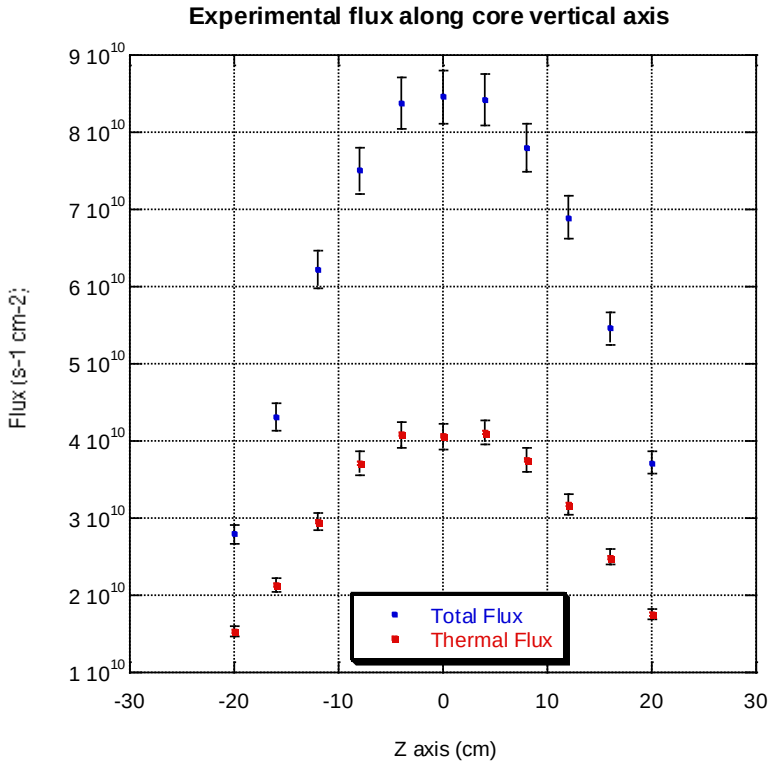

Figure 2.9: Plot of experimental flux values along the core vertical axis in the Central Thimble (CT). Total flux and Thermal flux values are shown in the 11 positions along the vertical axis (z axis).

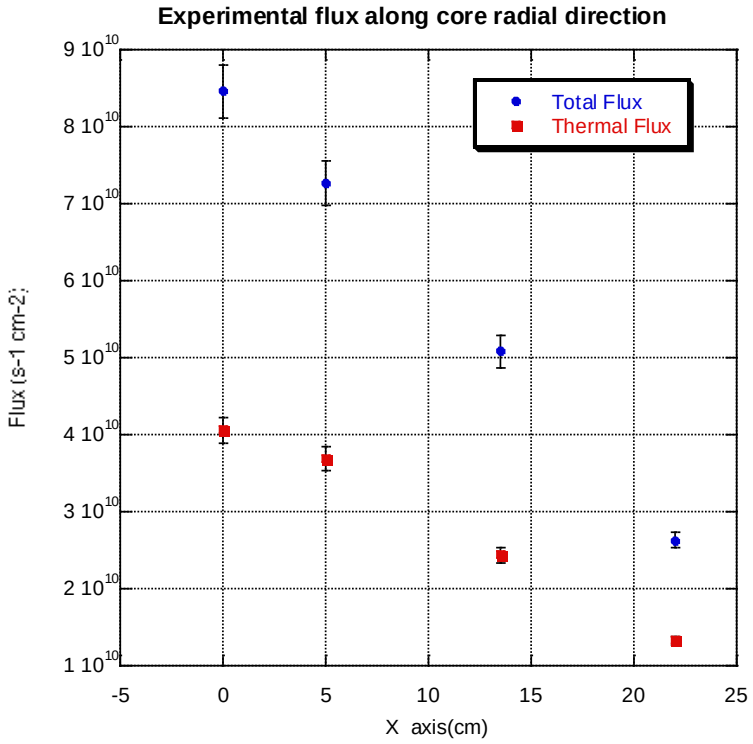

Figure 2. 10: Plot of Thermal and Total experimental flux values along the radial direction of the reactor core. On the x axis, the distances are referred from reactor equatorial position (x,y,z=0,0,0).

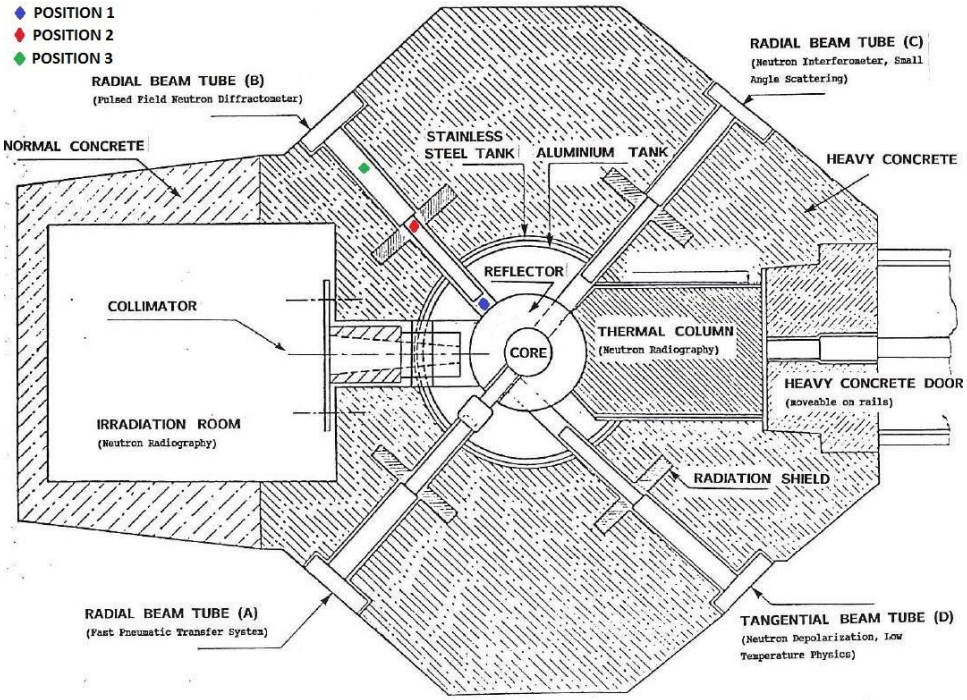

Figure 2.11: Irradiation positions in the horizontal beam tube. Position 1, 2 and 3 are represented in colour blue, red and green respectively.

2.3.1 Target foils irradiation and measurements

Horizontal beam tube B

At the TRIGA reactor of TU Wien the horizontal beam tubes are all utilized for ongoing experiments. For this reason, the decision to carry out the reactor characterization at the Beam Tube B was due to the opportunity to perform foils irradiations during a special inspection of the beam tube. At this occasion, the Beam Tube B was opened and the collimator that normally occupies the beam tube, was extracted for inspection and verification.

It has to be pointed out that the setting of this experiment was strongly influenced by the limited time available for the irradiation of the foils and radiation protection constraints; i.e. few days of reactor availability in the described conditions and limitation of reactor power level. Due to these constrains it became necessary to schedule irradiations in only 3 positions along the beam tube and, for each position, all target foils had to be irradiated at the same time.

Irradiation Position	Distance from reflector (cm)	Irradiated foils	Reactor Power (kW)	Irradiation time (min)
Position 1	5	Au; Au(Cd); Cu; In(Cd); NI,Fe, Al	10	30
Position 2	125	Au; Au(Cd); Cu; In(Cd); NI,Fe, Al	10	30
Position3	185	Au; Au(Cd); Cu;	10	60

Table 2.9: Irradiations performed in the horizontal beam tube B.

Accordingly, the irradiations time and the reactor power were set in order to optimize the measurement of the irradiated foils (activity, cooling-down time, counting time).

The irradiation positions were defined as in Table 2.9; the distances are taken from the graphite reflector and the location of the irradiation positions is shown by the markers in Figure 2.11.

As explained above, a complete foil set (see Table 2.2) was irradiated at the same time in one of the three defined positions, it was important to extract samples and start measurement soon after end of irradiation in order to detect the reaction $^{27}Al(n,p)^{27}Mg$ (Mg-27 half-life being approximately 9 min). Hence a proper wood sample holder was designed for this irradiation campaign.
Figure 2.12 shows the irradiation device and its positioning inside the beam tube.
In Position 1 and 2, the whole set of foils was irradiated; in Position 3, only three foils (Au, Au(Cd) and Cu) were used, because the irradiation power and time was limited and most of the samples would not have been activated properly under the given circumstances.
The reactor power was always 10 kW, the irradiation time was 30 min, except for the irradiation in the third position, for which the time was 60 min in order to compensate for the reduced neutron flux. The specifics of the single irradiations can be seen in Table 2.9.
Following the irradiations, for each foil the activity was measured by means of the same HPGe gamma detector previously described (see 2.2.1).

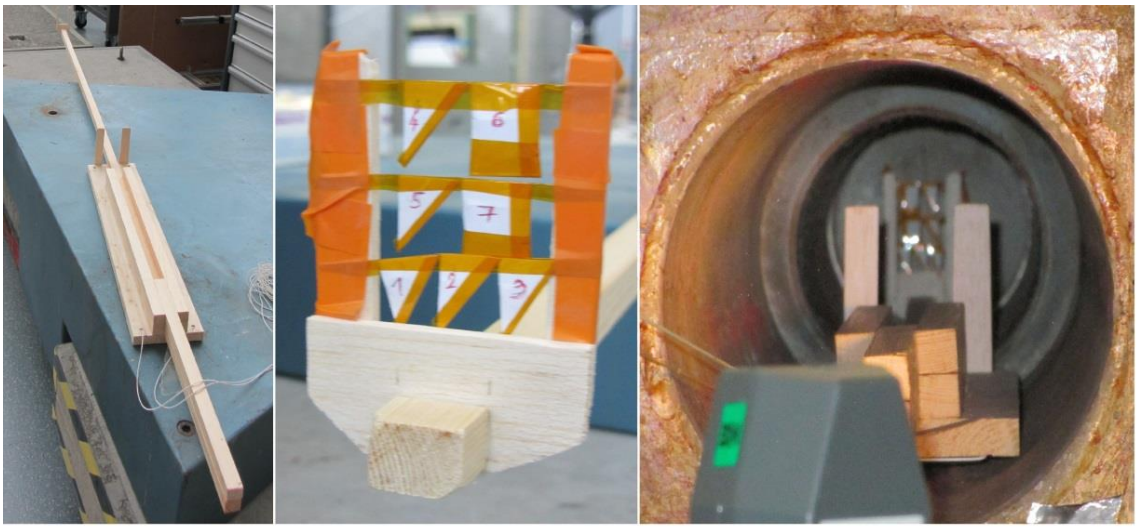

Figure 2.12: Irradiation device used for foils irradiation in Beam Tube B; foils contained in separate paper bags ready for irradiation; positioning of the device inside the horizontal beam tube.

The values of measured specific activities per atom at the end of irradiation and extrapolated to saturation are listed in Table 2.10 for each material foil in the three irradiation positions.

Considering the optimization of cooling-down and counting time of the foils, statistical uncertainties of the measurements were evaluated for less than 3%. To investigate the systematic error several repeated measurements of an irradiated foil of gold were performed, every time repositioning the foil on the detector. The error was evaluated to less than 2% giving a total uncertainty of the gamma spectrometry measurements of about ± 5%.

Position 1		Position 2		Position 3	
Foil	**Activities (Bq/atom)**	**Foil**	**Activities (Bq/atom)**	**Foil**	**Activities (Bq/atom)**
AU	$(6.14\pm0.30)\cdot10^{-11}$	AU	$(2.70\pm0.13)\cdot10^{-13}$	AU	$(8.43\pm0.42)\cdot10^{-14}$
AU(Cd)	$(4.52\pm0.23)\cdot10^{-11}$	AU(Cd)	$(1.68\pm0.08)\cdot10^{-13}$	AU(Cd)	$(5.78\pm0.29)\cdot10^{-14}$
CU	$(1.22\pm0.06)\cdot10^{-12}$	CU	$(5.04\pm0.25)\cdot10^{-15}$	CU	$(1.18\pm0.06)\cdot10^{-15}$
AL	$(2.06\pm0.10)\cdot10^{-16}$	AL	$(6.11\pm0.30)\cdot10^{-18}$		
NI	$(6.20\pm0.31)\cdot10^{-15}$	NI	$(1.67\pm0.08)\cdot10^{-16}$		
FE	$(3.34\pm0.17)\cdot10^{-15}$	IN (Cd)	$(1.98\pm0.10)\cdot10^{-16}$		
IN(Cd)	$(8.09\pm0.40)\cdot10^{-15}$				

Table 2.10: Measured specific activities per atom extrapolated to saturation for foils irradiated in Beam Tube B (Position 1, Position 2 and Position 3). Values are reported at the reactor power of 250 kW.

Irradiation Position	Irradiation Id.	Irradiated foils	Reactor Power (kW)	Irradiation time (min)
LS1	LS1.1	Au; Cu; NI, Fe, Al	10	10
	LS1.2	Au(Cd); Cu; In(Cd)	10	10

Table 2.11: Irradiation setting and foils in the Lazy Susan position.

Lazy Susan

The Lazy Susan (LS) position is the second out of core irradiation position that was characterized during this work. One of the reasons for performing the characterization of LS facility was that it consists of a dry irradiation position with a quite high flux (about 10^{12} $n \bullet s^{-1} \bullet cm^{-2}$). This characteristic makes it suitable for the subsequent irradiation of fissile and fertile material foils (see 4.1). Among the 5 available irradiation position in the LS, the position identified as LS1 was selected.

The foil set to be irradiated remained unchanged from the in-core irradiations (see Table 2.2). For irradiation in LS1, the foil set was divided (Table 2.11) in two irradiations (LS1.1, LS1.2) at the same reactor power (10kW) and same duration (10 minutes). The Cu foil irradiation was replicated also in the second irradiation (LS1.2) to be used as flux monitor.

Following the irradiations, the activity of the foils was measured by means of the same HPGe gamma detector described in 2.2.1 and results in terms of specific activity per atom at the end of irradiation and extrapolated to saturation are listed in Table 2.12.

The activity values of the Copper foils used as flux monitors differ for less than 2%, showing a very good consistence among the two irradiation. Then no correction was applied to the measured activity values in the LS1 position.

Position LS1	
Foil	**Activities (Bq/atom)**
AU	$(8.04\pm0.40)\cdot10^{-12}$
AU(Cd)	$(2.63\pm0.13)\cdot10^{-12}$
CU(LS1.1)	$(2.28\pm0.11)\cdot10^{-13}$
CU(LS1.2)	$(2.33\pm0.11)\cdot10^{-13}$
AL	$(3.23\pm0.16)\cdot10^{-17}$
NI	$(7.37\pm0.36)\cdot10^{-16}$
FE	$(6.33\pm0.31)\cdot10^{-16}$
IN(Cd)	$(3.15\pm0.15)\cdot10^{-15}$

Table 2.12: Measured specific activities per atom extrapolated to saturation for foils irradiated in Lazy Susan (LS1) position at 10 kW reactor power.

2.3.2 Out of core neutron flux experimental results

Horizontal beam tube B

As for the Central Thimble, the measured specific activities extrapolated to saturation have been used as input for the SAND II code in order to evaluate the neutron energy spectrum.

Since from original data and drawings of the reactor it was not clear if the Beam Tube B faces the graphite or a cavity in correspondence of the reflector, one of the purposes of this work was also to clarify this issue. For this reason, the SAND II code was run alternatively using two different input guess fluxes both generated by MCNP calculation: one guess flux was calculated considering the configuration facing graphite inside the reflector, the other facing a void volume inside the reflector. The considerable difference in the two Guess fluxes obtained by MCNP, did not affect the final results obtained by SAND II calculation; this result is considered a confirmation of the capability of SAND II code to build up the measured energy spectrum regardless of the absolute value and, partially, of the energy distribution of the guess flux.

As a result, the SAND II code provided the differential fluxes distributed over 621 energy values in the range between 10^{-10} MeV and 18 MeV: Figure 2.13 and Figure 2.14 show respectively the Differential and Integral Flux in each of the 3 irradiation positions as provided by SAND II code.

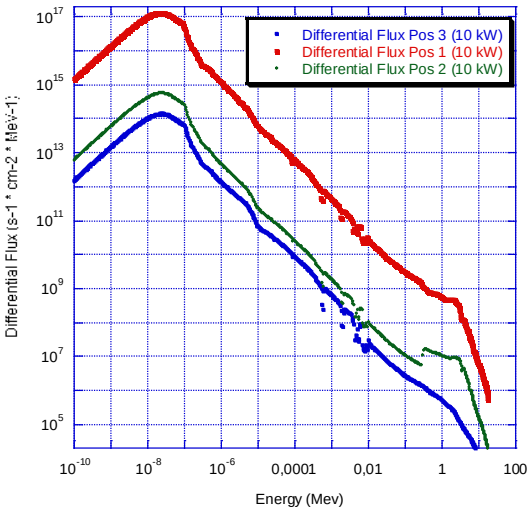

Figure 2.13: Experimental Differential Flux at 10kW in Beam Tube B (Position 1,2,3)

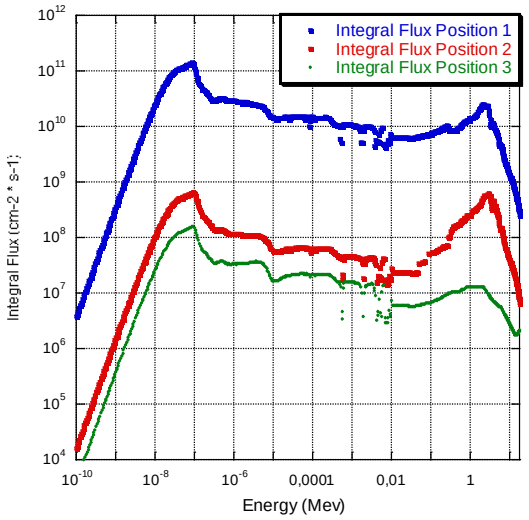

Figure 2.14: Experimental Integral Flux in Beam Tube B (Position 1,2,3) (250kW).

The integral flux values over the Thermal (E<0.55 eV), Epithermal (0.55 eV < E < 100 keV) and Fast (E>100 keV) neutron energy intervals was calculated from the obtained SAND II neutron flux distribution and is reported in Table 2.13.

Considering the values obtained for the total Integral Flux in the 3 position, it was possible to build the best fit for the integral flux values along the Beam Tube B (Figure 2.15) and accordingly evaluate the integral flux in correspondence of various distances, such as (by extrapolation) at the beam port. The estimated value of the total integral flux in correspondence of the beam port of Beam Tube B was of $1.76 \cdot 10^{8}$ $s^{-1} \cdot cm^{-2}$. Experimental results obtained will be benchmarked with MCNP calculation (see Chapter 3) for evaluation of which configuration, with or without graphite in the reflector, corresponds to the Beam Tube B.

The uncertainties of the differential and integral neutron fluxes were evaluated taking into account the propagation of the uncertainties of the foils measurements in the SAND II de-convolution process; the uncertainties related to the determination of the weight of the foils (less than 1%); the thermal power calibration of the reactor performed according to specific procedure using certified instrumentation (about ± 3%). The uncertainties of the flux values resulted to be within ± 10%.

	Total Flux ($cm^{-2} \cdot s^{-1}$)	**Thermal Flux (<0.69eV)** ($cm^{-2} \cdot s^{-1}$)	**Epithermal Flux (0.69eV-110keV)** ($cm^{-2} \cdot s^{-1}$)	**Fast Flux (100keV-18MeV)** ($cm^{-2} \cdot s^{-1}$)
Position 1	$(5.74\pm0.50)\cdot10^{11}$	$(3.28\pm0.30)\cdot10^{11}$	$(1.73\pm0.15)\cdot10^{11}$	$(7.28\pm0.70)\cdot10^{10}$
Position 2	$(3.13\pm0.30)\cdot10^{9}$	$(1.40\pm0.10)\cdot10^{9}$	$(7.11\pm0.70)\cdot10^{8}$	$(1.02\pm0.10)\cdot10^{9}$
Position 3	$(6.04\pm0.60)\cdot10^{8}$	$(3.39\pm0.30)\cdot10^{8}$	$(2.22\pm0.20)\cdot10^{8}$	$(4.43\pm0.40)\cdot10^{7}$

Table 2. 13: Thermal (E<0.69 eV), Epithermal (0.69 eV < E < 100 keV) and Fast (E>100 keV) neutron flux in Beam Tube B (values reported at reactor power of 250 kW).

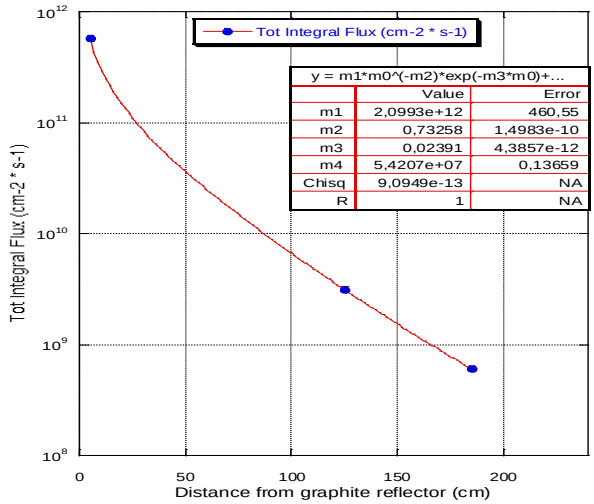

Figure 2. 15: Fit of the total flux experimental values along the horizontal Beam Tube B.

Lazy Susan

With the same methodology as for the previous irradiation positions, the measured specific activities of the samples irradiated in the LS1 position were extrapolated to saturation and provided as input for the SAND II code.

The neutron energy spectrum was then produced as differential flux distributed over 621 energy values in the range between 10^{-10} and 18 MeV: Figure 2.16 shows the differential flux obtained for LS1 in comparison to the one determined in the equatorial position (Position 6) of the reactor.

The integral neutron flux values over the Thermal-, Epithermal- and Fast-energy intervals is reported in Table 2.14.

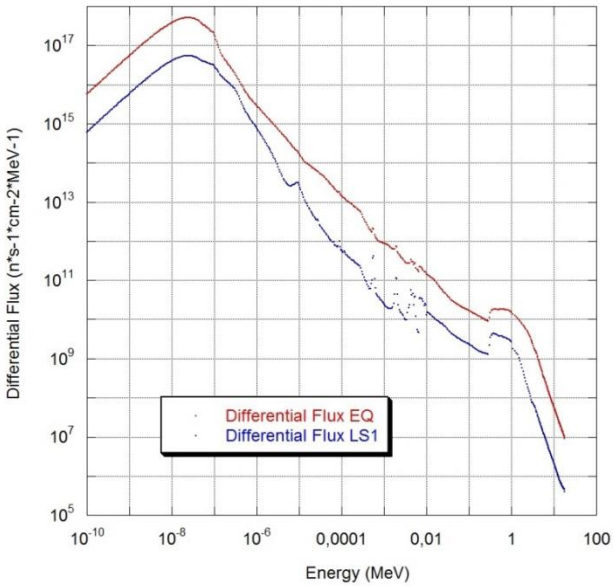

Figure 2.16: Neutron spectrum obtained in Lazy Susan position (LS1) is compared to the neutron spectrum in the center of the core (EQ position = POS6).

	Total Flux ($cm^{-2} \cdot s^{-1}$)	**Thermal Flux (<0.55eV)** ($cm^{-2} \cdot s^{-1}$)	**Epithermal Flux (0.55eV-100keV)** ($cm^{-2} \cdot s^{-1}$)	**Fast Flux (100keV-18MeV)** ($cm^{-2} \cdot s^{-1}$)
Position LS1	$(3.69\pm0.31)\cdot10^{12}$	$(2.05\pm0.17)\cdot10^{12}$	$(5.59\pm0.50)\cdot10^{11}$	$(1.08\pm0.13)\cdot10^{12}$

Table 2.14: Neutron flux values obtained in the Lazy Susan position LS1 values reported at reactor power of 250 kW).

2.4 Uncertainties evaluation

Due to the optimization of irradiation and counting time of the foils, statistical uncertainties of the measurements together with uncertainties related to the detector efficiency calibration were evaluated for less than 3%. Systematic error due to the positioning of the foils on the detector was investigated separately performing several repeated measurements of an irradiated foil of gold, every time repositioning it on the detector. The error was evaluated in less than 2% giving a total uncertainty of the gamma spectrometry measurements about ± 5%. The SAND II program gives as result a differential neutron spectrum without uncertainties. In this work, the method adopted to calculate the propagation of the uncertainties of the measured activities in the de-convolution process, is based on a multiple run (100 for each irradiation position) of the SAND II program with different sets of measured activities input data (see §2.2.3). The set of values were calculated fitting a Student's t-distribution with mean equal to the average measured activity and standard deviation equal to the uncertainty

of the gamma spectrometry measurement. As result, one hundred differential neutron flux densities for each irradiation position were calculated and, for each energy, the average value and the variance were evaluated. The average flux differential density evaluated in this way is affected by a standard deviation which varies from 4% to 20% through the 621 energy intervals. The group flux densities were evaluated integrating the average flux differential densities: the uncertainties over the energy groups, evaluated according to the error propagation rules, were less than 2%.

In addition, two more factors contributed to the total uncertainty: the foils weighting process and the reactor operational parameters measurement.

The measurement of the foils weight was performed using an analytical balance with accuracy in the order of 0.05 mg. Thus, the uncertainty related to the determination of the foils weight is evaluated about 1% for gold foils and much less than 1% for other materials foils.

The thermal power calibration of the reactor is performed according to the specific procedure using certified instrumentation. Taking into account all the uncertainties of the procedure, the power calibration measurement is affected by an uncertainty of about ± 5%. The reactor power automatic control allows to stabilize the power level during the irradiation of the samples with a precision of ± 0.5%. Thus, the neutron flux density value, during reactor operation, is affected by an uncertainty of about ± 6% due to reactor operational parameters measurement.

Taking into account all contributions, the total uncertainty of the integral flux densities were within 9%.

Chapter 3

MCNP6 reactor model validation

This chapter describes one of the computational tasks performed during this PhD work: the implementation of the TU Wien TRIGA reactor new model with MCNP6 and its validation against experimental data.
An introduction to MCNP6 Monte Carlo code is provided first (3.1), including the description of its main new capabilities compared with previous MCNP5/MCNPX versions, as well as the MCNP physics and the particle treatment.
Subsequently the reactor model implementation (3.2) is described with indication of the level of detail in the modelling procedure, like for example choices for the source simulation option and the calculation parameters. The calculations are then performed in correspondence of the previously experimentally characterized positions (see Chapter 2) and results are reported (3.3). The comparison of calculated and experimental results is discussed (3.4) and an evaluation is performed about the MCNP6 reactor model capability of well reproducing the TRIGA reactor neutron flux and neutron spectrum behaviour.

3.1. MCNP6 code

The MCNP (Monte Carlo N–Particle) Code is one of the best known and most utilized Monte Carlo code in reactor physics developed at Los Alamos National Laboratory (LANL) dating from the 1940s. The MCNP code has been expanded ever since to include more and more particle types: 37 different particle types can be currently transported for criticality, shielding, dosimetry, detector response, and many other applications.

The last release version MCNP6.1[13] represent a general-purpose, continuous-energy, generalized-geometry, time dependent, Monte Carlo radiation-transport code designed to track many particle types over broad ranges of energies. MCNP6 is the merge result of the MCNP5 and MCNPX codes into a single product comprising all features of both. The code presents a set of new features that include the possibility to handle a multitude of particles and to include model physics options for energies above the cross-section table range, a material burnup feature, and delayed particle production. Expanded and new tally, source, and variance-reduction options are available as well as an improved plotting capability.

In addition to the code capabilities of MCNP5 and MCNPX, MCNP6 includes several significant new capabilities not found in the previous versions of the codes. The main new capabilities are the following:

- Adjoint-based sensitivity coefficients: MCNP6 contains the new ability to compute sensitivity profiles of k_{eff} (ksen card) with continuous-energy physics for cross sections, fission multiplicities ν and spectra χ, and scattering distributions. This is useful for identifying the criticality benchmarks that are similar to applications being analysed, which is important for understanding how well MCNP6 and its data libraries perform for that particular application through quantifying uncertainties and biases.
- Low energy photon and electron transport for atomic cross sections: MCNP6 has extended the minimum energy cut-off for photon transport down to 1 eV; and for electron transport down to 10eV.
- Explicit tracking of all charged particles in magnetic fields: MCNP6 can model magnetic fields in low density materials, such as air. This new capability is an alternative to the existing particle tracking in a magnetic field in a vacuum, i.e. in a void cell.
- Uncollided secondaries: historically, an uncollided particle in MCNP was any particle that had not undergone a collision since its creation as a source particle or as a secondary particle. A new cell card (unc) has been added to MCNP6 that allows the user to control if secondaries are born as uncollided or collided particles.
- New MCNP6 Depletion Capabilities: MCNP6 depletion (BURN card) enables complete depletion calculations in a single Monte Carlo code and include: (1) new performance enhancing parallel architecture that implements both shared and distributed memory constructs; (2) enhanced memory management that maximizes calculation fidelity; and (3) improved burnup physics for better nuclide prediction; (4) added swapb keyword on

the burn card, which allows universe swapping at each time step during the burn to mimic fuel shuffling at the assembly and pin levels.

- Background source option (SDEF card, PAR option): A database of background neutrons and gammas for different locations on the Earth's surface has been added and is available as a source particle type on the SDEF card.
- Delayed Beta treatment (ACT card): Enhancements were made to the delayed-particle treatment, including an improvement to the delayed-neutron spectra.
- Spontaneous beta source option (SDEF card, PAR keyword): The spontaneous source option on the SDEF card was extended to include the production of neutrons and betas from spontaneous decay of unstable radionuclides.
- Continuous thermal scattering laws S(α,β): Differently from previous data scattered neutrons at discrete directions, the new thermal scattering data S(α,β) in ENDF/B-VII.1 (extension .20t, e.g. light-water is lwtr.20t) is continuous in energy and scattering angle., The use of the ENDF/B-VII.1 continuous thermal scattering laws should exclusively be used in MCNP6, as both versions MCNP5 and MCNPX present a bug in the sampling procedure that would lead to slightly incorrect answers and eventually would cause the code to crash or enter an infinite loop.
- Perturbations for k_{eff}: The old perturbation capability (the differential operator or PERT) in MCNP5 and MCNPX did not consider the effect of the perturbation on the fission source and it could be used reliably only in fixed-source or SDEF problems (not in eigenvalue or KCODE problems). An integral method based on adjoint functions was developed in MCNP6 that correctly computes perturbations for k_{eff} in KCODE problems.

Currently MCNP6 is continuously under development in several widely disparate fields of Monte Carlo particle transport. The future improvement will consider aspects like adding molecular interaction cross sections for both photons and electrons; improving the optical light transport with reflection and refraction; improving the energy and time signatures of delayed particle emissions; merging the unstructured mesh capability with the other +features; and improving of the temperature effects on neutron interactions.

3.1.1. MCNP Physics

As the essence of MCNP is the physics of particle interactions, to describe the operation of this program it is essential to dwell on the concepts of particle weight and trace.

In a particle transport simulation, there are two possibilities: the first implies to follow the so-called *analog* model, according to which each particle of MCNP represents a real particle with *weight* w=1 (this strategy is applicable if a sufficiently high number of particles contributes to the result); the second possibility consists instead in the *not-analog* simulation, advisable in case it is necessary to force the probability that a particle contributes to the desired quantity (without polarizing the result) improving the efficiency of calculation (in this case, the *weight w* of each source generated particle may be different from the unit, thus allowing a more effective sampling of the regions of greatest interest, through the relative enhancement of the statistics).

To every generated particle, a *trace* is also associated that follows its history, that is the evolution of the particle from the moment in which it is generated up to that in which it is absorbed or escapes. When tracking the interaction of a particle in a region with fixed composition, the probability for a collision to occur between l and l + dl is:

$$p(l)dl = e^{-\Sigma_t l}\,\Sigma_t\,dl \tag{3.20}$$

Where $\boldsymbol{\Sigma}_t$ is the macroscopic total cross section. If ξ is a random number uniformly distributed in the interval [0,1]:

$$\xi = \int_0^l p(l)\,dl = \int_0^l e^{-\Sigma_t s}\,\Sigma_t\,ds = 1 - e^{-\Sigma_t l} \tag{3.21}$$

As $(1-\xi)$ is distributed same as ξ, the collision distance will result:

$$l = -\frac{1}{\Sigma_t}\ln(1-\xi) = -\frac{1}{\Sigma_t}\ln(\xi) \tag{3.22}$$

Figure 3.1 represents the random *history* of a neutron incident on a material that can undergo fission. MCNP randomly selects ξ values between 0 and 1 to determine what and where interaction takes place, based on the rules (physics) and probabilities (transport data) governing the processes and materials involved.

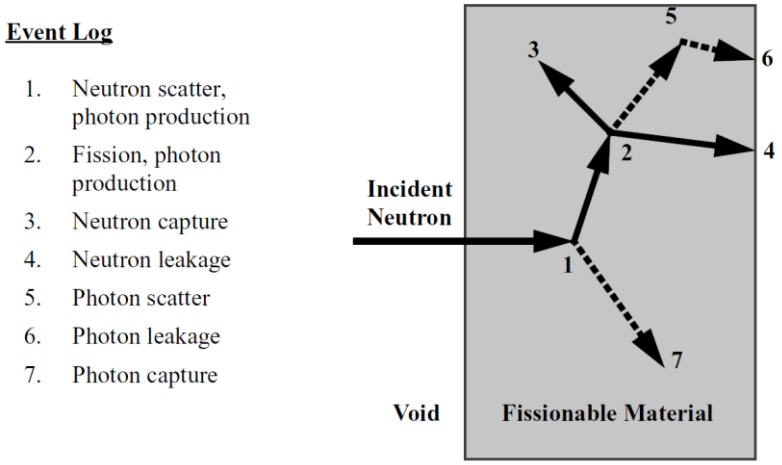

Figure 3. 1: representation of the random history of a neutron incident on a material that can undergo fission [13].

3.1.2. Neutron interactions

When a particle (which represents a number of neutrons that depends upon the particle weight) collides with a nucleus, MCNP actuates the following processes:

Identification of Collision Nuclide

If the material in which the collision occurred is composed of n different nuclides, and if ξ is a random number in the interval [0,1], then the k^{th} nuclide is chosen as the collision nuclide if the following equation is satisfied:

$$\sum_{i=1}^{k-1} \Sigma_{ti} < \xi \sum_{i=1}^{n} \Sigma_{ti} \qquad (3.23)$$

Where Σ_{ti} is the macroscopic total cross section of i^{th} nuclide. If the energy of the neutron is low enough (below about 4 eV), the total cross section is the sum of the capture cross section from the regular cross-section table and the elastic and inelastic scattering cross sections from the table. Otherwise, the total cross section is taken from the regular cross-section table and is adjusted for thermal effects as described below.

Free Gas Thermal Treatment or $S(\alpha,\beta)$ Treatment

The free gas thermal treatment in MCNP assumes that the medium is a free gas. This approximation is justified to account for the thermal motion of the interacting atom and for the presence of other atoms nearby. As a consequence, the elastic scattering cross section at zero temperature is nearly independent of the energy of the neutron, and the reaction cross sections are nearly independent of temperature. With the above assumptions, the free gas thermal treatment consists of adjusting the elastic cross section and taking into account the velocity of the target nucleus when the kinematics of a collision are being calculated.

The $S(\alpha,\beta)$[15,16] treatment instead takes into account the effects of chemical binding and crystal structure for incident neutron energies below about 4 eV, but is available for only a limited number of substances and temperatures. In this case, two processes are allowed: the first is the elastic scattering (σ_{el}), with no change in the outgoing neutron energy, chosen with probability $\sigma_{el}/(\sigma_{el} + \sigma_{in})$; the second is the inelastic scattering (σ_{in}) with energy distribution of the outgoing neutron selected from a set of equally probable energies in the interval [10^{-5}eV, 4eV], along with a diffusion angle evaluated basing on the initial and final energy.

Optional Generation of Photons

Photons generation[17] takes place if the problem is a combined neutron/photon run and if the collision nuclide has a nonzero photon production cross section. The number of photons produced is a function of neutron weight, neutron source weight, photon production cross section, neutron total cross section, importance of the neutron source cell and of the cell in which the interaction takes place. In a KCODE calculation, secondary photon production from neutrons is turned off during the inactive cycles.

Neutron absorption is modelled

Absorption is treated in one of two ways: analog or implicit. For fissile nuclides, "absorption" includes both capture and fission reactions. In analog absorption, the particle is killed with probability σ_a/σ_t , where σ_a and σ_t are the absorption and total cross sections ($\sigma_t = \sigma_{el} + \sigma_{an} + \sigma_a$) of the collision nuclide at the

incoming neutron energy. For all particles killed by analog absorption, the entire particle energy and weight are deposited in the collision cell.

For implicit absorption, the neutron weight W_n is reduced to the quantity:

$$W_n^{'} = \left(1 - \frac{\sigma_a}{\sigma_t}\right) W_n \tag{3.24}$$

and only a fraction σ_a/σ_t of the original particle weight is deposited in the collision cell. Implicit absorption is the default method of neutron absorption in MCNP.

Elastic or Inelastic Scattering selection

If the conditions for the S(α,β) treatment are not met, the particle undergoes either an elastic or inelastic collision. The selection of an elastic collision is made with the probability:

$$\frac{\sigma_{el}}{\sigma_{an} + \sigma_{el}} = \frac{\sigma_{el}}{\sigma_t - \sigma_a} \tag{3.25}$$

The selection of an inelastic collision is made with the remaining probability. If the collision is determined to be inelastic, the type of inelastic reaction, *n*, is sampled from:

$$\sum_{i=1}^{n-1} \sigma_i < \xi \sum_{i=1}^{N} \sigma_i \leq \sum_{i=1}^{n} \sigma_i \tag{3.26}$$

where ξ is a random number on the interval [0,1], N is the number of inelastic reactions, and σ_i is the i_{th} inelastic reaction cross section at the incident neutron energy. If the energy of the neutron is low enough and an appropriate $S(\alpha,\beta)$ table is present, the collision is modeled by the $S(\alpha,\beta)$ treatment instead of by elastic/inelastic scattering selection.

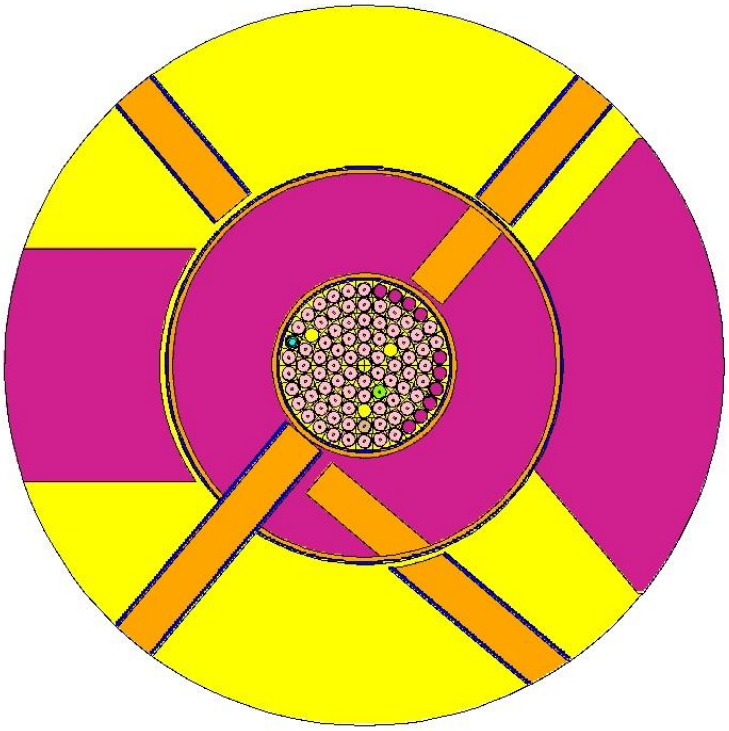

Figure 3.2: The horizontal section (z=-15cm) of the TRIGA reactor model as obtained by MCNP6.

3.2. Reactor model implementation for the TRIGA reactor

A model of the TRIGA Mark II research reactor of the Technische Universität Wien (TU Wien) was developed by means of MCNP6 basing on available geometric and material data[6] [7] [8]. The current model includes at the proper level of detail all the components that can affect the evaluation of the neutron flux in-core distribution and the energy spectrum in different in-core positions, including inside the fuel elements; as well as the reactor fuel burn-up and reactor critical parameters.

3.2.1. Geometry description

This model extends up to the reactor water tank. The reactor horizontal section of model obtained by MCNP6 is shown in Figure 3.2, where the graphite reflector, the four horizontal beam tubes, the initial parts of thermal and thermalizing columns are also displayed. The circular ring irradiation facility (Lazy Susan) surrounding the core inside the graphite reflector is also modelled and can be seen in Figure 3.4, as it lays in the upper part of the reflector.

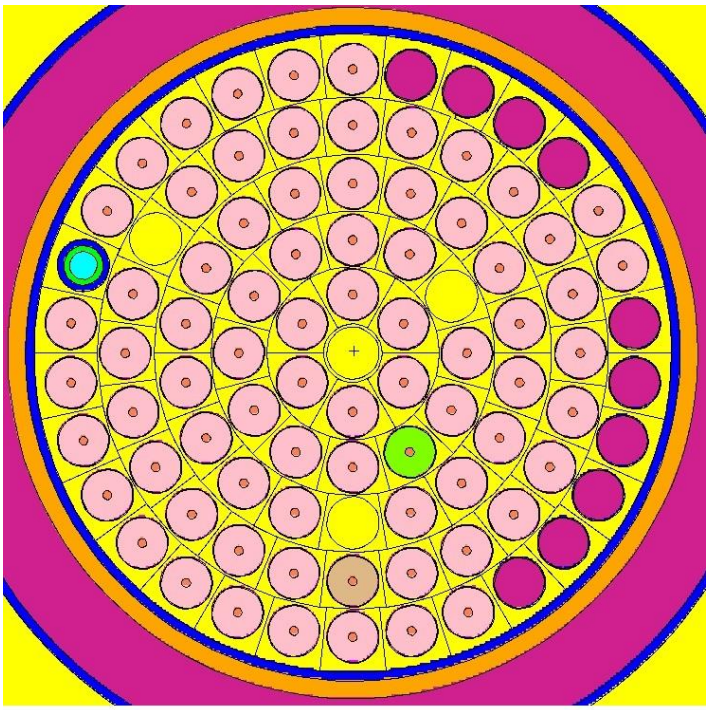

Figure 3.3: The horizontal section (z=0cm) of the TRIGA core modelled by MCNP6.

Due to its configuration (the geometry of a single element appears 90 times in the core lattice), the core of the TRIGA MARK II reactor was modelled through the creation of *repeated structures* in MCNP6. The procedure consisted in defining a reference cell, and then modifying it by means of the card "like n but": from time to time, the new fuel cell was positioned the desired core position (with a cell transformation) and filled with the appropriate universe (i.e. specific geometry and material).

The detail of the reactor core (Figure 3.3) shows the different core component and their current location: the 76 cylindrical FE(s) (pink coloured), including the visible central Zirconium rod; the neutron source (blue coloured, in position F25); the control rods position (in yellow, as they are represented completely extracted); the instrumented FE (green coloured); the graphite elements (purple coloured); the water inside the core (yellow coloured).

The core corresponds to the actual core configuration during the performance of the neutron flux and spectrum characterization described in Chapter 2.

A vertical view of the reactor model including the graphite reflector is shown in Figure 3.4: main components of the FE(s) (such as fuel meat, central Zirconium rod, axial graphite reflectors, stainless steel-cladding) are visible.

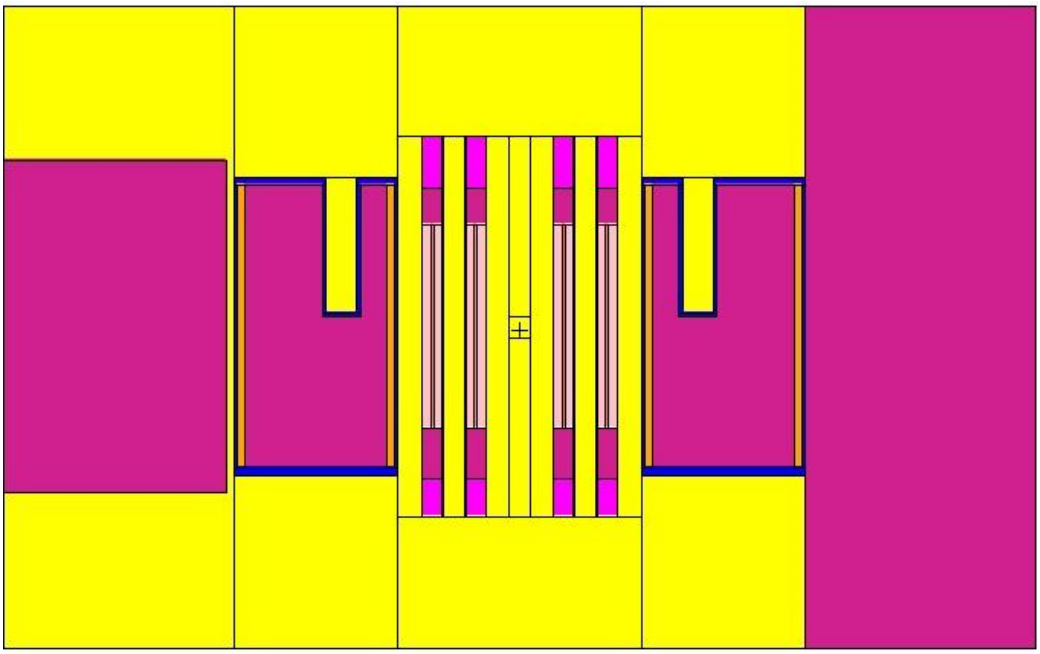

Figure 3.4: Vertical (y=0) view of the reactor model including the graphite reflector, the Lazy Susan, the thermal and thermalizing columns.

3.2.2. Source specification

As for the source specification in MCNP, four types of source are possible: general source (SDEF card), surface source (SSR card), criticality source (KCODE card), or user-supplied source (default if all others are missing). All types can use source distribution functions defined by SIn (Source Information), SPn (Source Probability), SBn (Source Bias), and DSn (Dependent Source Distribution) cards. Independent probability distributions are available to specify the source variables of energy, time, position, direction, and for other parameters such as starting cell(s) or surface(s)[13].

To run a criticality problem, in addition to the geometry description and material cards, it is required to specify the KCODE card and an initial spatial distribution of fission points (using either the KSRC card, the SDEF card, or an SRCTP file). Criticality calculations with MCNP are based on an iterative procedure called "power iteration"[18,19]. After assuming an initial guess for the fission source spatial distribution (i.e., first generation), histories are followed to produce a source for the next fission neutron generation and to estimate a new value for *keff*. Calculating k_{eff} consists of estimating the mean number of fission neutrons

produced in one generation per fission neutron started. A generation is the life of a neutron from birth in fission to death by escape, parasitic capture, or absorption leading to fission.

In MCNP, the computational equivalent of a fission generation is a k_{eff} cycle. Fission neutrons are terminated in each cycle and provide the fission source for the next cycle, a single history can be viewed as continuing from cycle to cycle.

Criticality Problem Definition

To set up a criticality calculation, the KCODE card is used in the input file with the following information:

- the nominal number of source histories, N, per k_{eff} cycle;
- an initial guess of k_{eff};
- the number of source cycles, I_c, to skip before k_{eff} accumulation;
- the total number of cycles, I_t, in the problem.

The initial spatial distribution of fission neutrons can be generated by using (1) the KSRC card with sets of x,y,z point locations, (2) the SDEF card to define points uniformly in volume, or (3) a file (SRCTP) from a previous MCNP criticality calculation. The energy of each source particle for the first *keff* cycle is selected from a generic Watt thermal fission distribution if it is not available from the SRCTP file.

Particle Transport for Each *keff* Cycle

In each *keff* cycle, source particles are started isotropically and transported through the geometry by the standard random walk process, except that fission is treated as capture, either analog or implicit. At each collision point, the following steps are performed for the cycle:

- the three prompt neutron lifetime estimates are accumulated;
- if fission is possible, the three *keff* estimates are accumulated;
- if fission is possible, n ≥0 fission sites at each collision are stored for use as source points in the next cycle;
- the collision nuclide and reaction are sampled but the fission reaction is not allowed to occur because fission is treated as capture. The fission neutrons that would have been created are derived by three different

methods (a collision estimator, an absorption estimator and a track length estimator) to estimate k_{eff} for this cycle.

The neutron prompt removal lifetime is the average time from the emission of a prompt neutron in fission to the removal of the neutron by some physical process.
In the KCODE default mode delayed neutrons are produced as well as prompt neutrons; nevertheless, the neutrons are all born at time zero, then the removal lifetimes calculated in MCNP are prompt removal lifetimes, even if there are delayed neutrons.

k_{eff} Cycle Termination

At the end of each k_{eff} cycle, a new set of M source particles has been derived from fissions in that cycle. The number M varies from cycle to cycle but the total starting weight in each cycle is a constant N. These M particles are written to the SRCTP file at certain cycle intervals. The SRCTP file can be used as the initial source in a subsequent criticality calculation with a similar, though not identical, geometry.

Convergence

The first I_c cycles in a criticality calculation are inactive cycles and are required to make the spatial source changes from the initial definition to the correct distribution for the problem. After the first I_c cycles, the fission source spatial distribution is assumed to have achieved equilibrium, active cycles begin, and k_{eff} and tallies are accumulated. Cycles are run until either a time limit is reached or the total cycles on the KCODE card have been completed.

The neutron source of the current TRIGA reactor model was simulated using the KCODE option with 10000 histories per cycle and 1050 cycles (with the first 50 cycles inactive ones). The initial spatial distribution of fission neutrons was entered by using the KSRC card with set of locations inside different fuel elements.

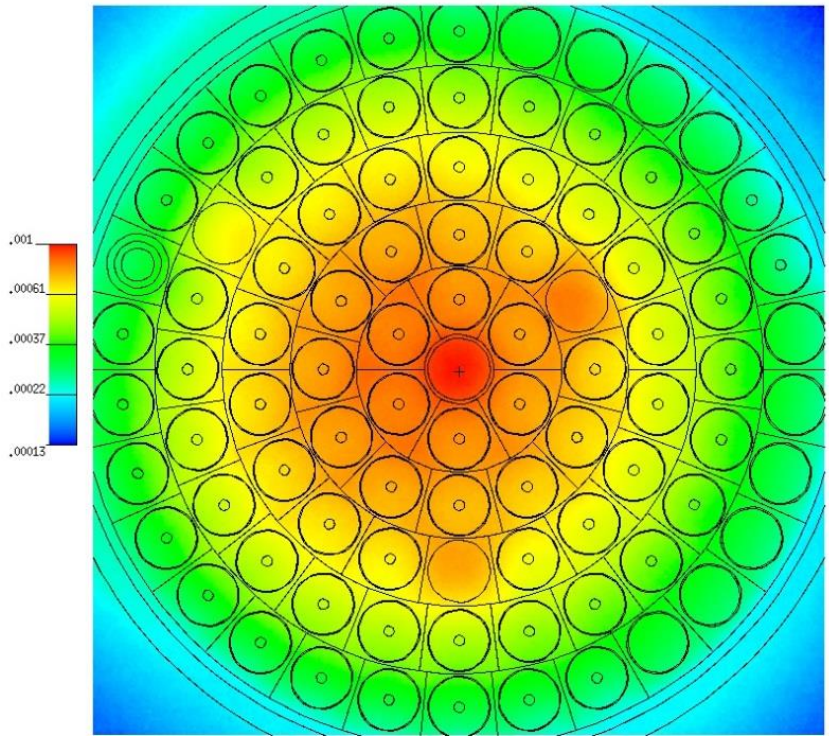

Figure 3. 5: Mesh tally plot of neutron density in the TRIGA reactor core (z=0).

3.3. MCNP flux and neutron spectrum results

The developed MCNP6 TRIGA reactor model was used to calculate the neutron flux and spectrum in the in-core and out of core positions that were characterized by the measurement campaign described in Chapter 2.

The calculation performed with the current MCNP6 reactor model adopted the point detector as standard tally (F5) and produced results in the form of integral neutron flux over 30 energy groups: the width of the energy groups was chosen to represent constant lethargy intervals. Dividing the integral value on each group by the width of the group, a differential flux distribution over 30 energy points was calculated.

In addition to the standard tallies, the special superimposed mesh tally (FMESH card) was also used. This feature allows to tally particles on a mesh independent of the problem geometry. Results are written to a separate output file (MESHTAL) and, for the modelled core, are plotted as shown in Figure 3.5 (plane z=0): the regions in the core with higher neutron population are represented in red, while the blue colour indicates less intensity of neutron density.

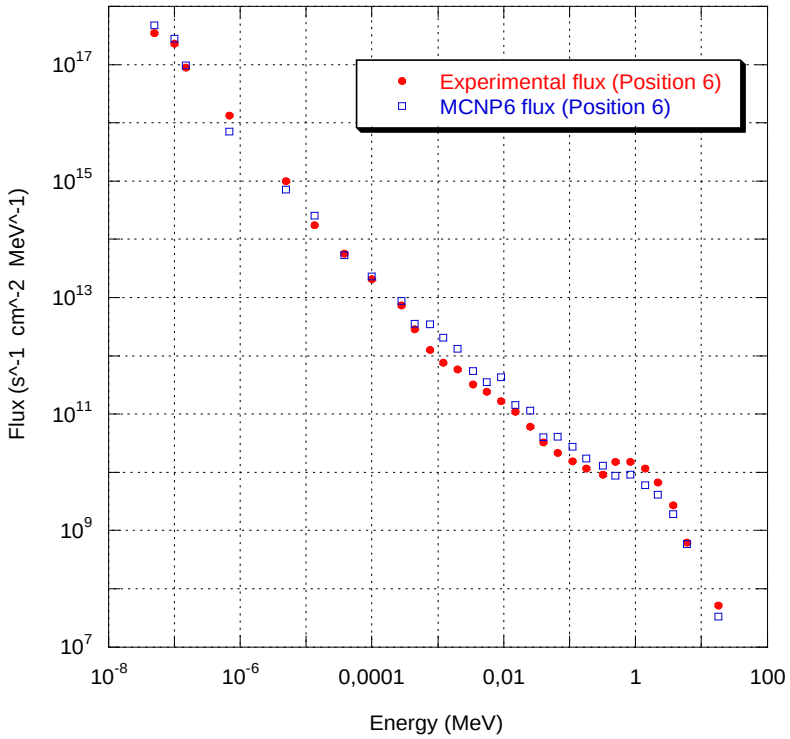

Figure 3. 6: Comparison of experimental and MCNP6 Differential Flux (at 1kW reactor power) in Position 6 (corresponding to core center).

3.3.1. In-core calculation results along radial and vertical direction

As for the in-core positions (see 2.2), the neutron flux and spectrum was calculated in the 11 positions (Figure 2.3) inside the Central Thimble (CT) along the vertical axis and in the 3 positions (Figure 2.4) along the radial direction of the core[20]. Both vertical (POS1, POS2, …POS11) and radial (*b, i, o*) positions in MCNP model corresponded to the distances defined in Table 2.3.

As an example, the comparison between the calculated and measured differential flux over 30 energy points is provided in Figure 3.6 for the position corresponding to the center of the core (POS 6), where the measured 621 energy groups differential flux was also reduced to the corresponding 30 MCNP energy intervals.

MCNP6 flux values were then summed to obtain the total-, thermal- (E<0.69eV), epithermal- (0.69eV-110keV) and fast-flux (110keV-18MeV) component. Results are reported in Table 3.1 for position along core vertical axis (z axis) and in Table 3.2 for positions along core radial direction (x axis).

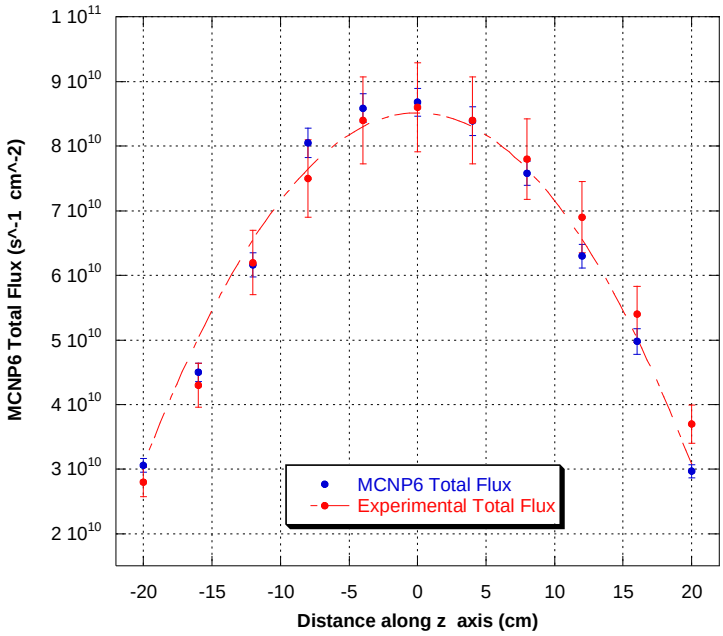

Figure 3. 7: VERTICAL DIRECTION – Comparison of experimental and MCNP6 total neutron fluxes along the vertical core direction (z axis).

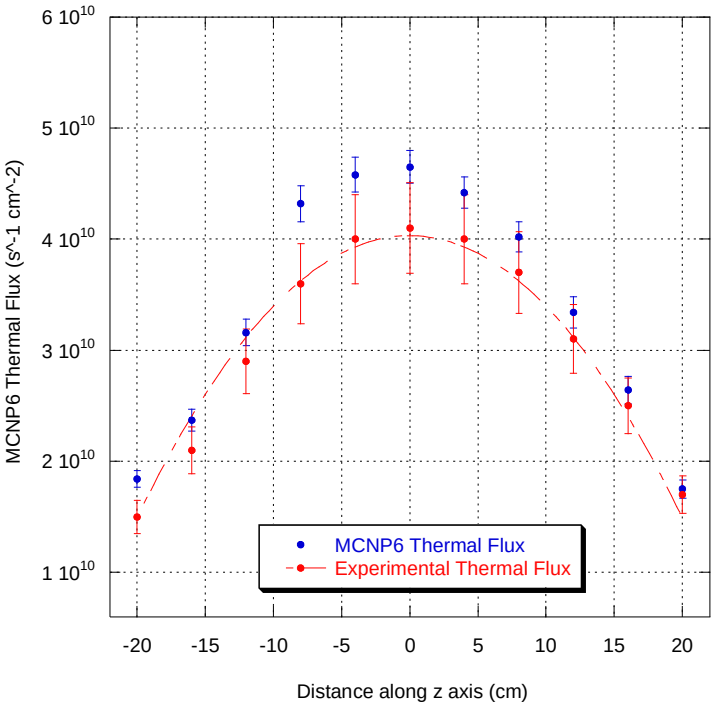

Figure 3. 8: VERTICAL DIRECTION – Comparison of experimental and MCNP6 thermal neutron fluxes along the vertical core direction (z axis).

		MCNP 1 kW			
	Z (cm)	**Total Flux [n •s-1 • cm-2]**	**Thermal flux (<0.69eV) [n •s-1 • cm-2]**	**Epithermal Flux (0.69eV-110keV) [n •s-1 • cm-2]**	**Fast Flux (110keV-18MeV) [n •s-1 • cm-2]**
Position 1	**20**	$2.97 \bullet 10^{10}$	$1.75 \bullet 10^{10}$	$6.69 \bullet 10^{9}$	$5.56 \bullet 10^{9}$
Position 2	**16**	$4.98 \bullet 10^{10}$	$2.64 \bullet 10^{10}$	$1.29 \bullet 10^{10}$	$1.04 \bullet 10^{10}$
Position 3	**12**	$6.30 \bullet 10^{10}$	$3.34 \bullet 10^{10}$	$1.53 \bullet 10^{10}$	$1.44 \bullet 10^{10}$
Position 4	**8**	$7.58 \bullet 10^{10}$	$4.02 \bullet 10^{10}$	$1.84 \bullet 10^{10}$	$1.73 \bullet 10^{10}$
Position 5	**4**	$8.39 \bullet 10^{10}$	$4.42 \bullet 10^{10}$	$2.08 \bullet 10^{10}$	$1.89 \bullet 10^{10}$
Position 6	**0**	$8.68 \bullet 10^{10}$	$4.65 \bullet 10^{10}$	$2.12 \bullet 10^{10}$	$1.91 \bullet 10^{10}$
Position 7	**-4**	$8.59 \bullet 10^{10}$	$4.58 \bullet 10^{10}$	$2.02 \bullet 10^{10}$	$1.99 \bullet 10^{10}$
Position 8	**-8**	$8.05 \bullet 10^{10}$	$4.32 \bullet 10^{10}$	$2.01 \bullet 10^{10}$	$1.72 \bullet 10^{10}$
Position 9	**-12**	$6.16E \bullet 10^{10}$	$3.16 \bullet 10^{10}$	$1.55 \bullet 10^{10}$	$1.45 \bullet 10^{10}$
Position 10	**-16**	$4.50 \bullet 10^{10}$	$2.37 \bullet 10^{10}$	$1.11 \bullet 10^{10}$	$1.02 \bullet 10^{10}$
Position 11	**-20**	$3.06 \bullet 10^{10}$	$1.84 \bullet 10^{10}$	$6.78 \bullet 10^{9}$	$5.40 \bullet 10^{9}$

Table 3.1: the total-, thermal- (E<0.69eV), epithermal- (0.69eV-110keV) and fast-flux (110keV-18MeV) component as obtained by MCNP calculation along the reactor core vertical axis.

		MCNP 1 kW	
Position along x axis	**x (cm)**	**Total Flux [n •s-1 • cm-2]**	**Thermal flux (<0.69eV) [n •s-1 • cm-2]**
Position 6	**0**	$8.68 \bullet 10^{10}$	$4.65 \bullet 10^{10}$
Position b	**-5**	$7.75 \bullet 10^{10}$	$3.07 \bullet 10^{10}$
Position i	**-13.5**	$6.02 \bullet 10^{10}$	$2.21 \bullet 10^{10}$
Position o	**-22**	$2.74 \bullet 10^{10}$	$1.14 \bullet 10^{10}$

Table 3. 2: The total- and thermal- (E<0.69eV) flux component as obtained by MCNP calculation along the reactor core radial direction.

Comparison of experimental and MCNP6 results along the vertical core direction (z axis) are shown in Figure 3.7 and Figure 3.8 for the Total and Thermal flux respectively.

In the same way, the neutron flux behaviour along the core radial direction is displayed in Figures 3.9 and Figure 3.10 for the total and the thermal neutron flux respectively. All values reported are referred to the reactor power of 1 kW.

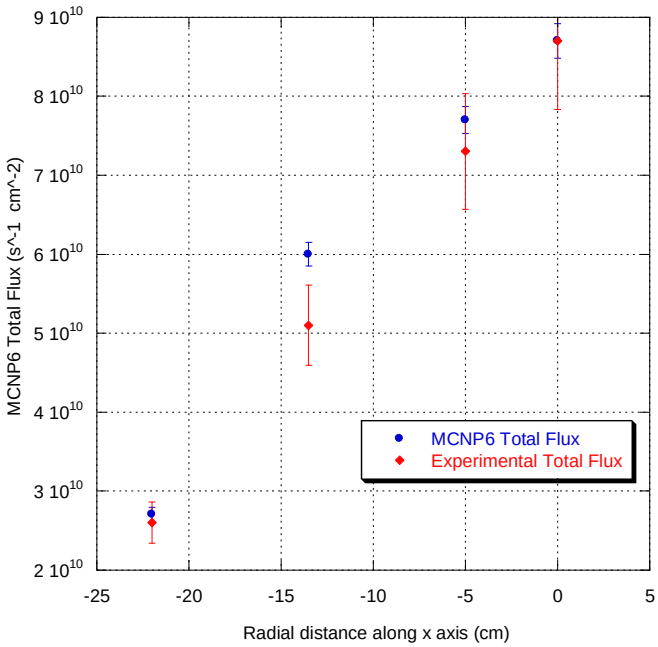

Figure 3. 9: RADIAL DIRECTION - Total neutron fluxes along the radial core direction (x axis) obtained by means of MCNP6 simulation and through measurement.

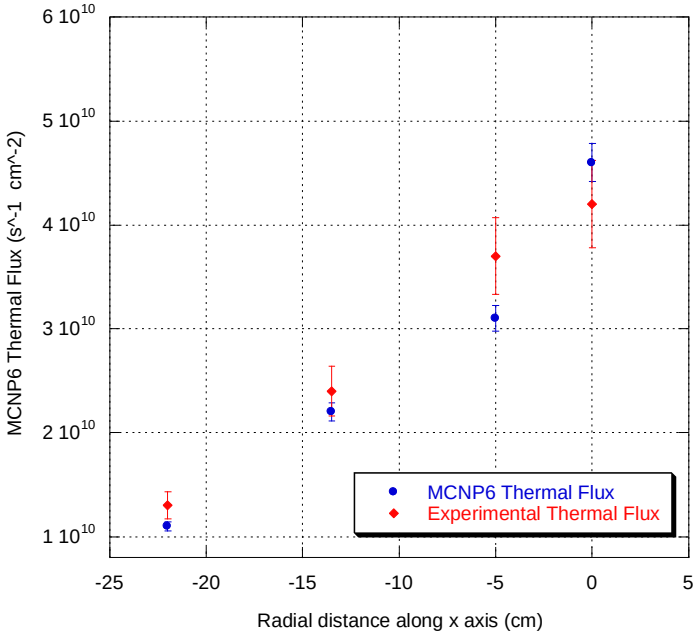

Figure 3. 10: RADIAL DIRECTION - Thermal neutron fluxes along the radial core direction (x axis) obtained by means of MCNP6 simulation and through measurement.

The uncertainty of the MCNP results for the total-flux values resulted to be in the range of 2-3%, except for position 1 and 11 where it raises to 5%. Higher uncertainty was obtained for the others flux component: typical thermal-flux

uncertainty resulted to be about 5% with maximum values around 9% in the vertical external positions (POS1 and POS11) and in the radial positions (Position *b, i ,o*).

3.3.2. Out of core calculation results: Horizontal Beam Tube and Lazy Susan

In order to benchmark the MCNP model effectiveness also in the out of core regions, the experimental results described in 2.3 at the Horizontal Beam Tube B and at the Lazy Susan irradiation facility were considered.

Horizontal Beam Tube B

In case of the Horizontal Beam Tube B, as said in 2.3, it was not known if the Beam Tube B faces the full graphite or an empty volume in correspondence of the graphite reflector.

For this reason, two MCNP6 simulations were performed, one for each case, in correspondence of the experimental Position 1 (see Table 2.9 for position definition); the other experimental positions (Position 2 and 3) were not simulated as they lay out of the boundary of the MCNP6 reactor model.

The obtained MCNP6 results were then compared with the experimental neutron flux spectrum, as shown in Figure 3.11.

It can be seen that, while the simulation with the full graphite reflector (green coloured) is far away from the experimental values, the MCNP6 calculation performed with the empty volume in the graphite reflector (red coloured) best estimates the experimental (blue coloured) energy neutron distribution.

The calculated MCNP thermal and total neutron flux values are reported in Table 3.3 and compared to the experimental ones.

Results hence indicate that, most likely, the Beam Tube B at TRIGA reactor of TU Wien faces an empty volume in the graphite reflector.

Position 1	**Total Flux** (cm-2 *s-1)	**Thermal flux (<0.69eV)** (cm-2 *s-1)
Experimental (see Table 2.13)	$(5.74\pm0.50)\cdot10^{11}$	$(3.28\pm0.30)\cdot10^{11}$
MCNP empty graphite	$4.30\cdot10^{11}$	$2.96\cdot10^{11}$
MCNP full graphite	$2.05\cdot10^{11}$	$1.67\cdot10^{11}$

Table 3. 3: MCNP6 results in Beam Tube B, Position 1 for the two different graphite reflector configurations (empty cavity or full graphite) and comparison with experimental values (reactor power 250 kW).

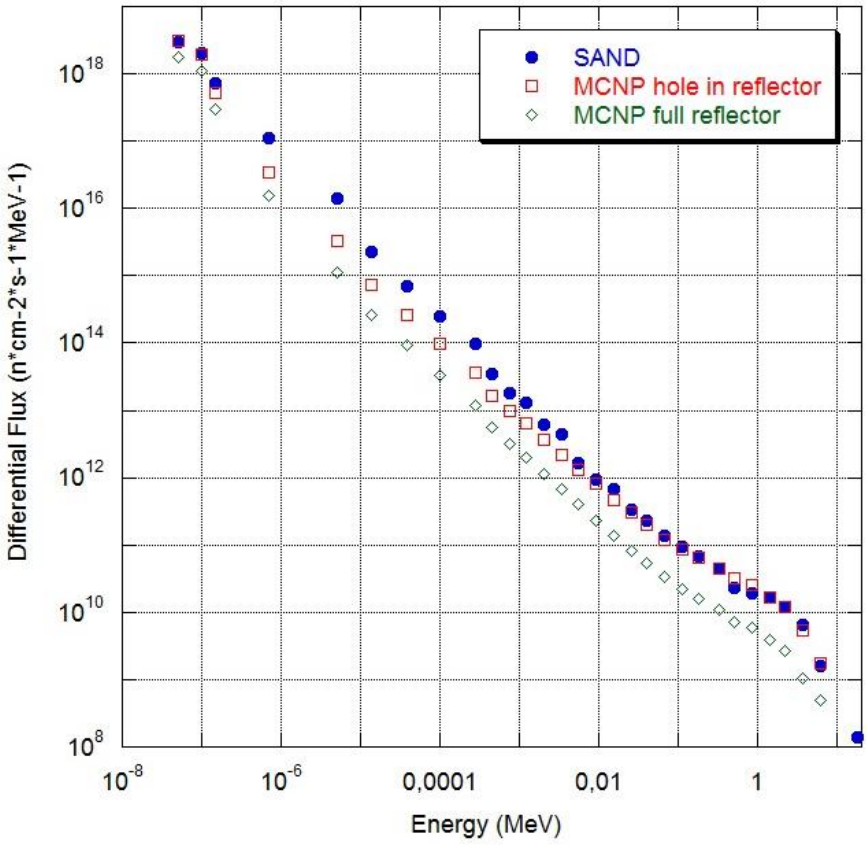

Figure 3. 11: Comparison of experimental (blue coloured) and MCNP6 (red and green coloured) results for the neutron spectrum in Position 1 of the Horizontal Beam Tube B.

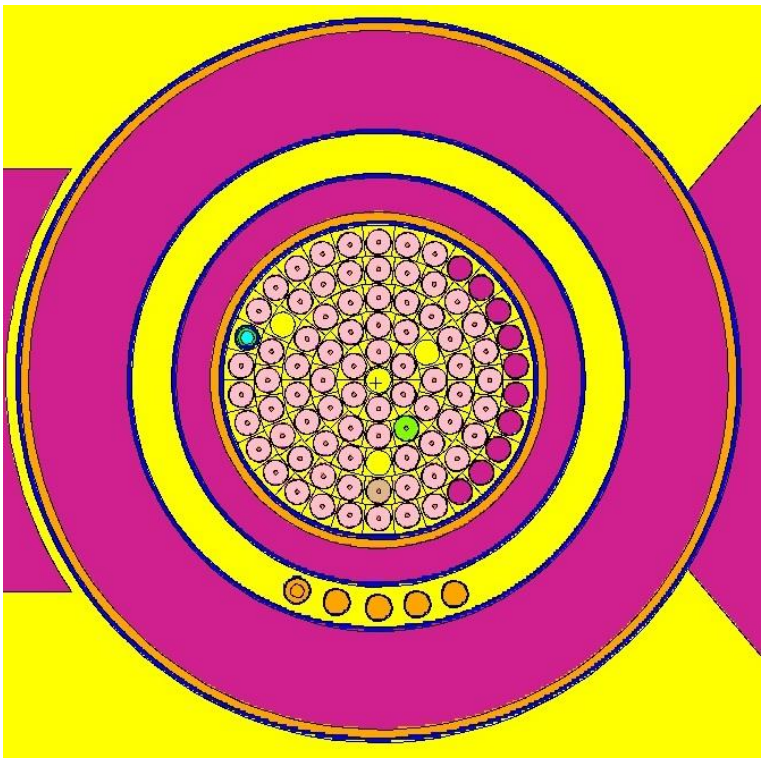

Figure 3. 12: Section of the reactor (z = 5cm) showing the Lazy Susan cavity and the current five vertical dry beam tubes available as irradiation positions LS1, LS2, LS3, LS4, LS5.

Lazy Susan

The second out of core position to be checked with the MCNP6 model was the Lazy Susan irradiation facility LS1. At the TRIGA reactor of TU Wien, the original Rotary Specimen rack was removed long time ago from the reflector and replaced with five vertical dry irradiation tubes (LS1, LS2, LS3, LS4, LS5). The aluminum irradiation tubes were implemented in the current MCNP6 model (Figure 3.12).

The irradiation position LS1 used for flux experimental characterization (see 2.3) is the first from left. The vertical view of the LS1 position is provided in Figure 3.13: at a lower level in the reflector, the Horizontal Beam Tubes C and D are also visible.

A cell, with dimension and location comparable to those of the irradiated samples, is placed in the LS1 dry tube and used as a Tally (F4) in the MCNP calculation. The MCNP simulation was run and obtained results are shown in Table 3.4.

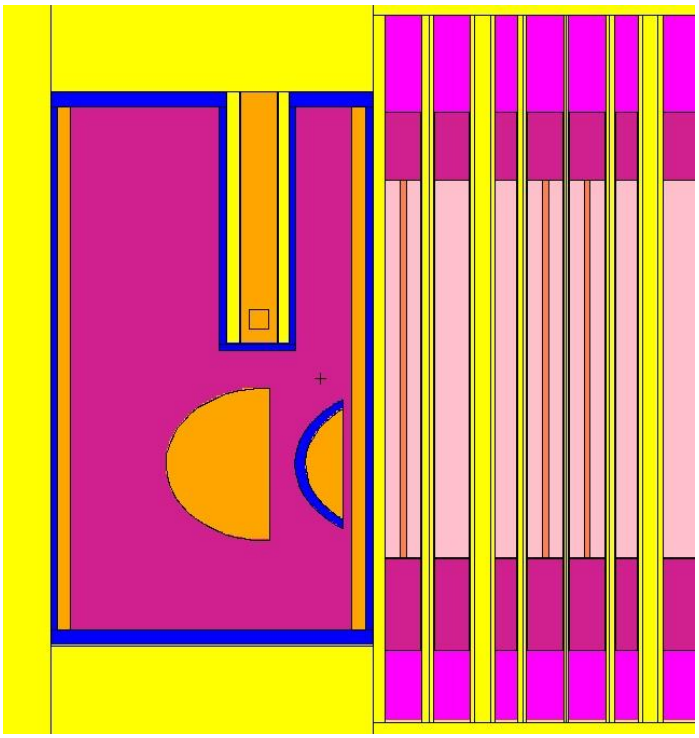

Figure 3. 13: Vertical view of the LS1 irradiation facility located in the graphite reflector.

Position LS1	**Total Flux** (cm-2 *s-1)	**Thermal flux (<0.69eV)** (cm-2 *s-1)	**Epithermal Flux (0.69eV-110keV)** (cm-2 *s-1)	**Fast Flux (110keV-18MeV)** (cm-2 *s-1)
Experimental (see Table 2.14)	$(3.69\pm0.31)\cdot10^{12}$	$(2.05\pm0.17)\cdot10^{12}$	$(5.59\pm0.50)\cdot10^{11}$	$(1.08\pm0.13)\cdot10^{12}$
MCNP	$2.46\cdot10^{12}$	$1.85\cdot10^{12}$	$3.54\cdot10^{11}$	$2.51\cdot10^{11}$

Table 3. 4: MCNP6 results in position LS1 and comparison with experimental values.

3.4. Results evaluation for MCNP6 model validation

Considering the 14 in-core irradiation positions used for the verification of the developed MCNP6 reactor model, the results of the simulation and of the measurement show a good agreement within the experimental uncertainties (<9%). This can be seen both comparing calculated with experimental neutron energy spectra (e.g. Figure 3.6); as well as comparing specific neutron spectrum components (see Figures 3.7, 3.8, 3.9, 3.10).

As verified for the experimental values, the distribution of (total and thermal) MCNP calculated fluxes along the vertical direction of the core (Figures 3.7, 3.8) shows a typical cosine behaviour. MCNP6 systematically overestimates the value of the thermal flux over the axial distribution: this could be explained by the fact that in the simulation the material are without impurities that may affect the absorption of neutrons, especially in the thermal region. However the same behaviour is not reflected in the radial distribution of the thermal flux.

Among the out of core positions, the MCNP calculation in the Horizontal Beam Tube B and subsequent comparison with experimental values allowed to identify the tube configuration (full graphite) in correspondence of the reactor reflector. MCNP results are lower than the experimental ones (e.g. 9.7% less for thermal flux component), but they can still considered acceptable as the position is far away from the reactor core and outside of the graphite reflector region.

Also for the Lazy Susan LS1 position, MCNP calculated values underestimate (Table 3.4) the experimental ones, but of only 10% in the thermal region. This results is considered valuable for the proper characterization of the LS1 irradiation position: in fact, experiments performed lately (Chapter 4) in this position, aimed to fission products production in fissile materials, are then mainly affected by the thermal spectrum component.

Based on the above considerations, the new reactor model developed in MCNP6 was tested and benchmarked against experimental results (flux values and neutron energy spectra) in several irradiation positions, both in core and out of core.

In such a way, the MCNP6 model was validated and can be used from here on to calculate neutron flux and spectrum in other reactor region where a direct measurement is not possible, like for example inside the fuel elements (see Chapter 5).

Chapter 4

Experimental determination of transmutation rates

The present chapter describes experiments conducted at the TRIGA Mark II reactor of TU Wien, within the framework of the present PhD work, in order to estimate the transmutation rates of nuclides relevant for the study and analysis of nuclear fuel composition under irradiation, focusing on major and minor actinides build-up and burn-up and on fission product production and depletion.

The first experiment (§4.1) is related to the irradiation of target foils containing the above mentioned nuclides in one of the characterized (see Chapter 2) irradiation facility at the TRIGA reactor. Following irradiation, the samples were measured by means of gamma-ray spectrometry technique in order to determine the transmutation rates (production and depletion) inducted by neutrons.

The second experiment (§4.2) consisted in the detection of fission products activity distribution along the axial dimension of irradiated fuel elements (FEs) at the TRIGA reactor. The activity distribution was measured by means of a proper fuel gamma scanning device and different fission products were detected. For the deduction of reliable activity values, the MCNP6 code was utilized for self-absorption and geometric effects as explained in detail in §4.2.2 and §4.2.4.

Both experiments provided a data set of experimental results reported in the present Chapter: these data have been subsequently used for the validation of the new TRIGA reactor model developed using the Serpent code (see Chapter 5).

4.1 Transmutation rate determination in irradiated Uranium and Thorium foils

This activity was planned in order to obtain experimental data about production and depletion of nuclides in natural Uranium (U) and Thorium (Th) samples following an irradiation at the TRIGA MARK II reactor of the Atominstitut. The obtained data have subsequently been used (see 5.2) to verify the capability of Serpent reactor model to predict changes in the composition of nuclear fuel under irradiation. Three samples of each kind (U, Th) were irradiated under consistent conditions in the Lazy Susan (see 1.5.6) irradiation position. All samples were counted and analysed both before and after irradiation and the results compared. In this chapter, results in terms of the activities of the detected nuclides are reported.

4.1.1 U and Th samples

As stated above, one of the objectives of the present work was to establish a methodology for verification of theoretical calculation models used in the study of nuclear fuel composition under irradiation. To develop a scheme valid for a wide variety of reactors (i.e. operated on both the Uranium and the Thorium cycle) the natural Uranium and Thorium material foils were selected for irradiation.

The natural Uranium composition presents 99.27% of U-238, 0.72% of U-235 and 0.0055% of U-234. In nuclear fuel, the percentage of U-235 varies basing on the enrichment, ranging from the natural abundance up to 90%.

Natural Thorium (100% of Th-232) instead is not fissile but it is a fertile nuclide: in nuclear reactors it undergoes nuclear transmutation giving as a product the fissile nuclide U-233.

The samples used for this irradiation at the TRIGA reactor were obtained by "Goodfellow Cambrige Limited" and were provided with appropriate certificate for the mass, dimensions and composition. In addition to the natural isotope composition of the Thorium and Uranium samples, some impurities are present in very low (ppm) concentrations but have no influence in the analysis.

The samples were thin plates/foils with diameter of 10.0±0.5mm. The Uranium foils present an average thickness of 0.178±mm10%, while the Thorium foils of 0.125mm±10%.

(a) Uranium foil compared with cent coin

(b) Thorium foil compared with cent coin

(c) Irradiation Capsule, Plastic Container, Small Capsule

Figure 4.1: Picture of Uranium (a), Thorium (b) foils and irradiation capsules (c).

The samples were weighed at the laboratory by means of a calibrated scale (SATORIUS GmbH GÖTTINGEN type R160P-*A1) and results compared with the data from *GoodFellow* certificates (see Table 4.1). From this point on the samples were assigned a code (U1, U2, U3 and TH1, TH2, TH3) used throughout irradiations and analysis process. U and Th samples in comparison to a cent coin are shown in Figure 4.1(a) and 4.1(b) together with the irradiation capsules utilized for the irradiation.

In addition, one standard 99.99% pure Copper foil (0.5 mm thick and 6mm in diameter) was irradiated as flux monitors during each irradiation to verify the consistency between the different irradiations as it will be shown later. For irradiations the foils were placed into a small capsule which is then inserted into the irradiation capsule (Figure 4.1.c).

Datasheet Code	Sample Code	Datasheet Mass [g]	Measured Mass [g]
U00210/15-1	U1	0.212	0.21212
U00210/15-2	U2	0.216	0.21605
U00210/15-3	U3	0.210	0.20843
TH000220/4-1	TH1	0.129	0.12867
TH000220/4-1	TH2	0.124	0.12610
TH000220/4-1	TH3	0.126	0.12647

Table 4. 1: Comparison of Uranium and Thorium masses.

Figure 4.2: U-235 decay chain.

4.1.2 Irradiation setting and measurement procedure

Pre-irradiation foils measurement

Before irradiation, the foils were counted by low background gamma spectrometry to verify the content of U-238 and U-235 in U foils, of Th-232 and Ra-228 in Th foils.

For each natural U foil, the activity of U-235 was measured at the gamma energies of 143.8 keV, 163.4 keV, 185.7 keV e 205.3 keV; the activity of U-238 was derived from the 1001 keV gamma energy of Pa-234m in equilibrium with U-238 (Figure 4.3). As the Uranium foils are considered thick foils, their activity values were corrected for self-absorption effect by means of appropriate MCNP simulation. The ratio U-238/U-235 equal to 21.5 in natural Uranium was also verified though this activity measurement (Table 4.2).

In the case of Th foils, the activity was measured for Ra-228 (Ac-228 gamma lines at 911 e 969 keV) and Th-228 (Pb-212 gamma line at 238.6 keV) in equilibrium with Th-232 (Figure 4.4). Results are reported in Table 4.2.

Figure 4.3: U-238 decay chain.

Irradiation setting

Six irradiations were performed at the TRIGA reactor, one for each U/Th foil. The irradiation position was kept the same in every case and corresponded to one of the dry beam tubes of the Lazy Suzan (LS1) irradiation channel. This irradiation position was part of the neutron flux characterization described in Chapter 2. In each irradiation, the irradiation time was set at 90 minutes, whit reactor power of 5 kW.

During each irradiation in LS1, a copper foil was irradiated in parallel in the Central Thimble (CT) as a flux monitor: this position was chosen both to not interfere with U/Th irradiation and as this in core position is well characterized and reproducible (see Chapter 2.1).

Following the irradiation, due to high activity dose rate, the samples needed to remain in the reactor at least over night for a sufficient cooling down.

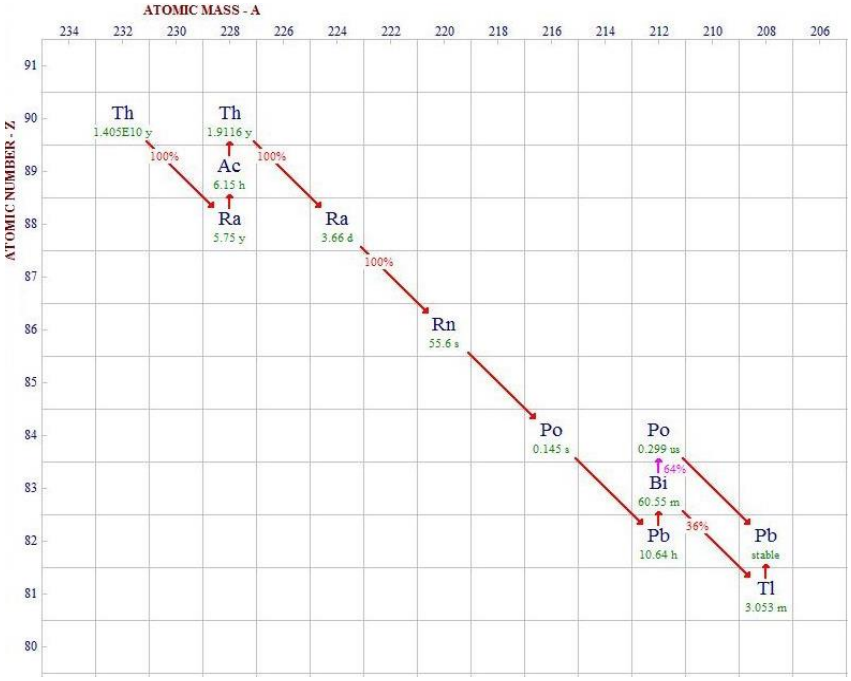

Figure 4.4: Th-232 decay chain.

Sample Code	U235 PREIRR Measured Activity [Bq]	U238 PREIRR Measured Activity [Bq]	Measured U238/U235 Ratio
U1	125.19	2696.44	21.54
U2	129.62	2779.59	21.44
U3	125.16	2695.10	21.53

	Ra-228 PREIRR Measured Activity [Bq]	Th228 PREIRR Measured Activity [Bq]
TH1	527.14	501.55
TH2	505.26	503.09
TH3	515.15	505.41

Table 4. 2: Results of pre-irradiation measurement of U and Th foils by low background gamma spectrometry.

4.1.3 Irradiated sample activity determination by gamma spectrometry

Irradiated foils activity was measured by means of a coaxial closed-ended HPGe n-type GAMMA-X (series C5020, CANBERRA) with 52.8% relative efficiency, 1.81 keV energy resolution at 1.33 MeV and Peak/Compton edge ratio equal to 73.6. The efficiency calibration of the detector was performed by means of a certified solid multi gamma calibration source (Type QCRB1186,

Eckert&Ziegler) with dimension and geometry similar to those of the activated foils. The acquired spectra were analyzed using the GENIE2K[21] Analysis software provided from CANBERRA.

Multiple measurements were performed after irradiation to verify the best conditions for samples counting. As for the cooling down time before counting, the Cu foils where typically measured 2-3 days after irradiation, while a longer cooling time was required for both U and Th irradiated foils. In addition, as produced fission products present different half-lives, it was decided to repeat each foil counting at different elapsed times after end of irradiation to better determine fission product activities. The counting time (real time) ranged from about 5000s (measurement 10 days after irradiation) up to 80000s (measurement 30 and 90 days after irradiation) and was corrected for the dead time of the detector when of interest. Parameters of the different gamma spectroscopy measurement are reported in Table 4.3.

The best counting position (i.e. distance between sample and detector) was selected over 3 possible calibrated positions (S=180 mm, M=250 mm, L=400 mm) finding a balance between low dead time and good counting statistics. The dead time was always kept under 10% for acceptable measurement outcomes.

4.1.4 Data analysis and results

The composition of the irradiated foils and the processes occurring during and after irradiation (neutron activation, decay, fission, etc.) were evaluated in advance to obtain an overview of the nuclides to look after and check for in the gamma spectra. Peak interferences and mother-daughter pairs were also checked and corrected.

Copper Sample Analysis

The irradiation of Copper (Cu) foils (see §4.1.2) in the CT position in correspondence of each U/Th foil irradiation was used to check the comparability of the different irradiations, i.e. that all U/Th foils in the LS channel underwent the same neutron fluence even if several irradiations were performed.

Irradiation ID	Foil ID	Counting position	Real Time [s]	Time since Irr. [d]	Dead Time (DT)
1LSU1	CU1	M	83996.86	3	not irradiated
	U1	M	4581.12	11	DT: 8,22%
	U1	S	80000.00	28	DT: 6%
	U1	S	80000.00	108	DT: 6%
2LSTH1	CU2	S	3345.30	6	DT: 2,47%;
	TH1	M	50000.00	8	DT: 7,86%
	TH1	S	80000.00	28	DT: 5%
3LSU2	CU3	M	3577.01	4	DT: 7,67%
	U2	M	4561.82	11	DT: 9,11%
	U2	S	80000.00	27	DT: 6%
	U2	S	80000.00	96	DT: 2%
4LSTH2	CU4	M	4579.94	4	DT: 8,07%
	TH2	M	5712.25	7	DT: 7,9%
	TH2	S	80000.00	36	DT: 4%
5LSU3	CU5	M	4946.34	4	DT: 7,68%
	U3	M	5002.30	11	DT: 9%
	U3	S	80000.00	34	DT: 5%
	U3	S	80000.00	95	DT: 2%
6LSTH3	CU6	M	5017.30	4	DT: 8,75%
	TH3	M	5000.51	8	DT: 8%
	TH3	M	80000.00	32	DT: 4%

Table 4.3: Parameters of the different gamma spectroscopy measurements performed on irradiated U and Th foils.

The irradiated Cu foils were analysed to detect the induced reaction $^{63}Cu\ (n,\gamma)\ ^{64}Cu$ and the correspondent Cu-64 (12.7h half-life) gamma emission at 1345.77keV (0.4748 %). The detected activity values A_{EndIrr}, calculated back to the end of the irradiation time (i.e. reactor shut-down) are shown in Table 4.4. The corresponding specific activity saturation values (A_{sat}), i.e. maximum achievable activity per atom under fixed irradiation parameters (see 2.1.1), was obtained as:

$$A_{sat} = A_{EndIrr} / (N_{atoms} * (1-EXP(-\lambda * t_{irr}))$$

where N_{atoms} is the number of Cu-63 atoms in the target foil and t_{irr} the irradiation time.

Irradiation ID	Foil ID	FOIL WEIGHT [mg]	A_{EndIrr} [Bq]	A_{sat} [Bq]	C_{fact} (%)
2LSTH1	CU2	122.71	(4.83±0.40) $x10^{7}$	(7.64±0.64) $x10^{-13}$	1.2
3LSU2	CU3	123.06	(4.88±0.33) $x10^{7}$	(7.69±0.53) $x10^{-13}$	-
4LSTH2	CU4	122.54	(4.70±0.39) $x10^{7}$	(7.44±0.61) $x10^{-13}$	3.8
5LSU3	CU5	122.84	(4.69±0.39) $x10^{7}$	(7.41±0.61) $x10^{-13}$	3.6
6LSTH3	CU6	123.34	(4.91±0.41) $x10^{7}$	(7.73±0.64) $x10^{-13}$	-

Table 4. 4: Cu-64 detected activity values after each irradiation in the Central Thimble.

The results of the five Cu samples show that the irradiations were comparable being around 4% the biggest relative error between irradiation 5LSU3 and 6LSTH3. Nevertheless, correction factors were determined and applied in order to normalize both the U and Th activity results respectively: their values are shown in Table 4.4. The CU1 sample in the first irradiation (1LSU1) resulted not irradiated: in this case, the U foil activity values where not normalized.

Uranium Sample Analysis

As first step, the long term gamma measurements (about 3 months after end of irradiation) were used for the comparison with the pre-irradiation U activity values. The results for the U samples are displayed in Table 4.5. As expected the activity of U-238 as well as U-235 inside the uncertainty limits is unchanged before and after irradiation.

For U-238 in the natural U foils, the dominant reaction when irradiated with thermal neutrons is neutron capture. The decay chain following neutron activation of U-238 is shown in Figure 4.5.

Considering the half-life of U-239, the only nuclide detectable after the decay time necessary for suitable measurement conditions, regarding the activation is Np-239. The produced Pu-239 with half-life of $2.4x10^{4}$ years was not detected due small amount production and its long half-life: it is therefore also considered negligible for fission products production in comparison to U-235 fission contribution.

About U-235, when irradiated with thermal neutrons, a wide variety of fission products is produced.

Sample Code	Nuclide	Activity Pre-irradiation [Bq]	Activity Post-irradiation [Bq]
U1	**U235**	125.19	123.44
	U238	2696.44	2642.35
U2	**U235**	129.62	126.15
	U238	2779.59	2790.82
U3	**U235**	125.16	120.47
	U238	2695.10	2689.80

Table 4. 5: Comparison of U foils activity values measured before and after irradiation.

The plot of the fission yields over the mass number of the fission product is shown in Figure 4.6, where the two most populated regions are in the range of 90<A<100 and 135<A<145 respectively. The cumulative fission yield (CFY), indicating the percentage of a specific nuclide produced during the fission process, is given in % per fission and sums up to 100% including both fission products.

For determination of the fission fragments produced with the highest probability during the natural U foil irradiation, the fission products with CFY>2.5% per fission of U-235 (Table 4.6) were selected for consideration according to the CFY values reported in literature[22]. Some of those nuclides (e.g. Ce-144, Sr-90) present an half-life too long for decent activity results in short spectroscopy measurements; others (e.g. I-135, Xe-135, Pr-144 and Nd-144) have instead a too short half-life for being still present at the time of measurement. In both cases then, those nuclides could not be detected.

$$^{238}U(n,\gamma)^{239}U \xrightarrow[23.47min]{\beta^-} {}^{239}Np \xrightarrow[2.355d]{\beta^-} {}^{239}Pu$$

$$^{238}U \xrightarrow[4.5E9y]{\alpha} {}^{234}Th \xrightarrow[24.1d]{\beta^-} {}^{234m}Pa \xrightarrow[1.17min]{\beta^-} {}^{234}U \xrightarrow[245.5E3y]{\alpha} {}^{230}Th...$$

$$^{235}U \xrightarrow[7.04E8]{\alpha} {}^{231}Th \xrightarrow[25.52h]{\beta^-} {}^{231}Pa \xrightarrow[3.276E4y]{\alpha} {}^{227}Ac...$$

Figure 4. 5: U-238 dacay chain and activation by neutron capture reaction.

.

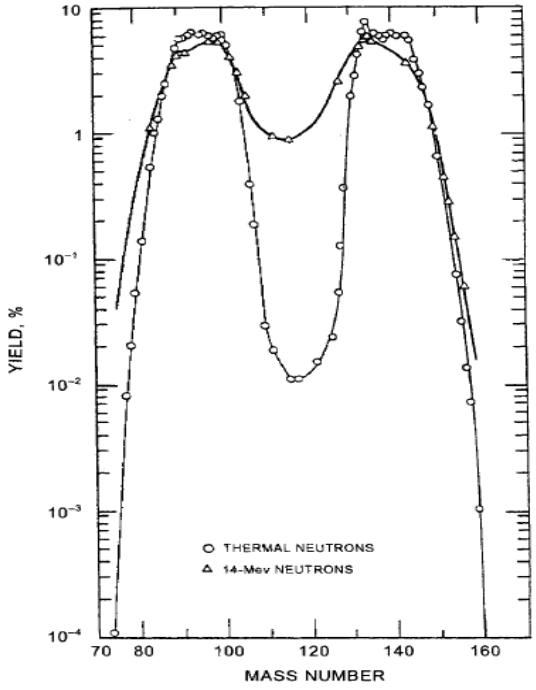

Figure 4. 6: Fission products distribution for U-235 fission[2]

For the analysis of irradiated Uranium samples, another factor need to be considered. In fact, for produced nuclides that are in a parent-daughter relation (e.g. Te-132/I-132, Zr-95/Nb-95 and Ba-140/La-140) the activity of the daughter nuclide (*d*) is correlated with the decay of the parent nuclide (*p*); that is, simple application of the decay law is not sufficient to derive the activity at the end of irradiation time for the daughter nuclide. In this case, the equation describing the behavior of the daughter nuclide population is:

$$\frac{dN_d}{dt} = \lambda_p N_p(t) - \lambda_d N_d(t) \qquad (4.27)$$

where N_p and N_d are the number of parent and daughter atoms at time t, and λ_p and λ_d the parent and daughter decay constant respectively.

The general solution of the equation (4.1), in terms of the daughter activity ($A_d(t)$) as a function of time, can be written[23] as:

$$A_d(t) = \frac{\lambda_d}{\lambda_d - \lambda_p} A_p(0)\left(e^{-\lambda_p t} - e^{-\lambda_d t}\right) + A_d(0)e^{-\lambda_d t} \qquad (4.2)$$

being $A_p(0)$ and $A_d(0)$ the parent and daughter activity values at time t=0.

Element	CFY [% per f]	Half Life		Element	CFY [% per f]	Half Life
Zr-95	6.502 ± 0.072	64.02d		Sr-90	5.73 0.13	28.81a
Nb-95	6.498 0.072	34.99d		Ru-103	3.103 0.084	39.27d
Mo-99	6.132 0.092	2.748d		Te-132	4.276 0.043	3.20d
(Tc-99m)	-	(6.01h)		I-131	2.878 0.032	8.02d
I-133	6.59 0.11	20.8h		I-135	6.39 0.22	6.57h
Xe-133	6.6 0.11	5.24d		Xe-135	6.61 0.22	9.14h
Cs-137	6.221 0.069	30.06a		Ba-140	6.314 0.095	12.77d
La-140	6.315 0.095	1.68d		Pr-144	5.474 0.055	17.28min
Ce-141	5.86 0.15	32.50d		Nd-144	5.475 0.055	-
Ce-144	5.474 0.055	285d		Nd-147	2.232 0.04	10.98d

Table 4. 6: List of the U-235 fission products that where taken into account for the analysis, their Cumulative Fission Yield (CFY) and half-lives. (Tc-99m was expected as a product of Mo-99 decay).

The daughter activity at end of irradiation ($A_d(0)$) can then be deducted once are known $A_p(0)$ (derived by measured $A_p(t)$) and $A_d(t)$ (measured). Considering the half-lives of the parent/daughter couples like Mo-99(66h)/Tc-99m(6h), Ba-140 (12.8d)/La-140(1.68d) it happens that they decay towards transient equilibrium ($T_{1/2d} < T_{1/2p}$). This means that at long times (around 3 to 5 daughter half-lives) the ratio of daughter to parent activity becomes constant ($A_d(t)/A_p(t) = \frac{\lambda_d}{\lambda_d - \lambda_p}$) and both decay curves will propagate in parallel (Figure 4.7).

In conclusion, nearly all fission products predicted above were detected by means of gamma spectroscopy and the activation measurement results for the three Uranium foils are shown in Table 4.7. Data are reported for each detected nuclide in the gamma measurement performed after around 11 days from end of irradiation; in addition, some nuclides activities have been checked and reported also after about 100 days from end of irradiation.

The results are reported as obtained at the time of the measurement. The activity values at time of end of irradiation can be deducted by direct application of the decay law. When parent-daughter fission products are detected the application of equation 4.2. is required to deduce the daughter nuclide activity at end of irradiation time. Considering the performed gamma spectroscopy measurement available, it can be noted that:

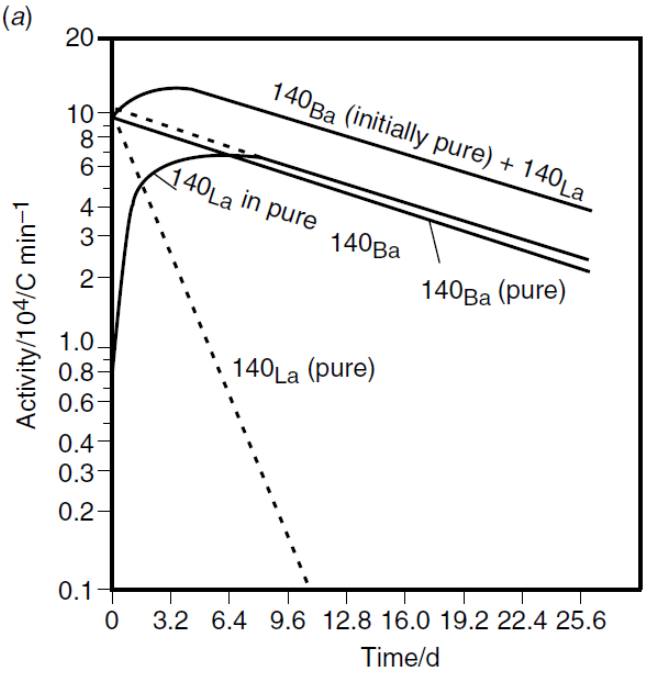

Figure 4. 7: Transient equilibrium for the parent-daughter couple Ba140-La140. [23]

- The experimental activity results for all three U samples are comparable and show a very good agreement for each detected nuclide.
- Ba-140/La-140 parent-daughter couple has already reached the transient equilibrium at time of first gamma spectroscopy (11 days after irradiation). Then, equation 4.2 can be applied and the equilibrium condition can be verified as the activity ratios $A_{La}(t)/A_{Ba}(t)$ results equal to the predictable value $\frac{\lambda_d}{\lambda_d-\lambda_p} = 1.15$.
- In the Mo-99/Tc-99m couple, only the Mo-99 is relevant as fission product.
- Zr-95/Nb-95 trend in the different measurement show that the two nuclides are reaching the equilibrium even though not yet completed at the time of last gamma spectroscopy (about 100 days after irradiation). As the equations 4.2 gives back correct results when parent and daughter nuclide have already reached transient equilibrium, this will be taken in consideration when comparing calculation and experimental results.
- Np-239 activity was deducted from the 277.599keV (14.4 %) gamma line only, as the other line at 228.327keV (11.32 %) presents interference with Te-132.

Analyzed Element	Peak [keV]	Measured Activity U1 [Bq]	Measured Activity U2 [Bq]	Measured Activity U3 [Bq]	Normalized (*) Activity (Bq)		
					U1	U2	U3
		Measurement: 11 days after irradiation					
Ba-140	537.303	6.97E+03	6.99E+03	6.94E+03	6.97E+03	6.86E+03	7.01E+03
La-140	487.022	7.99E+03	8.00E+03	7.90E+03	7.99E+03	7.85E+03	7.98E+03
Mo-99 c	739.5	3.41E+03	3.90E+03	3.65E+03	3.41E+03	3.67E+03	3.69E+03
Tc-99M	140.511	2.54E+03	2.81E+03	2.69E+03	2.50E+03	2.65E+03	2.72E+03
Np-239	277.599	5.51E+04	6.07E+04	5.74E+04	5.51E+04	5.95E+04	5.79E+04
Ce-141 c	145.4433	2.65E+03	2.69E+03	2.74E+03	2.65E+03	2.64E+03	2.77E+03
Nd-147	531.06	2.61E+03	2.89E+03	2.83E+03	2.61E+03	2.84E+03	2.86E+03
Te-132 c	228.327	7.59E+03	9.38E+03	9.30E+03	7.59E+03	9.21E+03	9.39E+03
I-132	522.65	3.69E+03	4.11E+03	3.99E+03	3.69E+03	4.03E+03	4.03E+03
I-131	364.489	3.77E+03	3.85E+03	3.81E+03	3.77E+03	3.78E+03	3.85E+03
Xe-133	80.9979	6.28E+03	6.45E+03	6.49E+03	6.28E+03	6.33E+03	6.55E+03
Ce-143	293.266	4.20E+02	4.80E+02	4.45E+02	4.20E+02	4.71E+02	4.49E+02
Ru-103	497.08	1.74E+03	1.73E+03	1.72E+03	1.74E+03	1.70E+03	1.74E+03
Zr-95 c	756.729	2.44E+03	2.42E+03	2.45E+03	2.44E+03	2.37E+03	2.47E+03
Nb-95	765.803	4.97E+02	4.69E+02	4.85E+02	4.97E+02	4.61E+02	4.90E+02
		Measurement: 100 days after irradiation					
Zr-95 c	756.729	7.98 E+02	9.00E+02	9.06E+02	7.98E+02	8.83E+02	9.15E+02
Nb-95	765.803	1.12 E+03	1.17E+03	1.18E+03	1.12E+03	1.15E+03	1.19E+03
Cs-137	661.00	1.40E+01	1.41E+01	1.41E+01	1.40E+01	1.38E+01	1.42E+01

Table 4.7: Activation results for U foils (U1,U2,U3). The values are already normalized on the Cu-monitor results and are related to the indicated time of measurement. The uncertainty of the measurement are within 10%. (*) The measured activity values are normalized on the mass of U1 foil for direct comparison.

- For the parent-daughter couple Te-132/I-132, it has to be noted that Te-132, lacks of an alternative significant peak except the one at 228.327keV (not usable because of interference, see above). Then the activity of Te-132 was not determined. The activity of I-132 was determined and shows consistent values among the different samples; nevertheless, due to the unknown parent (Te-132) activity, equation 4.2 is not applicable, i.e. I-132 activity at end of irradiation cannot be deduced.

Th-232 Sample Analysis

For the irradiated Thorium foils, among the spectroscopy measurement performed (see Table 4.3) the ones at about 27 days elapsed time after irradiation resulted as the more appropriate for the analysis.

As done for U foils, a comparison with the pre-irradiation Thorium activity values was carried out. The results for the Thorium samples are displayed in Table 4.8: again, within the uncertainty limits, the activity values do not show a modification of Thorium content in the sample following the irradiation.

The Thorium samples present a natural abundance of 100 % Th-232. During the irradiation, Th-233 is produced by capture reaction of thermal neutrons. Th-233 then decays according to the decay chain shown in Figure 4.8, with production of fissile U-233. Due to the short half-life of Th-233, Pa-233 was the only detectable nuclide from this activation decay chain: activity values of Pa-233, normalized basing on the Copper foils monitor results (see Table 4.4), are reported in Table 4.8.

Among the fission products, only Ba-140 and La-140 were detected (Table 4.8). The explanation could be that, even if the irradiation induced a detectable transmutation of Th-232 into U-233, the fission reaction of U-233 occurred only in limited amount: as a result, the fission products Ba-140 and La-140 were hardly detectable with the used instrumentation.

$$^{232}Th(n,\gamma)^{233}Th \xrightarrow[22.15min]{\beta^-} {}^{233}Pa \xrightarrow[26.98d]{\beta^-} {}^{233}U$$

$$^{232}Th \xrightarrow[1.41E10]{\alpha} {}^{228}Ra \xrightarrow[5.7y]{\beta^-} {}^{228}Ac \xrightarrow[6.1min]{\beta^-} {}^{228}Th \xrightarrow[1.9y]{\alpha} {}^{224}Ra$$

$$^{224}Ra \xrightarrow[3.6d]{\alpha} {}^{220}Rn \xrightarrow[55s]{\alpha} {}^{216}Po \xrightarrow[0.14s]{\alpha} {}^{212}Pb \xrightarrow[10.6h]{\alpha} {}^{212}Bi$$

Figure 4.8: The capture reaction on Th-232 with its decay chain (up to U-233 production) and the natural Th-232 decay chain are shown.

Sample Code	Nuclide	Pre-irradiation Activity [Bq]	Post-irradiation Activity [Bq]
TH1	Ra228 (Ac228)	527.14	533.31
	Th228 (Pb212)	501.55	481.55
	Pa233	-	1.13E+05
	Ba140	-	20.08
	La140	-	22.57
TH2	Ra228 (Ac228)	505.26	515.79
	Th228 (Pb212)	503.09	466.12
	Pa233	-	1.11E+05
	Ba140	-	20.90
	La140	-	24.06
TH3	Ra228 (Ac228)	515.15	523.74
	Th228 (Pb212)	505.41	485.00
	Pa233	-	1.12E+05
	Ba140	-	19.70
	La140	-	21.94

Table 4.8: Comparison of detected activity pre- and post-irradiation (activity post-irradiation were deducted from gamma spectroscopy performed after 27days for Ra228 and Th228; after 7 days for the remaining nuclides). The uncertainty of the measurement resulted within 10%.

4.2 Fission product detection in irradiated Fuel Elements

Aim of this activity was the detection of fission products activity distribution along the axial dimension of irradiated fuel elements (FEs) at the TRIGA Mark II research reactor of the TU Wien.[34, 35, 36]

The activity distribution was measured by means of a proper fuel gamma scanning device, which includes a vertical lifting system to move the fuel rod along its vertical axis. For each investigated FE, a gamma spectrum was recorded every 1 cm along the fuel rod axis resulting in the vertical distribution of the fission products. After the fuel elements underwent a relatively short cooling down period, different fission products were detected. The activity concentration was determined by calibrating with a standard calibration source of known activity and by MCNP6 Gamma-scanning device simulation for the evaluation of self-absorption and geometric effects.

Based on the specific TRIGA fuel composition, a correction procedure was developed for the particular case of detected fission product Zr-95. This chapter shows how the activity

contributions coming from neutron capture of Zr-94 was evaluated by means of MCNP6 simulation and deducted from the measured Zr-95 activity value.
This measurement campaign provided experimental results to be subsequently used for the validation of the reactor calculation models.

4.2.1 Fuel elements activity measurement

The present measurement campaign was conducted in occasion of a planned reactor shut-down period: this allowed to investigate the irradiated fuel elements after a cooling down period of 251 days.
The selection of FEs to be measured by gamma scanning was such that the FEs position in the core was constant during their irradiation history (see Table 4.9): this choice will facilitate the process of benchmarking and validation of Monte Carlo models in the future.
The selected FEs were located in ring B (B2, B4), ring C (C1), ring D (D1) and ring E (E1). They underwent irradiation for 2191 hours (at 250 kW thermal power) over a period of 800 days at the TRIGA reactor in Vienna. After the measurement, they returned in the previous core positions.

The FEs gamma spectrometry was carried out by means of a fuel-scanning machine (FSM)[24,25] specifically developed for optical and spectrometry inspection of spent fuel at the TRIGA reactor in Vienna. As shown in Figure 4.9, the FSM consists of a shielded lead and stainless steel construction plus an electronic unit. Several radial openings in the shield allow inspection of a FE placed into the FSM. The upper part of the shield is a fuel lead transfer cask: this makes it possible to transfer one fuel element from the reactor tank to the FSM using the crane in the reactor hall. When a FE is placed in the FSM, it lays on the piston of the elevator system: through the control system, the FEs is moved along its vertical axis, adjusting the scanning speed and movement steps (steps can be done every millimetre). The axial position of the FE to be scanned is indicated by a digital monitor fixed on the fuel inspection unit.

In the radial opening used for the present FEs measurement, a collimator was placed: the collimator faced the fuel element with an area of 1 cm in diameter. On the opposite side of the radial opening a p-type coaxial High Purity Germanium

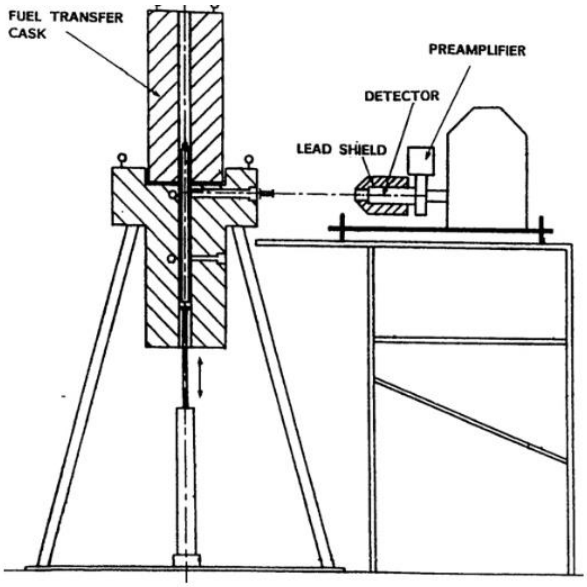

Figure 4. 9: Sketch[28] of the Fuel Scanning Machine (FSM) used for FEs activity experimental determination.

(HP-Ge) detector (aluminium window, 41mm x 41mm, 15mm x 10mm), shielded by a conical lead structure, was located for gamma spectrometry inspection. The acquisition system included a digital Multi Channel Analyser (model MCA-527 GBS Elektronik)[26]) and the WinSpec[27] data collection and analysis software.

The measurement was performed in the reactor hall, during a reactor shut-down period, i.e. no back ground radiation from the reactor interfered with the measurement. In this experiment, the fuel rods were measured in steps of 1 cm along their axial length: 38 acquired gamma spectra per element were obtained to cover the fuel active part. Due to the short cooling down period and to minimize the statistical and counting errors, the detection time was set to 45s. The distance between the fuel centre and the detector resulted in about 83cm in order to keep the dead time appropriate.

Fuel element		First irradiation day	Last irradiation day	Total hours at 250 kW	Date of measurement
In core position	ID				
B2	9213	21/01/1013	25/03/2015	2191	01/12/2015
B4	9214	21/01/1013	25/03/2015	2191	02/12/2015
C1	9905	21/01/1013	25/03/2015	2191	03/12/2015
D1	9915	21/01/1013	25/03/2015	2191	03/12/2015
E1	9932	21/01/1013	25/03/2015	2191	03/12/2015

Table 4.9: Irradiation history of the FEs investigated by gamma spectroscopy.

4.2.2 Calibration and simulation of the Fuel Scanning Machine

In order to determine the activity values of the detected isotopes, the Fuel Scanning Machine (FSM) needs to be properly calibrated in energy and efficiency, including geometry and self-absorption effects.

A certified Eckert&Ziegler Eu-152 gamma source was used for energy and efficiency calibration. It consisted of a capsule type (12mm diameter x 75mm length) source dispersed in epoxy matrix, with an active volume of 0.75 mL. Considering the geometry of the measurement system and the distance between the source and the detector, the used source can be considered as a point source. The obtained efficiency calibration curve allowed to set the efficiency value (ε) for each desired gamma energy.

Under ideal conditions, the measured sample and the calibration source should be of same shape, size, density and composition. This is not the case; in fact the measured sample is a volume of fuel element material, while the used calibration source is a point source. Thus, two effects needed to be taken into account: the geometric effect and the self-absorption effect. The geometric effect is due to the following aspect: the calibration was performed by means of a point source; the fuel volume considered for each acquired gamma spectrum, is instead a cylinder with radius as the fuel element radius (1.81cm) and height as the collimator radius (1cm). The self-absorption effect is due to the fact that the real sample is a volume of material (the fuel) with a certain density and elemental composition. Before reaching the detector, a gamma photon in the sample can undergo interactions. As an effect, fewer gamma-rays of a specific energy will reach the detector.

Correction factors for both geometric and self-absorption effect were calculated by simulation of the FSM with the MCNP6[13] Monte Carlo code. In Figure 4.10, a section of the FSM simulated with MCNP6 is shown: a fuel element is loaded in the machine; the radial opening, the collimator and the detector position are also visible.

The geometric correction factor was evaluated by running two different simulations (a) and (b).

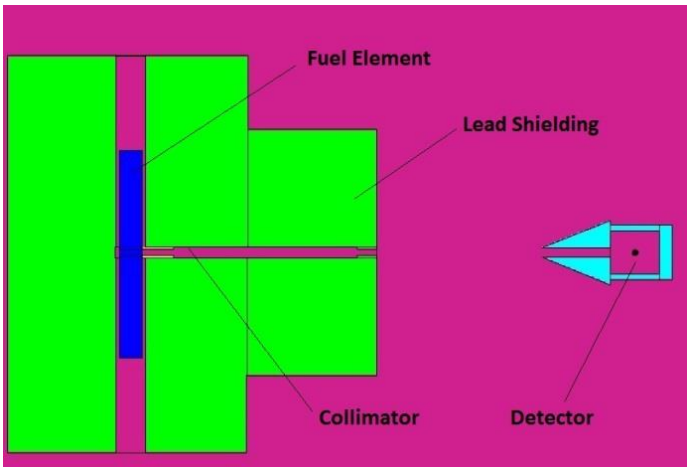

Figure 4.10: MCNP6 section of the Gamma Scanning Machine (GSM) with a fuel element loaded for measurement.

In simulation (a), the gamma source corresponds to a point source (Figure 4.11a) of a defined gamma energy. In simulation (b) (Figure 4.11b), the gamma source is distributed over a cylindrical cell corresponding to a fuel rod disc of 1 cm height. The material filling the source cell is air.

The volumetric correction factor C_{vol} results:

$$C_{vol} = \Phi_a/\Phi_b$$

were Φ_a and Φ_b are the flux values at a point detector placed in the experimental detector position for simulation (a) and (b) respectively.

The self-absorption correction factor was evaluated by comparison of simulation (b) and simulation (c). In simulation (c), the source is distributed over the same volumetric cell like in (b) except for the material, that is the actual fuel material with its composition and density (Figure 4.11c). Thus, the absorption correction factor C_{abs} was calculated as the ratio:

$$C_{abs} = \Phi_b/\Phi_c$$

were Φ_c is the flux value at a point detector placed in the experimental detector position for simulation (c).

The total correction factor C_{tot} that takes into account both geometric and self-absorption effects is then:

$$C_{tot} = C_{vol} \bullet C_{abs} = \Phi_a/\Phi_b \bullet \Phi_b/\Phi_c = \Phi_a/\Phi_c$$

C_{tot} was evaluated by MCNP6 for each detected gamma energy; the values obtained are shown in Table 4.10. The correction factors C_{tot} were used for the evaluation of the activities of the detected fission products as explained later.

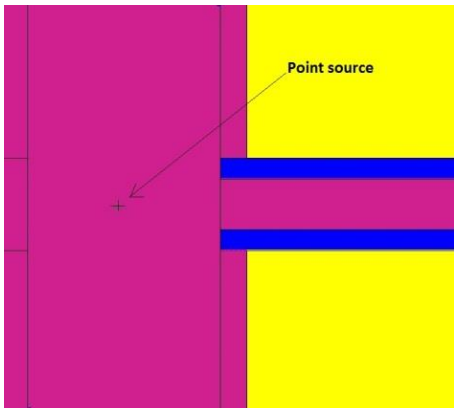

(a) Vertical section of FSM simulation (a) by MCNP6. The gamma source is a point gamma source placed as the gamma calibration source in the real measurement.

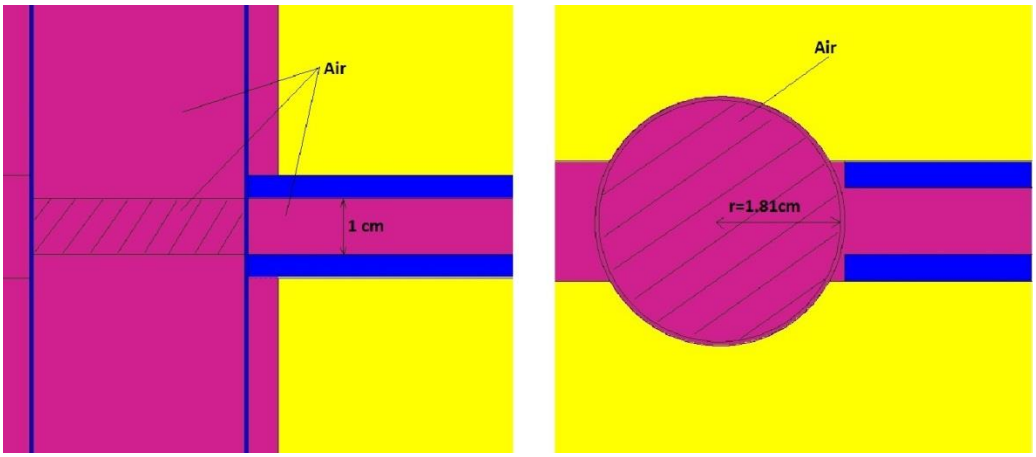

(b) Vertical and horizontal sections of FSM simulation (b) by MCNP6. The gamma source is distributed in a cell corresponding to a fuel cylinder of 1cm height placed in correspondence of the radial opening channel. The material filling the source cylindrical cell is air.

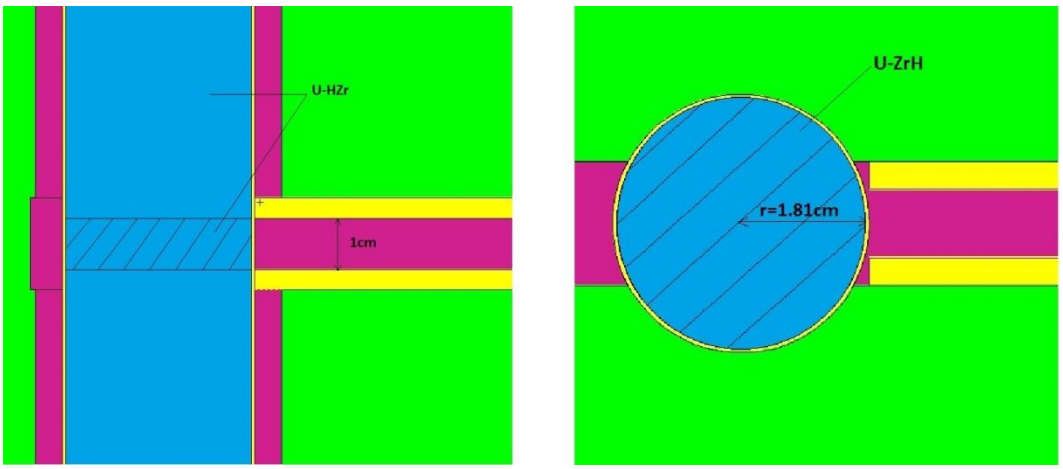

(c) Vertical and horizontal sections of FSM simulation (c) by MCNP. The gamma source is distributed in a cell corresponding to a fuel cylinder of 1cm height placed in correspondence of the radial opening channel. The material filling the source cylindrical cell is fuel (U-HZr).

Figure 4.11: MCNP6 vertical and horizontal sections of the Fuel Scanning Machine (FSM).

Isotope	Half life [29] (days)	Gamma line[29] (KeV)	C_{tot}
Ru-103	39.25	497.08	7.98
Cs137	$1.10 \cdot 10^4$	661.66	6.77
Zr 95	64.03	724.19	6.50
Ce 144 (Pr 144)	284.91	1489.16	4.80

Table 4.10: The total correction factor C_{tot} calculated by MCNP Gamma Scanning Machine simulation.

4.2.3 Fuel elements activity results

The five selected FEs (B2, B4, C1, D1 and E1) were measured in steps of 1 cm along their vertical axis. Thus, to cover the active part of each FE, a total of 38 gamma spectra were gathered and analysed per each FE. Thus, a single spectrum provided the activity of a cylindrical FE volume of 1 cm in height. The sum of the 38 activity values, gave the total activity of a FE.

The measured activity values were obtained as:

$$A = \frac{N}{\varepsilon \gamma t} C_{tot}$$

where N is the net peak area in the spectrum, ε is the efficiency obtained from the point source calibration curve at the photo-peak energy, γ is the emission probability of the corresponding gamma line, C_{tot} is the correction factor for geometric and self-absorption effects defined above. The correction for nuclide decay during counting time is negligible due to the fact that counting is short compared to the half-lives of measured nuclides.

Results are reported in Table 4.11 for the fission product Cs-137, Ce-144, Ru-103 and Zr-95: values represent the total measured activity for each fission product in each fuel element and are referred to time of measurement. As the activity was measured in 38 positions along the fuel elements vertical axis, Figures 4.12 to Figure 4.16 show the vertical distribution of measured activity values for the different fission products in each fuel element.

- As expected, the long life (T1/2=30.08 years) fission product Cs-137 was detected in all the fuel elements and represent the guideline isotope for subsequent burn-up evaluation. Nevertheless, other detected fission products can be useful in the framework of Monte Carlo calculation models verification.

Fuel element		Measured Activity (Bq)			
Position	**ID**	**Cs-137**	**Ce-144**	**Ru103**	**Zr-95**
B2	9213	$(4.62\pm0.34)\cdot10^{10}$	$(8.71\pm0.70)\cdot10^{11}$	$(9.48\pm1.14)\cdot10^{9}$	$(1.82\pm0.14)\cdot10^{11}$
B4	9214	$(4.88\pm0.36)\cdot10^{10}$	$(8.67\pm0.69)\cdot10^{11}$	$(7.95\pm0.95)\cdot10^{9}$	$(1.69\pm0.13)\cdot10^{11}$
C1	9905	$(5.38\pm0.39)\cdot10^{10}$	$(8.79\pm0.70)\cdot10^{11}$	$(7.45\pm0.89)\cdot10^{9}$	$(1.33\pm0.11)\cdot10^{11}$
D1	9915	$(4.92\pm0.36)\cdot10^{10}$	$(7.71\pm0.62)\cdot10^{11}$	$(6.24\pm0.75)\cdot10^{9}$	$(1.24\pm0.10)\cdot10^{11}$
E1	9932	$(3.56\pm0.26)\cdot10^{10}$	$(6.18\pm0.49)\cdot10^{11}$	$(4.61\pm0.55)\cdot10^{9}$	$(8.91\pm0.71)\cdot10^{10}$

Table 4.11: Total measured activity in the different fuel elements for each fission product (values referred to measurment date).

- Among these, Ce-144 is a fission product with half-life of 284.91 days. Its direct gamma emission line at 133keV was too low in energy to be efficiently detected with the used instrumentation. Nevertheless, Ce-144 undergoes 100% beta minus decay to Pr-144 (T1/2 = 17.28 min) with a branching fraction of 0.9885[30]. Pr-144 gamma emission lines (696.51, 1489.16 and 2185.66 keV) were visible in the measured spectra: the measurement of Ce-144 activity was then made through the 1489.16 keV Pr-144 gamma line.
- Ru-103, a fission product with a relatively short half-life (T1/2 = 39.25 days) was also detected in all the measured FEs: the gamma line used for the measurement was at the energy of 497 keV.
- Among the remaining peaks in the spectra, Zr-95 (T1/2 = 64.03 days) was detected in all the FEs at the gamma energy of 724.19 KeV.

4.2.4 Evaluation of fission induced Zr-95 activity

Zr-95 is a fission product but can be also produced through the $Zr^{94}(n,\gamma)Zr^{95}$ reaction, on the Zr with natural isotopic composition consistently present in the TRIGA fuel. Considering the value of this capture reaction cross section (σ_c = 50.69 mbarn[11]) the production of Zr-95 from fission (σ_{fiss} = 585.08 barn[31]) is expected to be predominant. However this aspect needs to be investigated.

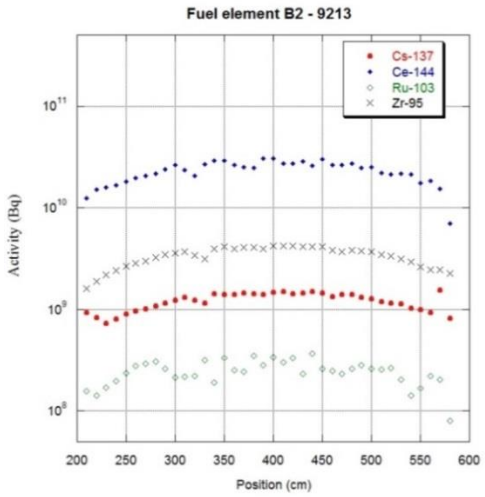

Figure 4.12: Activity vertical distribution in fuel element 9213 (B2).

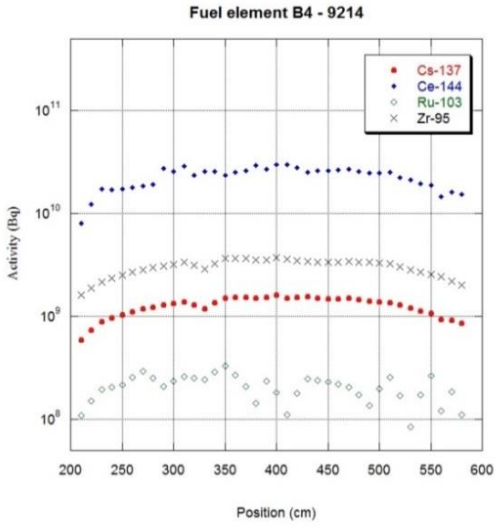

Figure 4.13: Activity vertical distribution in fuel element 9214 (B4).

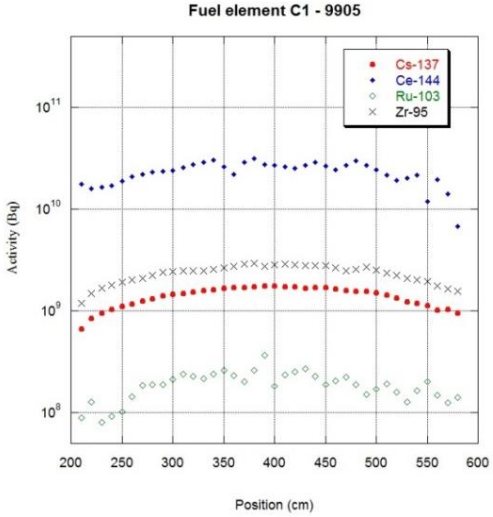

Figure 4.14: Activity vertical distribution in fuel element 9905 (C1).

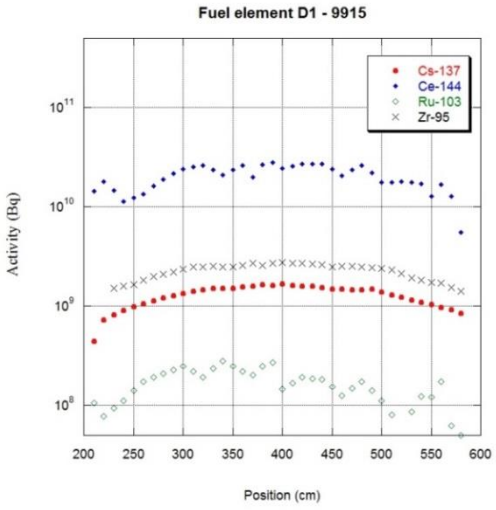

Figure 4.15: Activity vertical distribution in fuel element 9915 (D1).

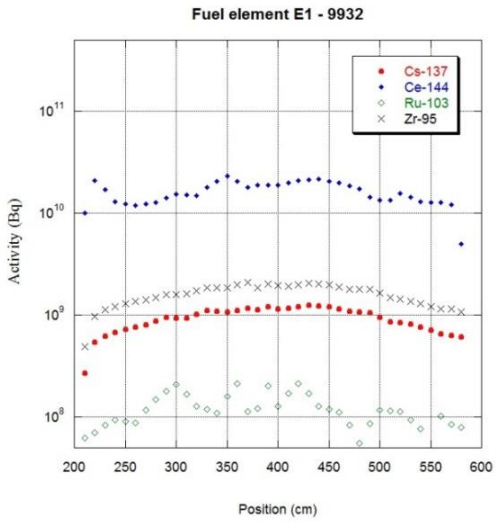

Figure 4.16: Activity vertical distribution in fuel element 9932 (E1).

This evaluation was carried out by means of a dedicated simulation with the MCNP6 code. The neutron source was simulated in MCNP6 with the Inward-cosine function. This option allows to distribute the neutron source over a sphere surface and obtain a constant neutron fluence equal to $1/\pi R^2$ (where R is the radius of the sphere in cm) inside the volume of the sphere. The source energy distribution was simulated using the results of another dedicated MCNP6 simulation, performed running the validated MCNP6 reactor model (see Chapter 3) to evaluate the neutron fluxes distribution inside the FEs. A cylindrical sample with the dimensions of the measured fuel volume (a rod disc of 1 cm height and 1.81 cm radius) was placed in the center of the sphere. The relative density of U-235 and Zr-94 in the fuel material was defined as:

$$\boldsymbol{\rho}_{\text{U-235}} = \boldsymbol{\rho}_{\text{fuel}} \bullet \%_{\text{U-235}}$$

$$\boldsymbol{\rho}_{\text{Zr-94}} = \boldsymbol{\rho}_{\text{fuel}} \bullet \%_{\text{Zr-94}}$$

were ρ_{fuel} is the actual fuel material density; %U-235 and %Zr-94 are the percentages in weight of U-235 and Zr-94 respectively in the fuel.

The cylindrical sample was then filled once with U-235 material at $\rho_{U\text{-}235}$ density and once with Zr-94 material at $\rho_{Zr\text{-}94}$ density. In both cases, the material density was diluted of a factor 10^{-4} to not perturb the flux inside the sample, maintaining constant the ratio $\boldsymbol{\rho}_{U\text{-}235}/\boldsymbol{\rho}_{Zr\text{-}94}$ between the two different simulations. As output, the fission rate R_{fiss} and the capture rate R_c were requested respectively in the case of U-235 and Zr-94.

The ratio K_{fiss}^{Zr-95}, defines the amount of Zr-95 produced by fission over the total amount of Zr-95 produced (by fission plus capture) in the fuel:

$$K_{fiss}^{Zr-95} = \frac{Y_{fiss}^{Zr-95} \cdot R_{fiss}}{Y_{fiss}^{Zr-95} \cdot R_{fiss} + R_c}$$

where Y_{fiss}^{Zr-95} is the Yield of Zr-95 from U-235 fission.

Then the net Zr-95 activity produced from fission reaction (A_{Zr-95}^{fiss}) is obtained by multiplying the measured Zr-95 total activity (A_{Zr-95}^{meas}) for the K_{fiss}^{Zr-95} factor:

$$A_{Zr-95}^{fiss} = K_{fiss}^{Zr-95} \cdot A_{Zr-95}^{meas}$$

K_{fiss}^{Zr-95} was evaluated with separate MCNP6 calculation for every measured FE. The K_{fiss}^{Zr-95} values and the corrected Zr-95 activity (A_{Zr-95}^{fiss}) are shown in Table 4.12.

Fuel element		K_{fiss}^{Zr-95}	A_{Zr-95}^{fiss} (Bq)
Position	**ID**		
B2	9213	0.666	$(1.22\pm0.11)\cdot10^{11}$
B4	9214	0.651	$(1.10\pm0.10)\cdot10^{11}$
C1	9905	0.636	$(8.44\pm0.80)\cdot10^{10}$
D1	9915	0.643	$(7.95\pm0.75)\cdot10^{10}$
E1	9932	0.648	$(5.78\pm0.55)\cdot10^{10}$

Table 4. 12: Calculated K_{fiss}^{Zr-95} values and corrected A_{Zr-95}^{fiss} activity values for Zr-95.

4.2.5 Uncertainty evaluation

The combined uncertainty of the measurement was derived taking into account the relevant sources of uncertainty[32] and applying the error propagation law. The main uncertainty sources are basically the detector efficiency (ε) calibration process and the counting statistic of the measured sample.

The efficiency calibration is affected by an uncertainty due to the following aspects: according to its certificate, the calibration source presents an inherent uncertainty equal to 3%; then, the precision of the calibration source measurement was evaluated by positioning and counting the source different times and resulted within 2%; furthermore, the uncertainty due to the introduction of an interpolation function was estimated according to the method described by Barrera[33] and resulted always lower than 6%. In addition, the geometric and self-absorption correction introduced by means of MCNP6 detector simulation allowed to avoid the introduction of systematic errors in the efficiency calibration determination and keep the relative uncertainty as low as possible.

The uncertainty due to the counting statistic (Area Uncertainty) of the sample varies with the acquired spectrum and the detected gamma lines. In the present case, this Area Uncertainty was calculated by means of the acquisition software[26] as follows:

$$Area\ Uncertainty =$$

$$= \sqrt{Integral + \left(\left(\sum_{i=ROI_{begin-3}}^{ROI_{begin}} Spectrum_i + \sum_{i=ROI_{end}}^{ROI_{end+3}} Spectrum_i\right)\left(\frac{ROI_{end} - ROI_{begin} + 1}{8}\right)^2\right)}$$

$$Integral = \sum_{i=ROI_{begin}}^{ROI_{end}} Spectrum_i$$

where $Spectrum_i$ is the number of counts in the channel i; ROI_{begin} and ROI_{end} are the Region Of Interest (ROI)'s start and stop channel respectively; *i* is the channel number. The Area Uncertainty resulted ranging from an average value of 2% for Cs-137 to 10% for Ru-103 (as the Ru-103 gamma line at 497 keV was constantly affected by the 511keV annihilation peak).

Thus, the total combined uncertainty of the fission product activity varies between 7 and 12% and is reported in Table 4.11 for each measured fission product in the different fuel elements.

4.2.6 Discussion of results

This Chapter described the detection of the activity of selected fission products along the vertical axis of five irradiated FEs at the TRIGA Mark II research reactor of the TU Wien. The measurement was performed in occasion of a planned shut-down by means of a customized Fuel Scanning Machine (FSM). The FEs were scanned after a cooling down period of about 8 months in steps of 1 cm along their vertical axis: as the FEs underwent a relatively short cooling down period, different fission products were detected. The detector was calibrated by means of a certified standard calibration source and by simulation with the MCNP6 Monte Carlo code. Through simulations, the correction factors for geometric and self-absorption effects (C_{tot}) were calculated for each detected nuclide. The results clearly show how the C_{tot} value varies with the gamma energy. Hence, the C_{tot} values were used to calculate the activity of the detected fission products.

In the case of Zr-95 an additional correction factor was introduced to evaluate the amount of Zr-95 produced from fission vs. that produced by neutron capture

reactions. The correction factor was evaluated through a dedicated Monte Carlo simulation and results show that the production of Zr-95 due to fission reaction occurs in the TRIGA fuel for approximately 65% of the overall production.

The results of the measurements coherently show how the detected activity for Ce-144, Ru-103 and Zr-95 depends from the different positions of the FEs in the core: the total activity in fact decreases moving from the inner to the outer ring core positions. Conversely, in the case of Cs-137, the measurements show an increased activity from B ring positions to C ring positions. This is explained by the fact that the FEs in C, D and E rings were not actually fresh when inserted in the core. They were in fact slightly irradiated (burn-up <1%) in another reactor (period 1985-1989). Considering the time elapsed, those fuel elements can be considered fresh for the detection of short-lived fission products (such as Ce-144, Ru-103 and Zr-95), but not for Cs-137 detection. Thus, the higher value of Cs-137 in the C ring can be explained by the contribution of Cs produced in the 1980s and still present. Nevertheless, comparing Cs-137 activity results of FEs with a comparable irradiation history (i.e. FEs in C1, D1, E1), it can be seen that the values again decrease coherently moving from inner to outer ring core positions.

The experimental results presented in this Chapter can be used for validation of the Monte Carlo calculation models (see Chapter 5) of the TRIGA reactor at the TU Wien.

Chapter 5

Serpent reactor model validation

The present chapter describes the use of the Serpent Monte Carlo calculation code to perform an important part of this PhD project.
After an introduction to Serpent main characteristics and capabilities (5.1), the implementation of a new model (5.2) for the TRIGA Mark II reactor of the TU Wien by means of Serpent is described. Decision taken for the development of the geometry, the utilization of material cards and other options are presented.
Then the procedure for the validation (5.3) of the new Serpent model is described in detail. Experiments performed in Chapters 2 and Chapter 4 respectively for neutron spectrum evaluation and burn-up determination are reproduced with Serpent (5.3.1 and 5.3.2). The results are compared with both experimental ones and with MCNP calculated results (Chapter 3).

5.1. Serpent code

The Serpent[37,38] code is a continuous-energy Monte Carlo reactor physics burnup calculation code, developed at the VTT Technical Research Centre of Finland from 2004, under the working title "Probabilistic Scattering Game", or PSG[39].
Since 2009 Serpent-1 is available at OECD/NEA Data Bank and RSICC. In 2010 the code was re-written and Serpent-2 version was developed. Currently Serpent-2 is in the Beta-Testing Phase: this version is the one used for the present PhD project and from here on, whenever Serpent is named in the text, it is intended to refer to this version.

Serpent code is constantly evolving[40] and its applications can be summarized into three categories:

- Traditional reactor physics applications, including spatial homogenization, criticality calculations, fuel cycle studies, research reactor modelling, validation of deterministic transport codes, etc;
- Multi-physics simulations, i.e. coupled calculations with thermal hydraulics and fuel performance codes;
- Neutron and photon transport simulations for radiation dose rate calculations, shielding, fusion research and medical physics.

5.1.1. Geometry and particle tracking

Similar to other Monte Carlo codes, the geometry description in Serpent relies on a universe-based constructive solid geometry model, which allows the description of practically any two- or three-dimensional fuel or reactor configuration. This geometry consists of homogeneous material cells, defined by elementary and derived surface types that are combined using Boolean operators (intersections, unions and complements). Serpent also supports square and hexagonal lattices, and provides special geometry types for CANDU and randomly-dispersed particle fuels. In addition to universe-based geometry, Serpent has the option to import CAD and unstructured mesh based geometries.

Particle transport in Serpent is based on the combination of conventional surface-tracking and the Woodcock delta-tracking method[41]. The tracking routine works efficiently for geometries where the particles (neutron or photon) mean-free-path is long compared to the dimensions. This is typically the case in reactor physics calculations involving fuel assemblies and especially HTGR micro-particle fuels. Complex geometries with highly-refined spatial detail are also encountered in various fusion applications. The traditional delta-tracking method is subject to certain efficiency problems related to localized heavy absorbers, which in Serpent are avoided by switching to surface-tracking when necessary[40].

The main disadvantage of delta-tracking is that the track-length estimate of particle flux is not available, and reaction rates have to be calculated using the potentially less-efficient collision estimator. This is usually not a problem in reactor

calculations when reaction rates occur in regions of high collision density. When the collision rate is low, the efficiency of the estimator can be improved by introducing additional virtual collisions over the particle flight path. Serpent also provides a special detector type based on the track-length estimator for calculating reaction rates in small or thin volumes, in which the efficiency of the collision estimator is poor[42].

5.1.2. Serpent physics

The interaction physics is based on classical collision kinematics, ENDF reaction laws and probability table sampling in the unresolved resonance region. Improved treatment for the free-gas scattering kernel near resonances is also available, based on the DBRC Doppler-broadening rejection correction method[43].

Serpent reads continuous-energy cross sections from ACE format data libraries. Those libraries, based on JEF-2.2, JEFF-3.1, JEFF-3.1.1, ENDF/B-VI.8 and ENDFB/B-VII evaluated data files, are included in the installation package of Serpent 1. Interaction data is available for 432 nuclides at 6 temperatures between 300 and 1800K. Thermal bound-atom scattering data is included for light- and heavy-water plus graphite. Since the data format is shared with MCNP, any continuous-energy ACE format data library generated for MCNP can be used with Serpent as well. The data format determines the "laws of physics" for neutron interactions, and the results from Serpent calculations can be expected to agree with MCNP to within statistics.

Unionized energy grid format

Cross sections read from the libraries are reconstructed on a single unionized energy grid, used for all reaction modes[44], resulting in a major speed-up in calculation, as the number of CPU time consuming grid search iterations is reduced to minimum. Macroscopic cross sections for each material are pre-generated before the transport simulation. Instead of calculating the cross sections by summing over the constituent nuclides during tracking, the values are read from pre-generated tables to improve the performance.

Nevertheless, the unionized energy grid approach is a very computer memory consuming process, as redundant data points are stored. The grid size may become too large in burnup calculations, often involving more than 250 actinide and fission product nuclides. To overcome this issue, Serpent 2 provides different optimization modes for burnup calculation problems, in which the unionized energy grid approach is used selectively[45]. The lowest optimization modes allow running large burnup calculation problems with tens or hundreds of thousands of depletion zones, while the higher modes provide considerable speed-up in assembly-level calculations.

Cross sections temperature adjustment

As the data in the cross section libraries is available only in 300K temperature intervals, a more accurate description of the interaction physics in temperature-sensitive applications may be required. This capability is possible in Serpent by use of a built-in Doppler-broadening pre-processor routine[46] that allows adjusting the temperatures of ACE format cross sections. The method has been validated with good results and the routine works efficiently without significant computational overhead.

Photon transport mode

Photon physics routines were implemented in Serpent 2 in 2015[47]. The physics model currently covers the basic photon interactions (Rayleigh and Compton scattering, photoelectric effect and electron-positron pair production) for energies ranging from 1 keV to 100 MeV. Secondary photons are produced by atomic relaxation and bremsstrahlung, handled using the thick-target bremsstrahlung (TTB) approximation. The physics model is comparable to the methods used in other Monte Carlo transport codes (e.g., MCNP6, Geant4, FLUKA). In addition to the standard ACE format cross section libraries, Serpent reads photon interaction data from supplementary data files, which is why the physics model is not fully compatible with that used in MCNP.

The original reason for developing a photon transport mode was to take into account gamma heating in coupled multi-physics simulations. A coupled neutron-

photon transport mode was implemented in Serpent in 2017, and the development of advanced heat deposition models is still under way. This implementation of photon physics routines will broaden the scope of Serpent applications from reactor physics calculations to radiation transport and shielding.

5.1.3. Burnup calculation

The burnup calculation capability in Serpent is entirely based on built-in calculation routines, without coupling to any external solvers. The number of depletion zones is not restricted, although memory usage may require reducing the optimization when the number of burnable materials is large.

Fission-, activation-products and actinide daughter nuclides are automatically selected for the calculation, and burnable materials can be sub-divided into depletion zones. The irradiation history is defined in units of time or burnup. Reaction rates are normalized to total power, specific power density, flux, fission or source rate, and the normalization can be changed by dividing the irradiation cycle into a number of separate depletion intervals. A restart features allows performing fuel shuffling or applying any modifications in the input by dividing the calculation into several parts.

Radioactive decay and fission yield data used in the calculation is read from standard ENDF format data libraries. The decay libraries may contain data for almost 4000 nuclides and meta-stable states, even if the number of nuclides produced from fission, transmutation and decay reactions is generally lower, in the order of 1500.

Flux-volume-averaged one-group transmutation cross sections are calculated either during the transport simulation, or by collapsing the continuous-energy reaction cross sections after the calculation has been completed using a flux spectrum collected on the unionized energy grid. The spectrum collapse method speeds up the calculation by a factor of 3-4, and due to the high energy resolution of the flux spectrum, the errors in the results are practically negligible. Similar methodology has been used with other coupled Monte Carlo burnup calculation codes[48].

Serpent has two options for solving the Bateman depletion equations. The first method is the Transmutation Trajectory Analysis (TTA) method[49], based on the

analytical solution of linearized depletion chains. The second option is the Chebyshev Rational Approximation Method (CRAM), an advanced matrix exponential solution developed for Serpent at VTT[50]. Both methods have shown to produce consistent results when used with Serpent.

Fission product poisons Xe-135 and Sm-149 can be handled separately from the other nuclides, and iterated to their equilibrium concentration during the transport simulation. The equilibrium calculation is independent of the depletion routine, and the iteration can also be performed in transport mode without burnup calculation.

Variance reduction

When Serpent started out as a reactor physics code, obtaining sufficient statistics for the results was just a matter of running a sufficient number of neutron histories. The uniform fission site method was later implemented to improve the statistical accuracy in full-core calculations, in which the outermost fuel pins in assemblies located at the core-reflector boundary typically receive a low number of scores.

The implementation of more efficient general-purpose variance reduction techniques was started recently. The methodology relies on a conventional super-imposed weight-window mesh. The importances used for obtaining the weight-window boundaries can be produced by external calculation tools, or using a built-in light-weight solver based on the response-matrix method. Serpent can read standard MCNP WWINP format files, although the methodology is still under development and subject to several limitations.

5.2. Serpent reactor model implementation

5.2.1. Geometric description of the TRIGA reactor

The three-dimensional model of the TRIGA reactor of TU Wien was developed by means of Serpent code. A top view of the reactor model is shown in Figure 5.1.

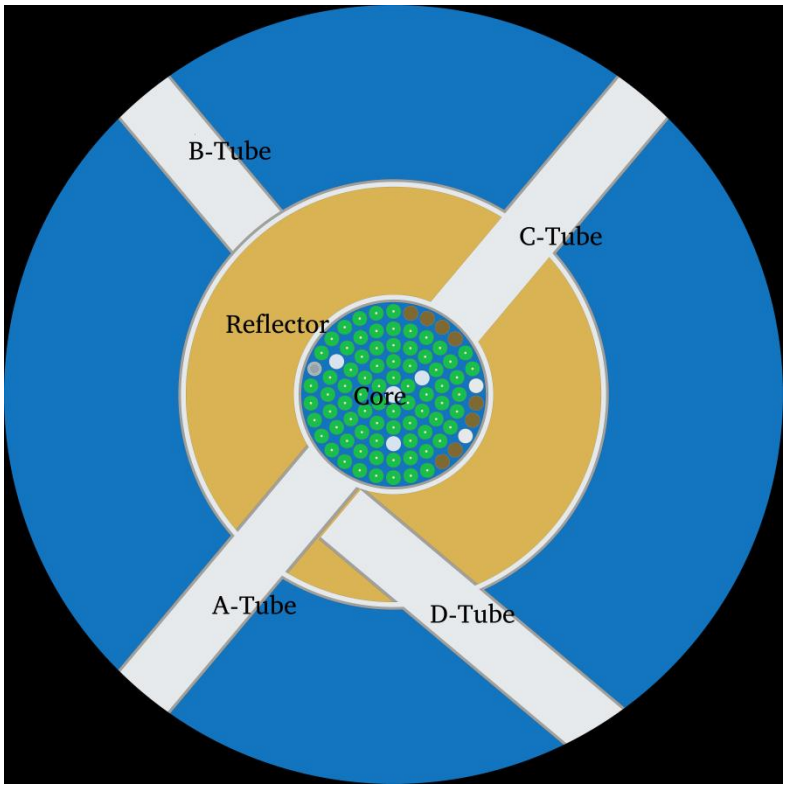

Figure 5. 1: Top view of the reactor obtained with Serpent (z = -9.65 cm).

The origin of the Serpent geometry is in the centre of the core. The detailed geometry and material information was reproduced exactly as in the described MCNP model (3.2.1).

The same simplifications as in the MCNP model were kept: for example, in case of the fuel elements (Figure 5.2(b)), the aluminium fixture at the bottom and the top of every FE were not modelled, as this is supposed to have no significant effect on the neutron transportation calculation inside the core.

The colours in the plot (Figure 5.2) represent different materials. The figure is a cross section of the FE, the cylindrical Zr-rod is surrounded by the fuel meat (green). At the top and the bottom of the FE vertical graphite reflectors (brown) are placed. At the lower part of the FE a Molybdenum-disk is placed.

The control rods were not shown because the burnup simulation runs at full power (250 kW) and the control rods are all simulated in their fully up position, then out of the core. The model shows water at the position where the control rods are usually placed. The horizontal beam tubes and the annular groove graphite reflector can also be seen in the top view of the reactor (Figure 5.1).

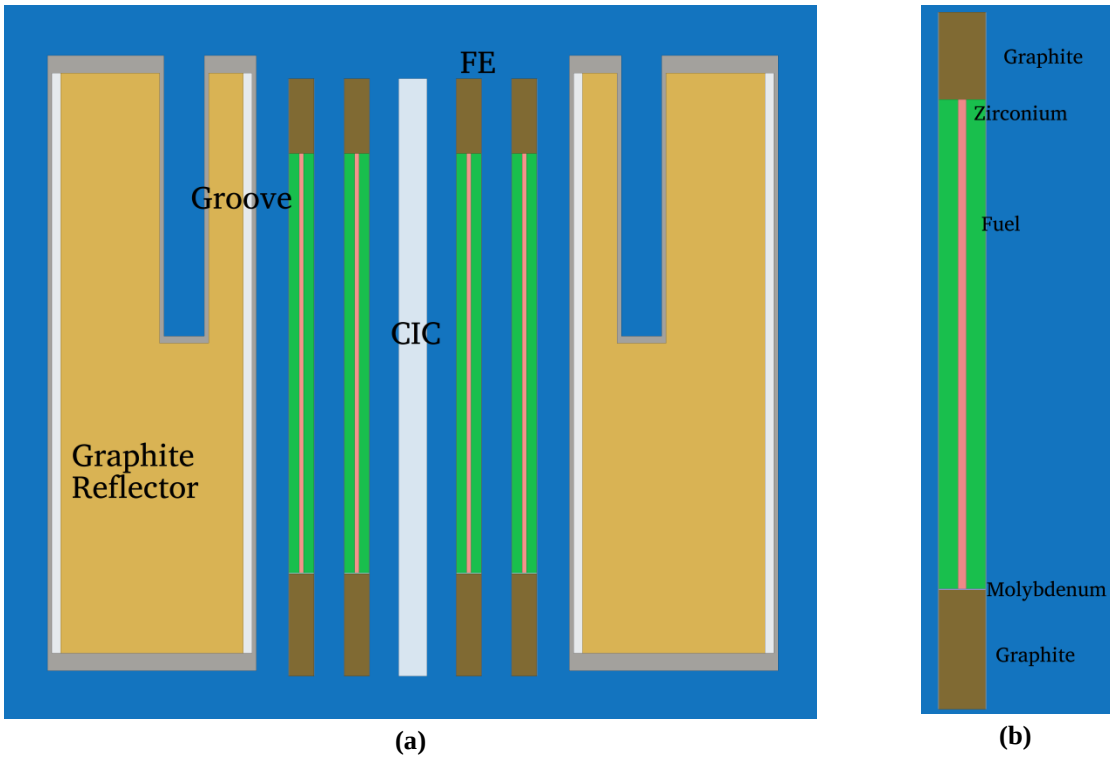

Figure 5. 2: Serpent vertical plots of the core at y= 0 cm (a) and of one fuel element (b).

Surface cards are needed to define the border of the cells. The surfaces most often used in the input file of the reactor were: sphere, cylinder and plane surfaces. The syntax to define a surface in Serpent is:

surf <id> <type> <para1> <para2> ...

where <id> is the surface identifying number set by the user; type is the type of the surface (e.g. sphere, plane, etc.); <para-i> can be different parameters (e.g. for a sphere, the origin coordinates (x, y, z) and the radius).

Cell cards define cells, each cell is filled with a material, while the borders are bound by surfaces. The Serpent syntax for a cell card looks as follows:

cell <id> <uni> <mat> <surf1> <surf2> ...

where <id> is again a number to identify the cell; <uni> is the universe number; <mat> is the name of the material that fills the cell; <surf-i> are all the surfaces that bound the cell.

Serpent uses different universes to nest parts into each other. The universes are identified by user-defined numbers; the most outer universe should have the number “0”. The universe structure of the TRIGA reactor is now described.

Universes and structure of the input file

The core elements were modelled separately and placed afterwards in the actual position. The fuel cylinder was modelled with the origin at x=0 cm, y=0 cm and then placed in a lattice. This was done the same way for every core element, such as control rods, dummy graphite elements, the neutron source and irradiation tubes. Every element has its own universe number, e.g the fuel elements have the universe number 10 and the dummy graphite elements have the number 11. This universe number is used to arrange them in the annular core lattice.

The core of the TRIGA reactor Vienna presents a cylindrical geometry and Serpent has a predefined lattice for this type of array amongst other. This predefine lattice structure can be filled by regular structure of other universes, like the fuel pins and dummy graphite elements. The syntax for the TRIGA reactor core is:

lat 100 4 0 0 6

where “lat” is the command for the predefined lattice structure; 100 is the universe number of the lattice (i.e. the universe of the reactor core); 4 is the lattice type (i.e. a circular cluster array);”0 0” are the origin coordinates (x,y); and 6 are the number of rings in the lattice. A list of rings is subsequently defined as follows:

$$<n> <r> <\vartheta> <u_1> <u_2> \ldots <u_n>$$

n is the number of elements in the ring; r is the radius of the ring; ϑ is the angle of rotation; and n is the number of the universes filling this ring. In the case if the TRIGA reactor the inner ring (A-ring) has 1 element and the next ring (B-ring) 6 elements: i.e.n is equal to 1 and 6 respectively. The radius of the A-ring is 0 cm and 4.15 cm for the B-ring. To arrange the core in Serpent the same way as in MCNP input file, the rings are rotated by 30°.

Between the core elements and around the core, water is placed. The core universe 100 is filled by the core components with their own universe numbers.

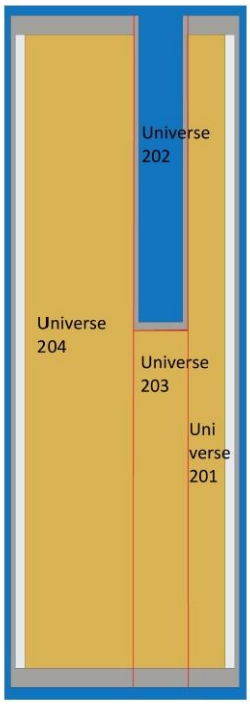

Figure 5. 3: Detail of the Graphite Reflector, for the Serpent Simulation the reflector is divided into four universes, the red lines are their boundaries

Furthermore the reflector is designed separately. The graphite reflector is cladded with aluminium, between the cladding and the graphite is an air gap (Figure 5.3). The annular grooved for irradiation experiments is placed in the reflector. To avoid any geometry errors by Serpent (like through overlapping cells) the reflector was divided into four parts, each with its own universe number (u=201, 202, 203, 204).

The four beam tubes passing through the reflector and the water tank (Figure 5.1) were modelled separately; then the reflector universe was filled by the tubes. The core and the reflector with the tubes are then placed in the water tank. The water tank is the outermost universe so it has the number “0”. It is filled by the core and the four parts of the reflector, plus the parts of the beam tubes in the water tank (see figure 4.1.1).

The material of the cell beyond the tank is “outside”, this means, that the boundaries for the Serpent calculations are set to the tank extension.

5.2.2. Material Cards

The neutron reaction data which Serpent uses for transportation calculation are taken from the OECD/NEA Data Bank. For the performed calculations the ENDF/B-VII library was selected.

The material specification of the problem are defined in the Serpent input file in the form of material cards, one for each material in the problem. The material card sets the name of the material and its density (mass or atomic), followed by a list of the nuclides that constitute the material with the corresponding fraction (in mass or atomic).

The materials were reproduced in the Serpent input as done for MCNP input. In particular it has to be noted that the fuel material in all fuel elements was defined as fresh fuel (Table 5.1): this is an approximation as in the reality the major part of the fuel elements were slightly irradiated in the past (4.2.6) before their first load in the TRIGA reactor at TU Wien.

Additionally, treating thermal systems by using free-atom cross section would introduced significant errors. To avoid this, a thermal scattering card was introduced to provides correct reactions data for moderator materials. For materials like water, graphite and Zirconium-Hydrogen thermal scattering cards were taken from the MCNP6 libraries and transfers to the Serpent libraries.

Nuclide	Mass Fraction
U-235	0.0166
U-238	0.0667
Zr-90	0.9012
H-1	0.0155

Table 5. 1: fresh fuel composition used in Serpent input file.

5.2.3. Parameters of the Serpent Calculation

The typical parameters of the following Serpent simulation consisted in 1500 cycles, where the first 70 cycles are skipped, with 1 million source neutron in each cycle. The model started with the initial k_{eff} = 1 and after 70 cycles the k_{eff} value become stable and acceptable. The unresolved resonance probability tables were switched on.

The main output file from the Serpent simulation consists of many values and parameters. First, the file lists the technical parameters under which the simulation runs and the user-defined options. In addition, it contains all the results of the calculation, such as criticality eigenvalues, radioactivity data, normalisation coefficient and the normalized total reaction rates, forward-weighted delayed neutron parameters and some more.

5.3. Serpent model validation

The validation[51,52] of the developed Serpent-2 model was carried out in two steps.
The first step consisted in calculating the neutron flux and neutron energy spectrum at several positions and benchmark the results against those obtained in the corresponding positions by use of the validated MCNP6 model (see Chapter 3).
On the other side, the second step consisted in the simulation with Serpent-2 model of the experiments described in Chapter 4, thus focussing on burn-up calculation. The obtained results were then compared with the experimental values to evaluate the capability of Serpent-2 model to reproduce the core behaviour during irradiation/operation.

5.3.1. Serpent neutron spectrum calculation

The first part of the Serpent model validation consisted in the Serpent evaluation of the neutron flux at the same positions defined both for the flux measurement campaign (see Chapter 2) and for the MCNP flux determination (see Chapter 3).
The neutron flux was then calculated at four different in-core positions (POS6, b, i and o) along the radial direction, and at 11 in-core positions (POS1, POS2, …, POS11) along the vertical direction in the Central Thimble (CT). The exact distances that define each position can be found in Table 2.3.
One of Serpent capability is to visualize the neutronics in thermal systems by plotting the fission power and thermal flux distributions in a graphics file; furthermore, burn-up mode produces new plots for each depletion step. A visualisation of the thermal flux calculated with the current Serpent reactor model is reported in Figure 5.4. The colour scheme consists of shades of red and yellow, representing relative fission power, and shades of blue, representing relative thermal flux (< 0.625 eV).

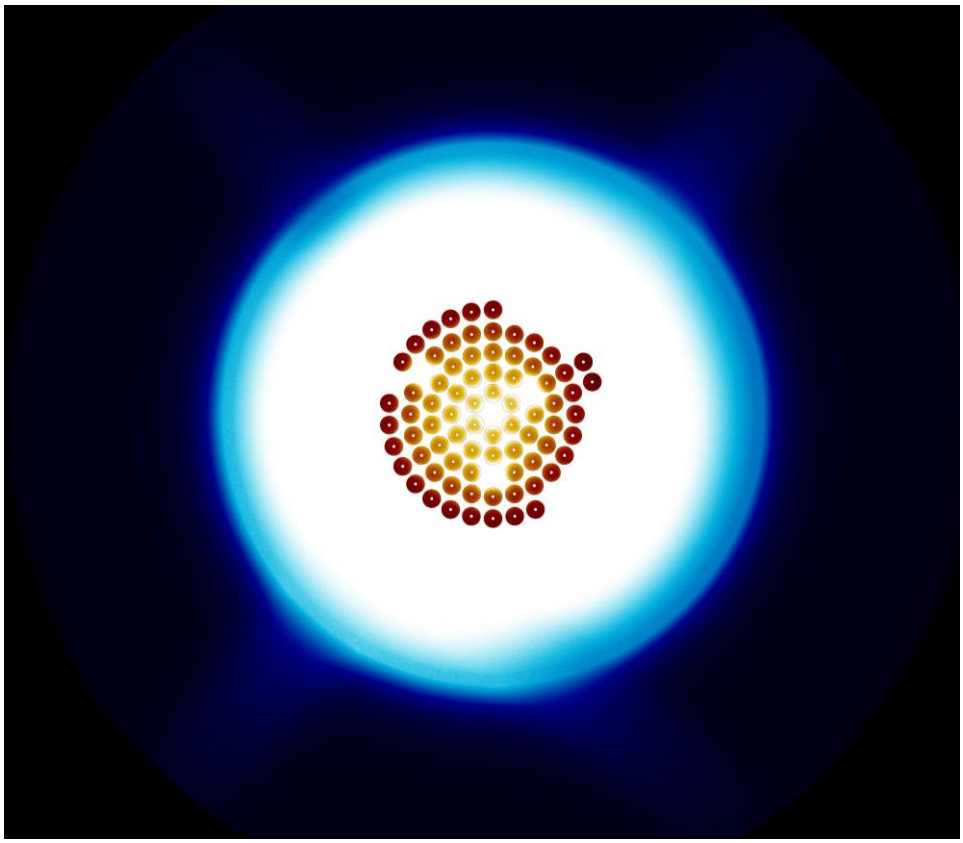

Figure 5. 4: Mesh plot of the relative thermal flux (blue and white shades) and relative fission power (red and yellow shades) created by the Serpent program at z = 0 cm

For flux calculation, at the positions of interest, a cell detector was used. The detector cell was a sphere with a radius of 0.6 cm, that is, of dimensions comparable to those of the irradiated samples used for flux determination (Chapter 2) . The reactor power was set to 250 kW.

As an output, the differential flux for every position was required over 30 energy intervals between 0 and 18 MeV. The width of the energy intervals was selected to represent constant lethargy intervals as in the corresponding MCNP6 calculation.

Radial Direction results

The differential neutron spectrum, in one of the characterized positions, over the 30 energy intervals obtained both with MCNP6 and Serpent-2 reactor model is reported in Figure 5.5. The integral flux was derived by multiplying the differential flux values by the width of the corresponding energy interval: the obtained thermal-(0 – 6.9 x 10-7 MeV) and total-flux (0-18MeV) are reported in Table 5.2. The comparison with the MCNP6 values is reported in Figures 5.6 and 5.7.

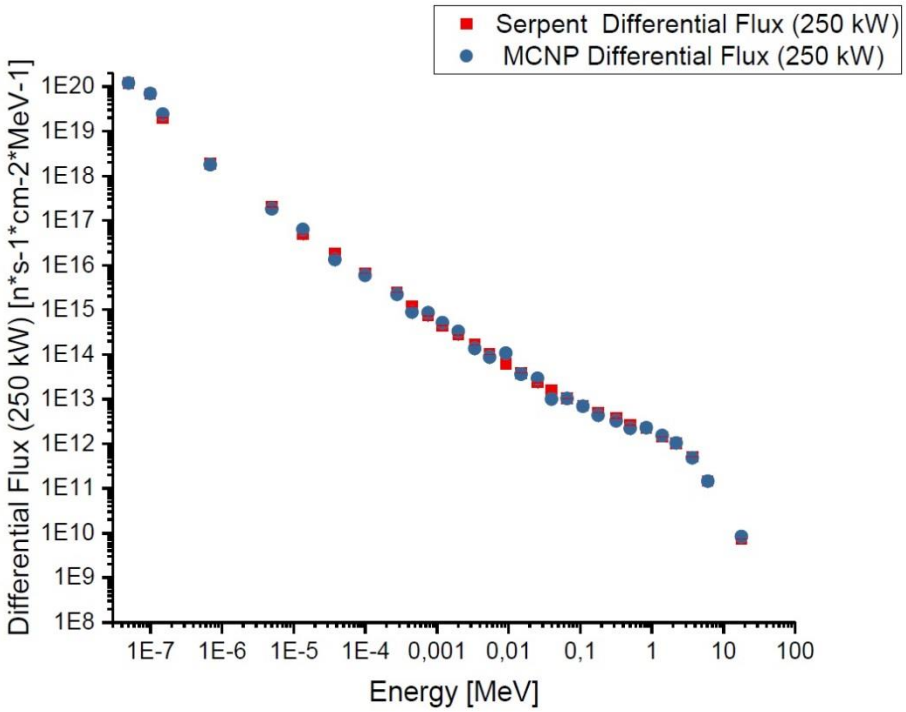

Figure 5.5: The differential neutron spectrum over the 30 energy intervals obtained both with MCNP6 and Serpent-2 reactor models.

Radial core position	Thermal Flux (<0.69eV) [n •s-1 • cm-2]		Total Flux [n •s-1 • cm-2]	
	Serpent	MCNP6	Serpent	MCNP6
Position 6	$1.13 \cdot 10^{13}$	$1.16 \cdot 10^{13}$	$2.16 \cdot 10^{13}$	$2.17 \cdot 10^{13}$
b	$7.24 \cdot 10^{12}$	$7.68 \cdot 10^{12}$	$1.91 \cdot 10^{13}$	$1.94 \cdot 10^{13}$
i	$5.23 \cdot 10^{12}$	$5.52 \cdot 10^{12}$	$1.42 \cdot 10^{13}$	$1.51 \cdot 10^{13}$
o	$2.44 \cdot 10^{12}$	$2.84 \cdot 10^{12}$	$6.20 \cdot 10^{12}$	$6.84 \cdot 10^{12}$

Table 5. 2: Thermal- and Total- neutron flux results obtained by Serpent and MCNP6 calculation (reactor power 250 kW) along the core radial direction.

Vertical Direction results

For the vertical direction flux evaluation, 11 sphere cell-detectors (again with radius of 0.6 cm) were placed in the Central Thimble (CT). The obtained thermal- and total-fluxes are reported in Table 5.3 and compared with MCNP6 results in the Figures 5.8 and 5.9.

The comparison with the MCNP6 results shows that the two Monte Carlo models are in very good agreement within the statistical error (<1% Serpent, <3%MCNP6) through the reactor core.

As it could be expected, the further away from the centre of the core the neutron flux is evaluated, the greater the difference between Serpent and MCNP.

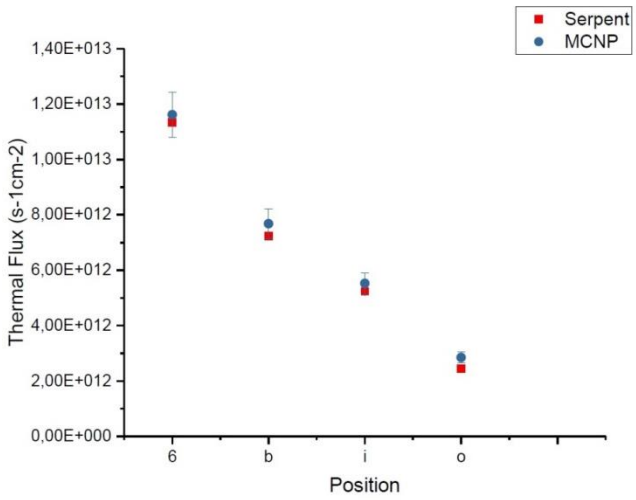

Figure 5.6: Thermal Flux along the radial direction of the core obtained by Serpent and MCNP6 calculation.

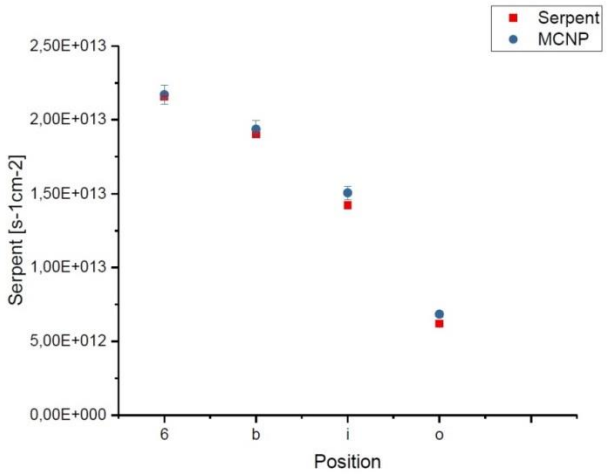

Figure 5. 7: Total Flux along the radial direction of the core obtained by Serpent and MCNP6 calculation.

Vertical core position	Z (cm)	Thermal flux (<0.69eV) [n •s-1 • cm-2]		Total Flux [n •s-1 • cm-2]	
		Serpent	MCNP6	Serpent	MCNP6
Position 1	**20**	$4.62 \cdot 10^{12}$	$4.37 \cdot 10^{12}$	$7.79 \cdot 10^{12}$	$7.43 \cdot 10^{12}$
Position 2	**16**	$6.21 \cdot 10^{12}$	$6.61 \cdot 10^{12}$	$1.17 \cdot 10^{13}$	$1.24 \cdot 10^{13}$
Position 3	**12**	$8.28 \cdot 10^{12}$	$8.34 \cdot 10^{12}$	$1.58 \cdot 10^{13}$	$1.58 \cdot 10^{13}$
Position 4	**8**	$9.96 \cdot 10^{12}$	$1.00 \cdot 10^{13}$	$1.90 \cdot 10^{13}$	$1.90 \cdot 10^{13}$
Position 5	**4**	$1.10 \cdot 10^{13}$	$1.11 \cdot 10^{13}$	$2.09 \cdot 10^{13}$	$2.10 \cdot 10^{13}$
Position 6	**0**	$1.13 \cdot 10^{13}$	$1.16 \cdot 10^{13}$	$2.16 \cdot 10^{13}$	$2.17 \cdot 10^{13}$
Position 7	**-4**	$1.10 \cdot 10^{13}$	$1.14 \cdot 10^{13}$	$2.09 \cdot 10^{13}$	$2.15 \cdot 10^{13}$
Position 8	**-8**	$9.91 \cdot 10^{12}$	$1.08 \cdot 10^{13}$	$1.89 \cdot 10^{13}$	$2.01 \cdot 10^{13}$
Position 9	**-12**	$8.22 \cdot 10^{12}$	$7.91 \cdot 10^{12}$	$1.56 \cdot 10^{13}$	$1.54 \cdot 10^{13}$
Position 10	**-16**	$6.16 \cdot 10^{12}$	$5.93 \cdot 10^{12}$	$1.16 \cdot 10^{13}$	$1.12 \cdot 10^{13}$
Position 11	**-20**	$4.35 \cdot 10^{12}$	$4.61 \cdot 10^{12}$	$7.44 \cdot 10^{12}$	$7.65 \cdot 10^{12}$

Table 5. 3: Thermal- and Total- neutron flux results obtained by Serpent and MCNP6 calculation (reactor power 250 kW) along the core vertical axis.

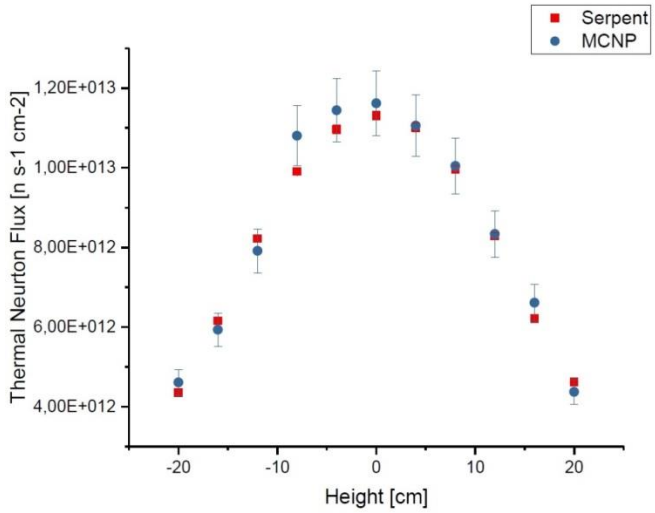

Figure 5.8: Thermal Flux along the vertical direction of the core (in the Central Thimble) obtained by Serpent and MCNP6 calculation.

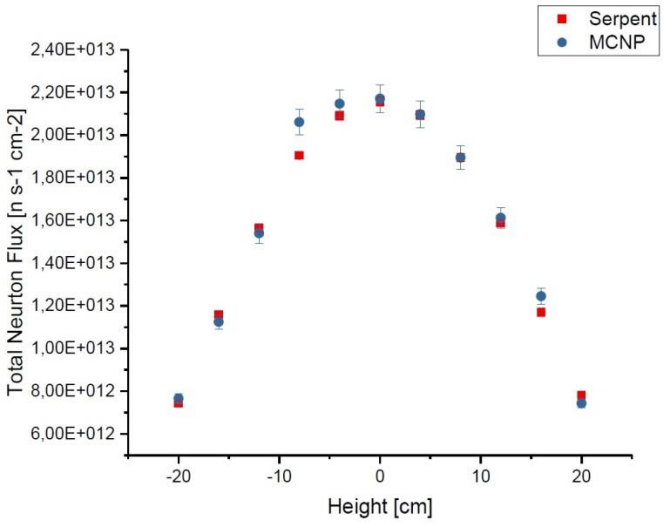

Figure 5.9: Total Flux along the vertical direction of the core (in the Central Thimble) obtained by Serpent and MCNP6 calculation.

Serpent flux calculation within the Fuel Elements

For burn-up calculation the behaviour of the neutron fluxes inside the fuel elements is of interest. Hence, an additional verification of the Serpent model was performed by calculation of the neutron flux inside one fuel element (FE 9213 in Position B2) and compared with an equivalent MCNP6 calculation.

In both models, the fuel active part inside the FE was divided into 9 cylindrical cells (with exclusion of the Zirconium rod) along the z-axis.

A detector cell was used to estimate the flux into each cell. The obtained total- and thermal-fluxes (Table 5.4) are shown in the plots in Figures 5.10 and 5.11. With statistical error in the order of less than 1% for Serpent simulation and less than 3% for MCNP, it was concluded that the difference in the results provided by the two models is insignificant, the highest being 5%.

		Thermal Flux (<0.69eV) [n •s-1 • cm-2]	
		MCNP6	**Serpent**
Fuel Element		**B2**	**B2**
Volume cell	**Cell centre along z axis (cm)**		
Cell 1	**16**	$2.92 \cdot 10^{12}$	$2.86 \cdot 10^{12}$
Cell 2	**12**	$3.95 \cdot 10^{12}$	$3.76 \cdot 10^{12}$
Cell 3	**8**	$4.84 \cdot 10^{12}$	$4.58 \cdot 10^{12}$
Cell 4	**4**	$5.44 \cdot 10^{12}$	$5.12 \cdot 10^{12}$
Cell 5	**0**	$5.61 \cdot 10^{12}$	$5.32 \cdot 10^{12}$
Cell 6	**-4**	$5.40 \cdot 10^{12}$	$5.15 \cdot 10^{12}$
Cell 7	**-8**	$4.88 \cdot 10^{12}$	$4.62 \cdot 10^{12}$
Cell 8	**-12**	$3.93 \cdot 10^{12}$	$3.79 \cdot 10^{12}$
Cell 9	**-16**	$2.89 \cdot 10^{12}$	$2.87 \cdot 10^{12}$

Table 5. 4: Thermal neutron flux profile along the z axis calculated by Serpent and MCNP6 models within the fuel element in position B2.

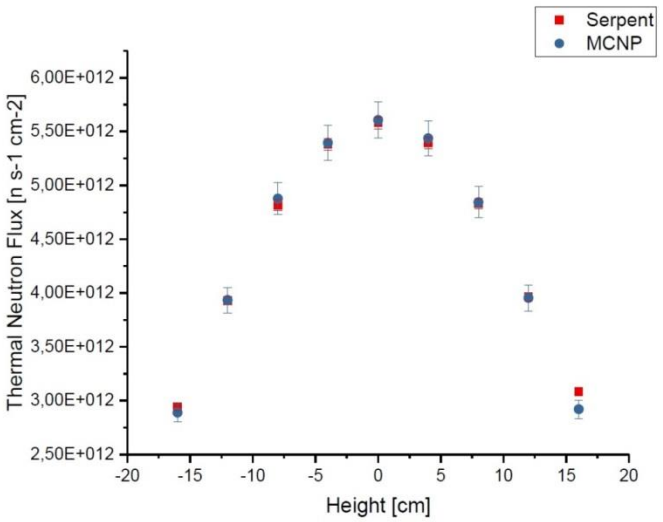

Figure 5. 10: Thermal Flux within the fuel element B2 (along the vertical direction) obtained by Serpent and MCNP6 calculation.

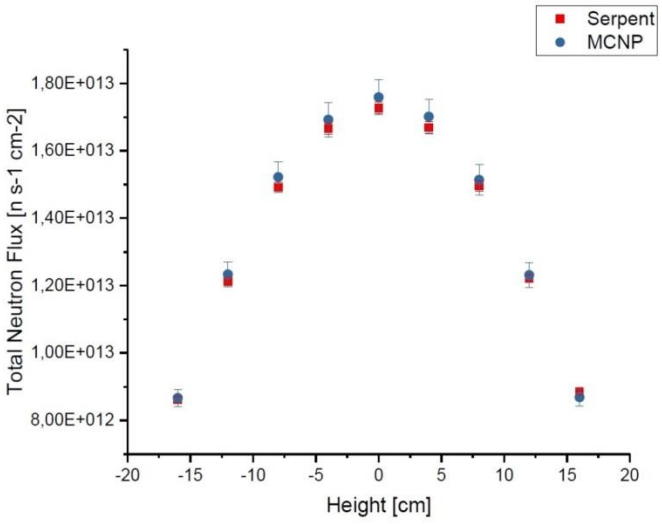

Figure 5. 11: Total Flux within the fuel element B2 (along the vertical direction) obtained by Serpent and MCNP6 calculation.

The neutron flux was then calculated with Serpent in various fuel elements from ring B to ring E (Table 5.5). The thermal- and total-neutron flux in the different fuel elements can be seen in Figures 5.12 and 5.13.

		Thermal Flux (<0.69eV) [n •s-1 • cm-2]			
		Serpent			
Fuel Element		B4	C1	D1	E1
Volume cell	Cell centre along z axis (cm)				
Cell 1	16	$2.79 \cdot 10^{12}$	$2.40 \cdot 10^{12}$	$1.96 \cdot 10^{12}$	$1.56 \cdot 10^{12}$
Cell 2	12	$3.76 \cdot 10^{12}$	$3.21 \cdot 10^{12}$	$2.72 \cdot 10^{12}$	$2.13 \cdot 10^{12}$
Cell 3	8	$4.61 \cdot 10^{12}$	$3.94 \cdot 10^{12}$	$3.34 \cdot 10^{12}$	$2.59 \cdot 10^{12}$
Cell 4	4	$5.16 \cdot 10^{12}$	$4.40 \cdot 10^{12}$	$3.73 \cdot 10^{12}$	$2.89 \cdot 10^{12}$
Cell 5	0	$5.34 \cdot 10^{12}$	$4.56 \cdot 10^{12}$	$3.86 \cdot 10^{12}$	$3.00 \cdot 10^{12}$
Cell 6	-4	$5.16 \cdot 10^{12}$	$4.40 \cdot 10^{12}$	$3.73 \cdot 10^{12}$	$2.90 \cdot 10^{12}$
Cell 7	-8	$4.62 \cdot 10^{12}$	$3.95 \cdot 10^{12}$	$3.35 \cdot 10^{12}$	$2.62 \cdot 10^{12}$
Cell 8	-12	$3.75 \cdot 10^{12}$	$3.22 \cdot 10^{12}$	$2.74 \cdot 10^{12}$	$2.16 \cdot 10^{12}$
Cell 9	-16	$2.76 \cdot 10^{12}$	$2.38 \cdot 10^{12}$	$2.04 \cdot 10^{12}$	$1.65 \cdot 10^{12}$

Table 5. 5: Thermal neutron flux profile along the z axis calculated by Serpent model within the fuel elements in the different positions.

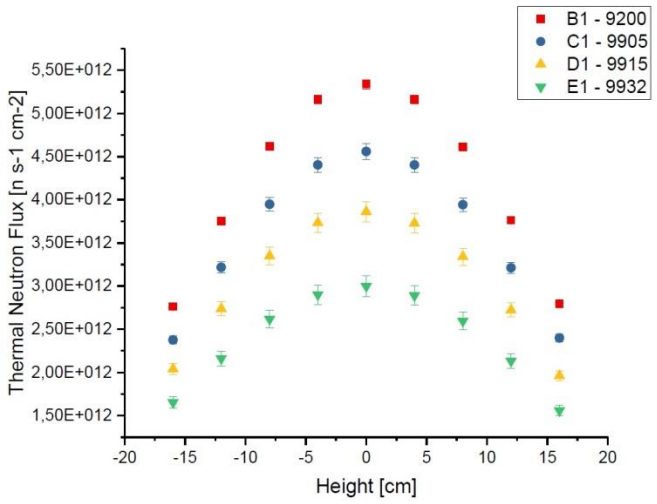

Figure 5. 12: Thermal Flux within different fuel elements (B1, C1, D1, E1) located in various rings obtained by Serpent calculation.

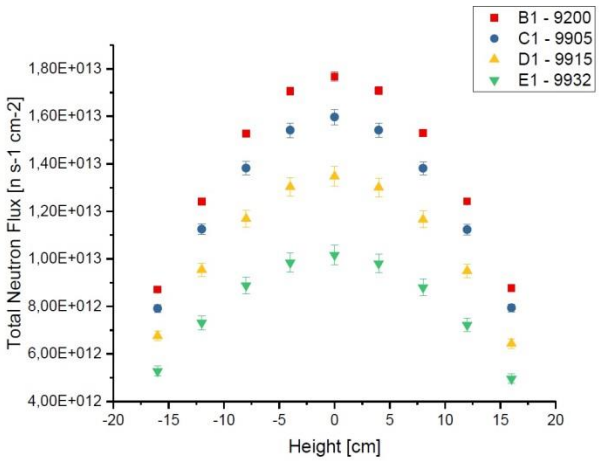

Figure 5. 13: Total Flux within different fuel elements (B1, C1, D1, E1) located in various rings obtained by Serpent calculation.

Conclusion

The comparison of the neutron flux values calculated with the Serpent model with those obtained by MCNP6 model shows a very good agreement.

In the irradiation positions along the radial direction, the maximum difference between Serpent and MCNP6 is below 10%, with lower value in the core centre for both the thermal- (2.5%) and the total-flux (0.5%).

In the irradiation positions along the vertical direction, the maximum difference between the two simulation is below 8%.

When investigating the neutron flux within the fuel elements, the difference between Serpent and MCNP is even lower (<3%), except for the outer cell in the fuel element where 5% difference is reached for the thermal flux.
Hence, the calculation shows that the Serpent model is a valuable tool to simulate the neutron flux in the reactor and can be used for further simulations.

5.3.2. SERPENT transmutation rates and burnup calculation

After verification of Serpent model based on the in-core neutron flux and spectrum behaviour, the second validation step consisted in the evaluation of transmutation rates and fuel burn-up by simulation of the previously described experiments (Chapter 4). The results were then compared with the experimental values.

Serpent simulation for the U/Th transmutation rates experiment

As described in 4.1, experimental data about production and depletion of nuclides in natural Uranium (U) and Thorium (Th) foils were obtained by irradiation in the annular groove irradiation facility (Lazy Susan) at the TRIGA reactor of TU Wien.
The Serpent-2 reactor model extends up to the reactor tank, including the graphite reflector, the horizontal beam tubes and the Lazy Suzan (LS). It was then possible to simulate the irradiation of U and Th foils in the position LS1.
The reactor horizontal and vertical sections of Serpent-2 model are shown in Figure 5.14(a) and 5.15(a) respectively.

In both figures, it can be seen the Lazy Suzan that penetrates the graphite reflector and is filled with water. In the Lazy Susan, five aluminum vertical dry irradiation tubes are installed for irradiation of small samples: the one (named LS1) used for the considered experiment is reproduced in Serpent and is visible in detail in Figures 5.14(b) and 5.15(b). The natural U/Th foil in the irradiation position is represented in red colour.

The simulation options were 1 million source neutrons per cycles, with in total 1500 cycles. To simulate the irradiation, the burn up of the foils material was modelled by Serpent with burn up time of 90 minutes and 5 kW reactor power.

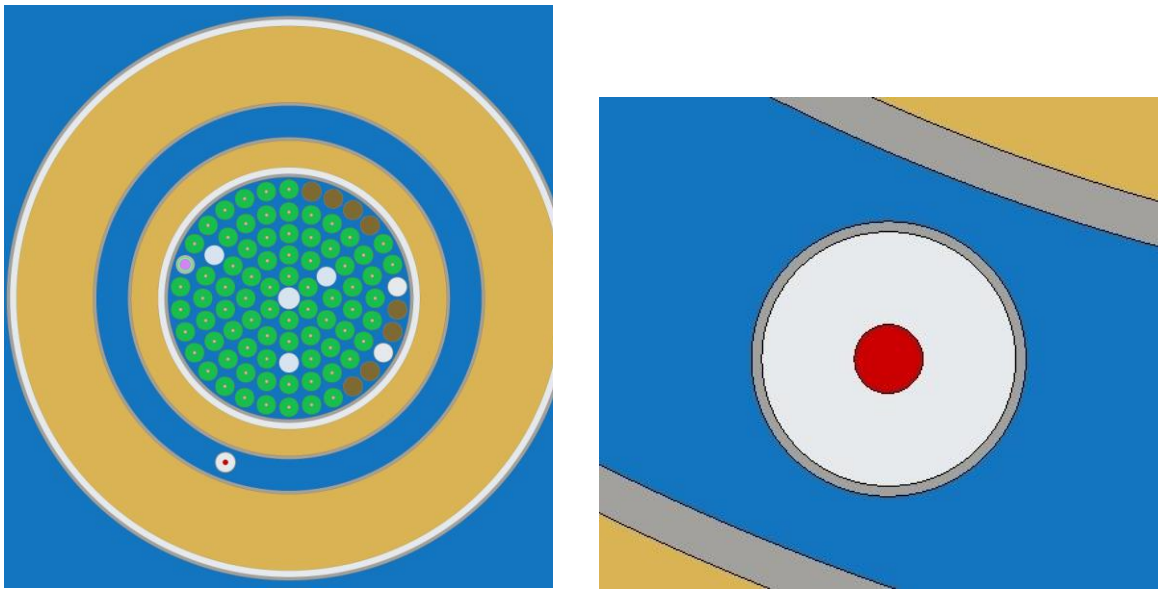

(a) **(b)**

Figure 5. 14: (a) The horizontal section of the TRIGA reactor model as obtained with Serpent-2 and (b) the detail of irradiation facility LS1 used for U and Th foils irradiation.

As Serpent can calculate the activities of every possible generated nuclide, the output requirement included all the nuclides measured in the experiment (see Table 4.7 for U foils and Table 4.8 for Th foils).

Calculated results for the U foil are reported in Table 5.6: Serpent was asked for providing the activity values at both end-of-irradiation time and at measurement time for direct comparison. The comparison of Serpent results against the experimental ones is shown in Figure 5.16.
Similarly, the Th foil calculated results are presented in Table 5.7 and compared to experimental values in Figure 5.17.

In case of the Uranium foils, most Serpent determined activities are in a good agreement with the experimental values: that is, Serpent results are comparable with the measurement results within the uncertainties (< 10%). However, it can be observed that some isotopes have bigger discrepancy between simulation and experimental data. This is the case of Tc-99m, Ce-141, Te-132 and Xe-133: the explanation can be that the gamma lines for detection of those isotopes lay in the low energy region (below 230 keV), where the detector uncertainty is larger.

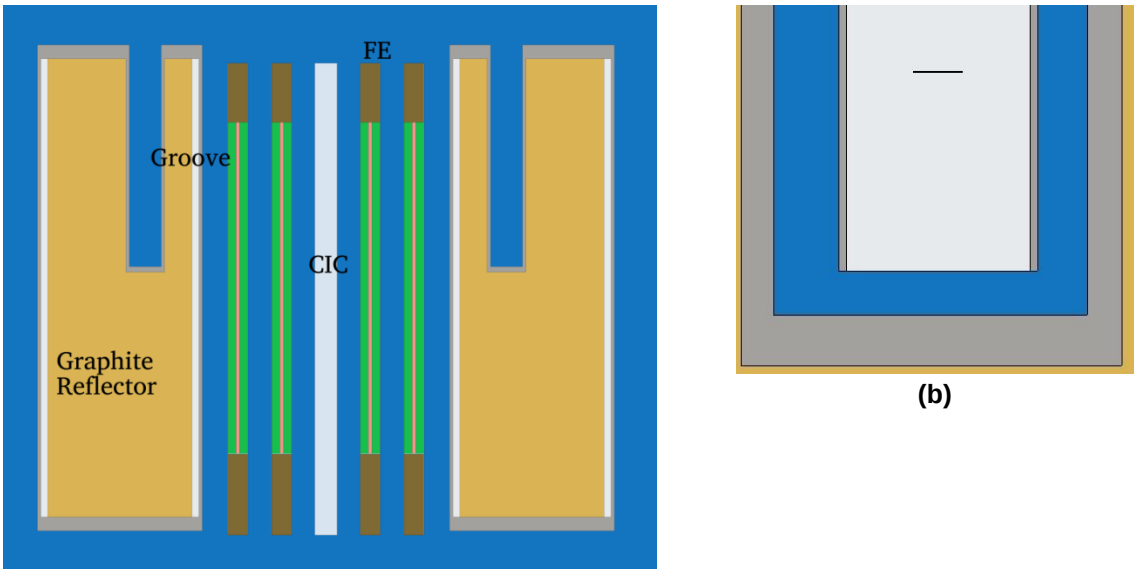

Figure 5.15: (a)The vertical section of the TRIGA core modeled with Serpent-2. (b) detail of irradiated foils in the LS1 irradiation position.

Element	U foil Serpent activity [Bq]			U foil experimental activity [Bq]
	End of irradiation time	Time of measurement		Time of measurement
Ba-140	1.18E+04	6.59E+003		6.95E+03
La-140	2.24E+02	7.45E+003		7.94E+03
Mo-99 c	5.41E+04	3.30E+003		3.59E+03
Tc-99M	3.87E+03	3.20E+003		2.62E+03
Np-239	8.08E+05	4.66E+004		5.75E+04
Ce-141 c	3.14E+02	3.53E+003		2.69E+03
Nd-147	3.92E+03	2.52E+003		2.77E+03
Te-132 c	1.12E+006	2.99E+003		8.73E+03
I-132	8.56E+03	3.08E+003		3.92E+03
I-131	3.03E+03	3.48E+003		3.80E+03
Xe-133	3.75E+02	8.77E+003		6.39E+03
Ce-143	8.14E+04	3.91E+002		4.47E+02
Ru-103	1.87E+03	1.59E+003		1.73E+03
Zr-95 c	2.09E+03	2.23E+003		2.43E+03
Nb-95	1.18E+00	4.67E+002		4.83E+02
Cs-137	1.40E+01	1.40E+01		1.40E+01

Table 5.6: Serpent calculated activity values in U irradiated foils, evaluated at the time of measurement, for each detected nuclide. Experimental activity values refer to average value of all irradiated U foils.

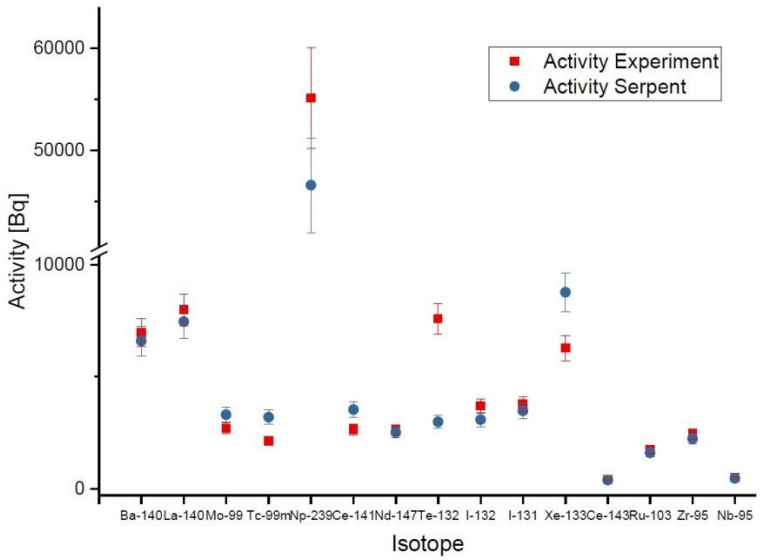

Figure 5.16: Serpent calculated and experimental activity values for the Uranium-foil.

Element	Th foil Serpent activity [Bq]	Th foil experimental Activity [Bq]
Pa-233	9.04×10^4	1.12×10^5
Th-232	4.66×10^2	4.77×10^2
Ba-140	15.40	20.23
La-140	16.60	22.86

Table 5.7: Serpent calculated activity values in Th irradiated foils, evaluated at the time of measurement. Experimental activity values refer to average value of all irradiated Th foils.

In case of the Thorium foils, the Serpent simulation looks less accurate in reproducing the experiment with discrepancy of about 20% for Pa-233, that rises to 33-37% for Ba-140 and La-140. In this case, it has to be noticed that most likely the irradiation was sufficient to induce a detectable transmutation of Th-232 into U-233: nevertheless, the fission reaction of U-233 occurred but produced fission products (as Ba-140, La-140) in very low amount, hardly detectable with the used instrumentation.

In general, when comparing the results of the simulation with experimental data, one must be aware that the simulation can have some inaccuracies. In the present simulation for example, the neutron flux spectrum in out of core region could results not exactly the same as in the reality. Additionally, Serpent burn calculation in thin and small volumes (like the irradiated foils) is not accurate as in larger volumes (like for example in the fuel elements).

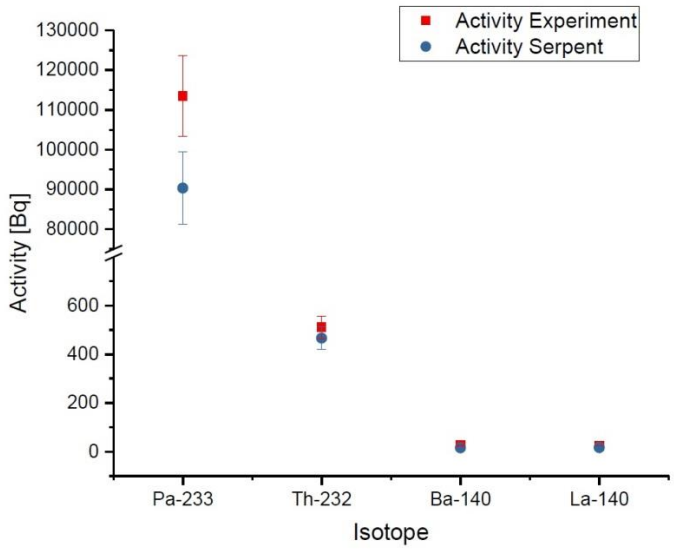

Figure 5. 17: Calculated and experimental activity values for the Thorium-foil.

Serpent simulation for the Fuel Elements experiment

The fuelled experiment described in 4.2 produced experimental data about the fuel inventory following the fuel irradiation during the reactor operation.
Those experimental results are here used for the validation of the Serpent reactor model.

The fuel elements investigated by Serpent calculation and their irradiation history are listed in Table 4.9. It is recalled that all the investigated fuel elements were loaded in the core in the same date and underwent no reshuffling during the considered operational period. In general, the entire core underwent only slight changes during the referenced period (Table 5.8), i.e. from the date of the new core loading (21/01/2013) to the date of reactor shut-down (01/04/2015) due to instrumentation refurbishment works.
The total cumulative work of the reactor in this time interval was 547.841 MWh, as estimated from the handbooks of the reactor operation.

Core	Start date	Core modification	End date	Duration (days)	Cumulative MWh	Operation at 250kW (h)
Core 1	21/01/2013	New core loaded and start of operation	22/07/2013	182	128.86	515.44
Core 2	22/07/2013	Fresh FEs in F15 and F14	04/10/2013	74	198.41	278.20
Core 3	04/10/2013	FEs reshuffle: F2 → F6 F3 → F7 Dummy element → F2,F3	14/04/2014	192	324.74	505.33
Core 4	14/04/2014	FE in F23 removed from core Fresh FE in F23	01/04/2015	352	547.84	892.40
Total	-	-	-	800	547.84	2191.36 (91.31 days)

Table 5. 8: Core modification and irradiation history during the reference period (21/01/2013 - 01/04/2015) for investigated fuel elements.

Serpent Simulation n.1

The first Serpent burn-up simulation was carried out with some simplifications. First of all, the core modifications incurred during the total reference period were simplified; i.e. the four core configurations were collapsed in a unique one corresponding to the one where the operational time was maximum (Core 4). Additionally, it was assumed that the reactor operated continuously at full power (250 kW) till reaching the total cumulative work: i.e. the simulation run in one step at the power of 250kW and duration of 91.31 days. A second step was accounted for the cooling down time elapsed (251 days) from the reactor shut-down till the date of measurement. The simulation calculation was set to 1500 cycles with 1.000.000 source neutron each.

Results were provided in each burned fuel elements (B2, B4, C1, D1, E1): for the main fission products, the total activity in each fuel element at end of the reference period were produced in the output.

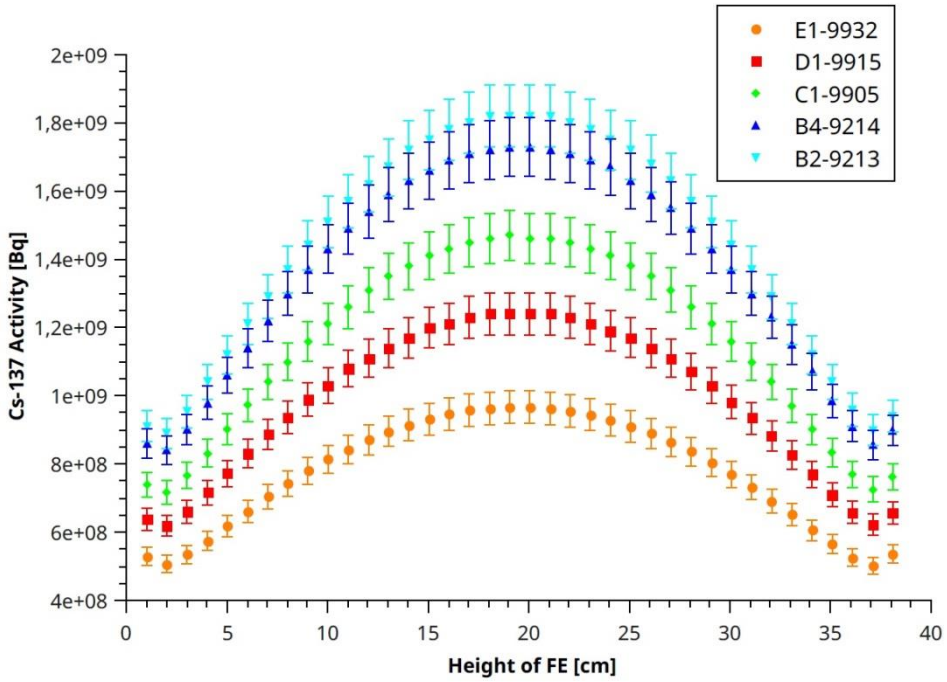

Figure 5.18: Serpent Cs-137 activity distribution along the z-axis inside the five investigated fuel elements.

Besides, each fuel element was divided in 38 cylindrical cells (of 1 cm highness) along the z-axis to obtain the vertical distribution of the activity.

After each burn-up step, Serpent provides an output for all burned materials (in this case the 38 fuel cells) reporting the material composition of all isotopes in atomic density (unit $10^{24}/cm^3$). The total number of a certain nuclide in one cell is then obtained multiplying by the volume of the cell; the activity within the fuel cell can be deducted with equation 2.5.

As an example, the Serpent Cs-137 activity distribution along the z-axis for the five investigated fuel elements is shown in Figure 5.18.

For all the fission products (Cs-137, Ce-144, Ru-103 and Zr-95) detected in the experiment, the results of the simulations are reported in Table 6.2.4. These results were compared with the experimental data (see Table 4.11 and 4.12) as shown in Figures 5.19 and 5.20.

It can be seen that the results of Serpent simulation are in agreement with the experimental values for the isotopes Cs-137, Ce-144 and Ru-103, while Zr-95 results need to be further investigated.

Fuel element		Serpent Activity (Bq)			
Position	**ID**	**Cs-137**	**Ce-144**	**Ru-103**	**Zr-95**
B2	9213	$5.47 \cdot 10^{10}$	$9.64 \cdot 10^{11}$	$1.07 \cdot 10^{10}$	$4.37 \cdot 10^{11}$
B4	9214	$5.19 \cdot 10^{10}$	$9.13 \cdot 10^{11}$	$1.02 \cdot 10^{10}$	$4.10 \cdot 10^{11}$
C1	9905	$4.39 \cdot 10^{10}$	$7.71 \cdot 10^{11}$	$8.65 \cdot 10^{9}$	$3.44 \cdot 10^{11}$
D1	9915	$3.74 \cdot 10^{10}$	$6.57 \cdot 10^{11}$	$7.35 \cdot 10^{9}$	$2.93 \cdot 10^{11}$
E1	9932	$2.94 \cdot 10^{10}$	$5.17 \cdot 10^{11}$	$5.79 \cdot 10^{9}$	$2.30 \cdot 10^{10}$

Table 5. 9: Calculated activity values with Serpent simulation n.1

The activity of Cs-137 in the Serpent simulation is higher for the fuel elements in B2 and B4; while it is lower for the other three elements (C1, D1, E1). The explanation for this is that the history of the various fuel elements is different. The fuel elements in B ring (B2, B4) were fresh fuel elements when loaded in the core at the beginning of the reference period. The fuel elements in the other rings instead (C1,D1,E1) were already slightly irradiated in another reactor till 1989. Caesium (Cs-137) produced till that date is in part still present in those fuel elements; nevertheless the simulation did not take this into account as the fuel composition was provided as for fresh fuel. It is then expected that the "real" (i.e. measured) Cs-137 concentration in these fuel elements is higher than the calculated concentration.

In case of Ce-144, comparing the activities from the measurements with the ones from the simulation the discrepancies of the total activities are for all fuel elements between 5% (B4) and 16% (E1).
In this case the different irradiation history of the fuel elements (previous irradiation in another reactor) does not affect the results. In fact, being the Ce-144 half live of 284.91 days, means that Cerium produced till 1989 is already decayed: therefore the measured activity comes only from Ce-144 produced during the reference period and can be directly compared with the simulation results.

In case of Ru-104, the activities obtained from the Serpent simulation always exceed the experimental ones: the difference goes from 12% in B2 up to a maximum of 20% in the external position E1. The experimental and calculated profiles of activity values along the vertical direction are in the same range even if the experimental data show a considerable fluctuation.

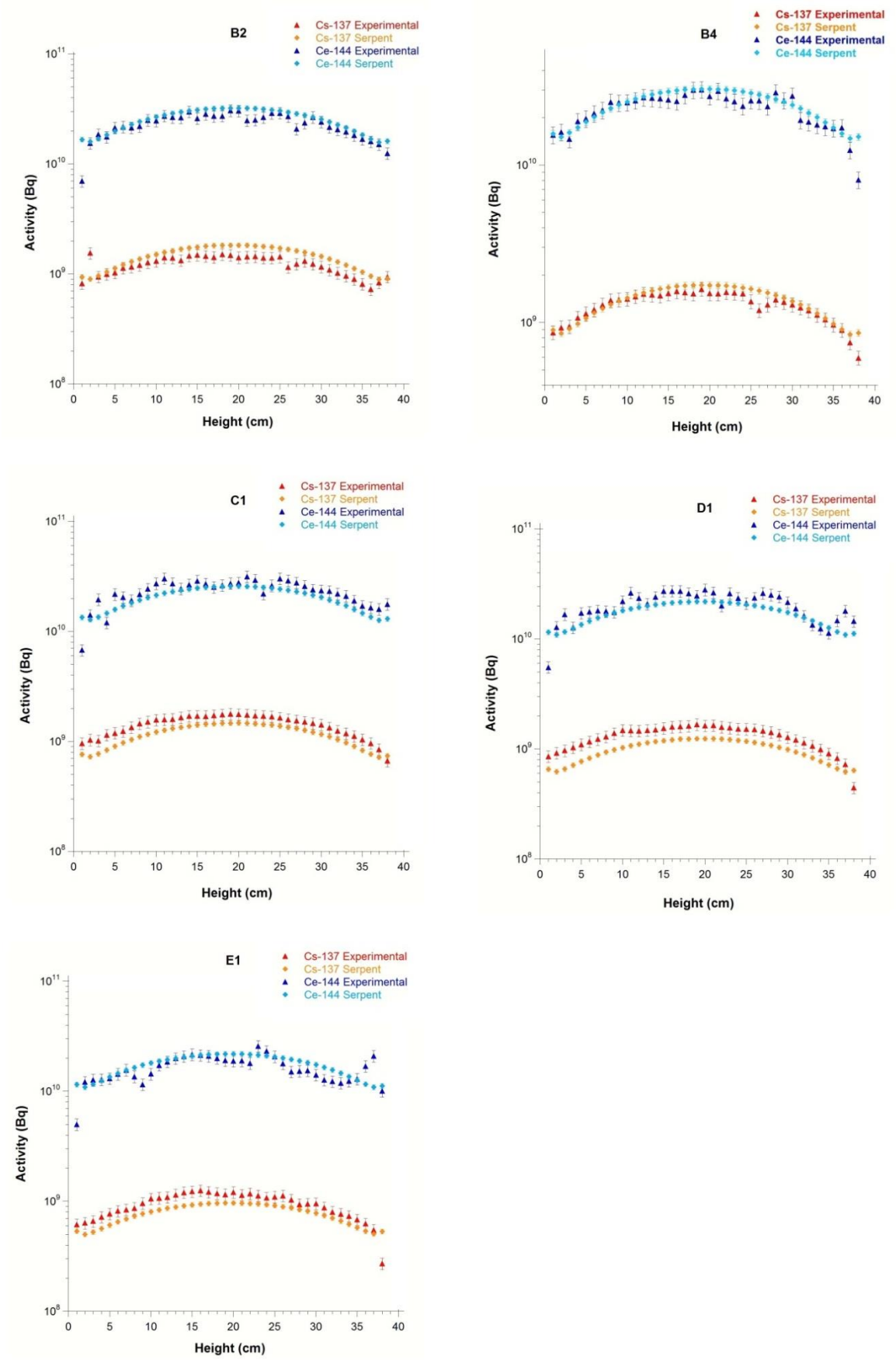

Figure 5. 19: Activity profile (along z axis) of isotopes Cs-137 and Ce-144 in the investigated fuel elements obtained by Serpent calculation and by experimental determination (values referred at time of measurement)

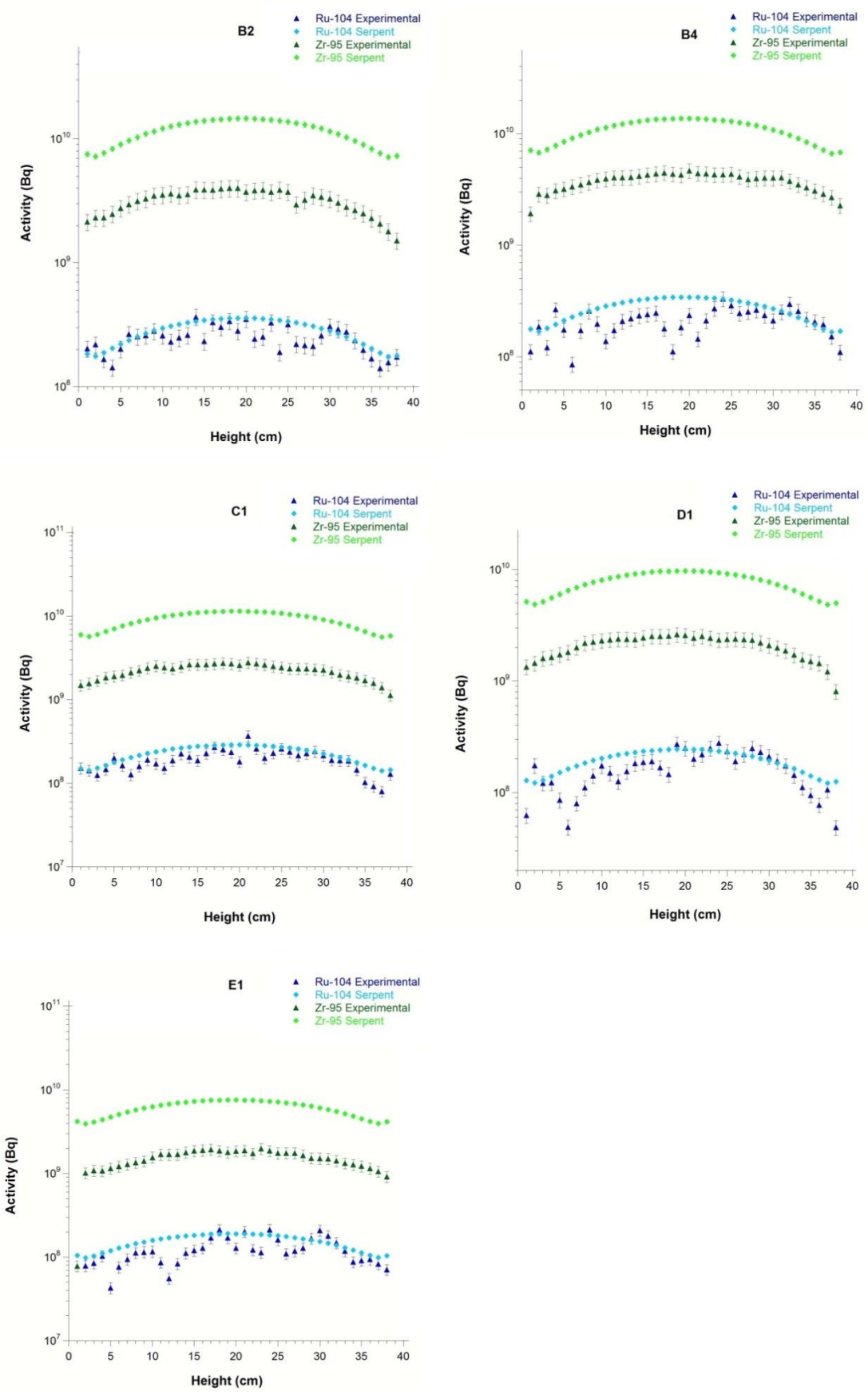

Figure 5. 20: Activity profile (along z axis) of isotopes Ru-104 and Zr-95 in the investigated fuel elements obtained by Serpent calculation and by experimental determination (values referred at time of measurement).

For the fission product Zr-95, this Serpent simulation results are not in good agreement with the experimental values. In fact the simulation sharply overestimates the activity of Zr-95 for all fuel elements. Then it has to be considered that the half live of Zr-95 is 94.91 days, comparable with the burn-up time (91 days) in the performed 1-step calculation. In the reality, this operational time was distributed over a period of about three years, i.e. the produced Zr-95 also decays during the reference period. This effect is not considered in the simulation and the Serpent activity results higher.

Adjustment of the Serpent Simulation for evaluation of short half-life fission product

From the discrepancy of Serpent and experimental results in case of Zr-95, it is clear that in order to evaluate the activity of short half-life (< 100 days) fission products it is necessary to modify the simulation approach. This was done with the next simulations.

Serpent Simulation n.2

A new Serpent simulation was performed considering only the last twelve months of reactor operation before shut-down: the core configuration in this period correspond to Core 4 configuration (Table 5.8). The production of fission product with half-life <100 days (like Zr-95) during the previous operation period was assumed to not significantly contribute to the final results.
The simulation was divided into 6 time intervals, each of 2 month duration. For each time interval, 2 calculation steps were set: one for irradiation (250 kW) and one for decay (0 kW). The number of serpent calculation steps then resulted to be 12.

The duration of the “irradiation” steps was defined by the real operation time in the correspondent 2 months period, while the duration of the “decay” steps was set in order to cover the remaining part of the 2 months interval. Only the last decay step was longer, taking into account the cooling down time till time of measurement. The details of Serpent calculation steps can be found in the Table 5.10.

Time interval	Step	Days	Power (kW)
1	1	8.8	250
2	2	53.2	0
	3	7.9	250
3	4	52.1	0
	5	5.4	250
4	6	55.6	0
	7	6.3	250
5	8	54.7	0
	9	4.1	250
6	10	58.9	0
	11	6.9	250
Cool down	12	251	0

Table 5. 10: Time intervals and calculation steps in the serpent simulation n.2.

Hence, Zr-95 was produced during the time in which the power was set at 250 kW, followed by a time of decay. This build-up and decay behaviour of the total Zr-95 activity during the simulation can be seen in Figure 5.21. The obtained Zr-95 activities at time of the measurement are compared with the experimental values (Table 5.11 and Figure 5.22).

The results from the Serpent simulation can now be considered in fair agreement with the experimental values, being the discrepancies between 15-27 % for the total activity in the different fuel elements.
This difference can be explained by the irradiation history of the simulation. In the simulation the build-up of Zr-95 happens in only few days, while in the remaining time the reactor is turned off. However, this does not correspond to the reality in which the reactor is operating daily for several hours and is only switched off at night and on weekends.

To get more accurate values for isotopes with half-lives like Zr-95, ideally a more detailed irradiation history would be needed: but in this case, a very detail operation history and a much longer calculation time would be required. This is a common limit of burn-up simulation for those reactors that are operated and shut-down on daily basis.

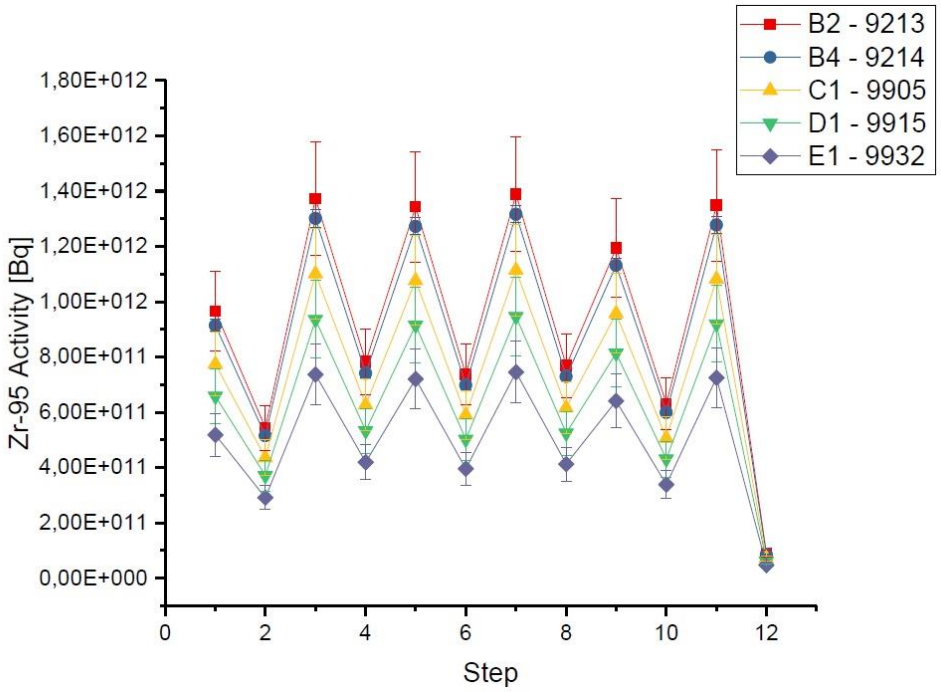

Figure 5. 21: Behaviour of Zr-95 build-up and decay during Serpent simulation n.2 for the fuel elements in the different rings.

	Zr-95 Activity (Bq)		
Fuel element	**Experimental results**	**Serpent *Simulation n.2***	**Serpent *Simulation n.3***
B2	$1.22 \cdot 10^{11}$	$8.91 \cdot 10^{10}$	$9.07 \cdot 10^{10}$
B4	$1.10 \cdot 10^{11}$	$8.44 \cdot 10^{10}$	$8.66 \cdot 10^{10}$
C1	$8.44 \cdot 10^{10}$	$7.14 \cdot 10^{10}$	$7.31 \cdot 10^{10}$
D1	$7.95 \cdot 10^{10}$	$6.08 \cdot 10^{10}$	$6.22 \cdot 10^{10}$
E1	$5.78 \cdot 10^{10}$	$4.78 \cdot 10^{10}$	$4.90 \cdot 10^{10}$

Table 5. 11: activity values obtained by Serpent *Simulation n.2* and *Simulation n.3* compared with the experimental results.

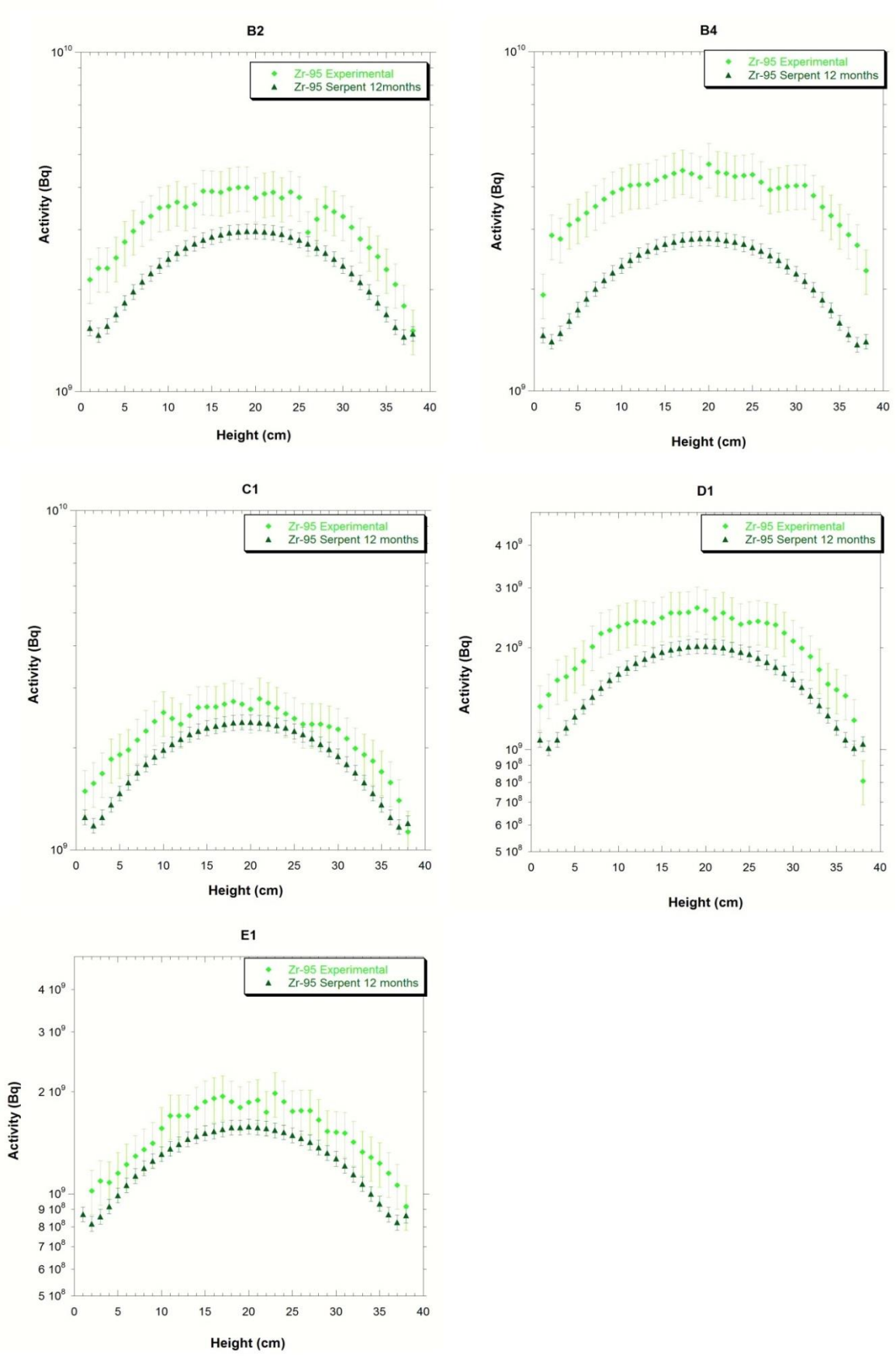

Figure 5.22: Comparison of the Zr-95 activity values obtained by the Serpent *simulation n.2* and the experimental values.

Serpent simulation n.3

Another Serpent simulation was run to refine the calculation approach for Zr-95 and seek the possibility to better estimate its activity.
The irradiation history to take into account was limited to the last 6 months of reactor operation during the reference period. This assumption is justified by the fact that Zr-95 was measured 8 months after reactor shut-down, i.e. after 8 months cooling down time. Hence, at the time of the measurement, Zr-95 produced earlier then the last 6 months of operation was not detectable anymore due to its short half-life.
With the target to faster the Serpent calculation, the considered 6 months of reactor operation were divided into 2 time interval, of 3 months each. As in the previous *simulation n.2*, each time interval was run by Serpent in two calculation steps: one "irradiation" step at 250 kW (for the corresponding real operation time in the interval) and one "decay" step (to cover the remaining part of the 3 months interval). The last decay step included also the cooling down time till time of measurement. In total Serpent provided the fuel composition at the time of the measurement in only 4 steps (instead 1of 2 steps as done in *simulation n.2*).

The new results (Table 5.11 and Figure 5.23) that are slightly closer to the experimental values then the results from *simulation n.2*: the discrepancies are now between 13% (fuel element C1) and 25% (fuel element B2).
This means that, willing to evaluate the activity of fission products with short half-lives (<100days), there is no need to run a very long and detailed simulation with Serpent. The time period to be considered should be about 7 times the reference half-life. The Serpent calculation intervals can typically be set at 3 months of "real time": each interval can then be simulated by 2 calculation steps. The effective operational time of the reactor (during one 3 month interval) can be collapsed in the 1st calculation step, allowing the radioactive decay to take place for the remaining part of the time interval (2nd calculation step).
Considering the assumption and approximation done, among the performed Serpent calculations, *simulation n.3* represents the best choice both for reproducing the experimental values of short half-lives (<100days) fission products and for optimizing the overall calculation time.

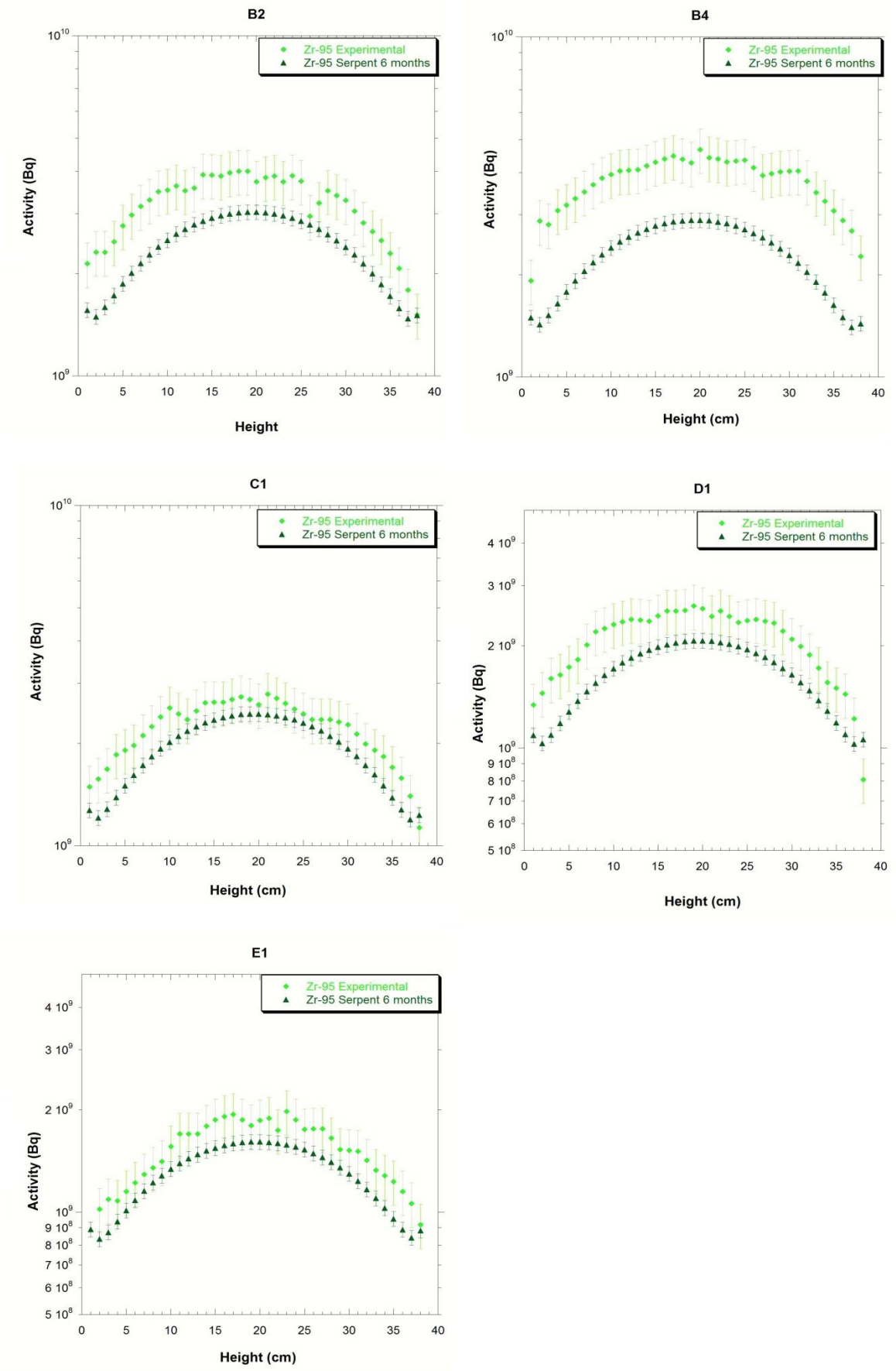

Figure 5. 23: comparison of the Zr-95 activity values obtained by the Serpent *simulation n.3* and the experimental values.

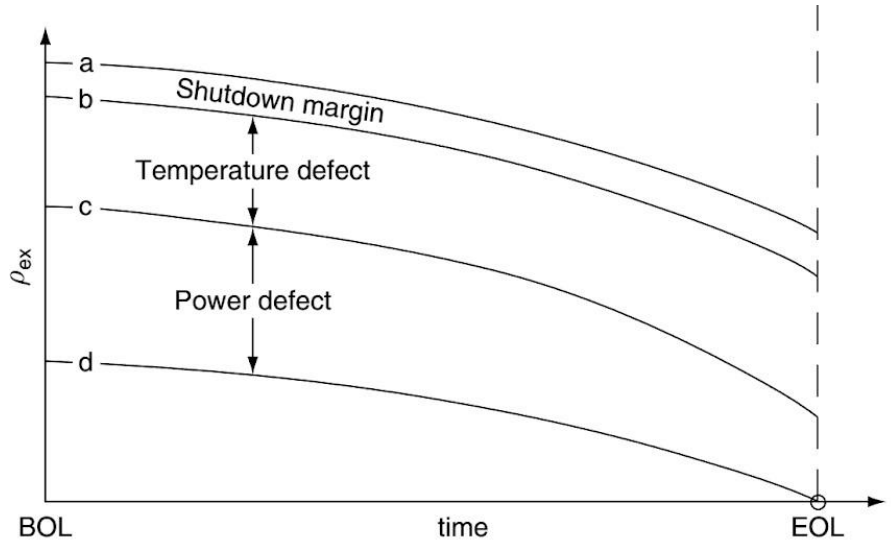

Figure 5. 24: Excess reactivity vs time for different core states. (a) Cold shut-down; (b) cold critical; (c) hot zero power; (d) full power. [53]

5.3.3. Serpent 1st criticality calculation for the new LEU core

The TRIGA reactor of TU Wien with the new fully converted LEU (Low Enriched Uranium) core reached its first criticality on 2013, January 21th (Table 5.8). At this date, the typical nuclear tests and measurement were also performed.

The Serpent reactor model was then utilized to evaluate some of the measured parameters, like the control rods' worth and the excess reactivity (or core excess) value.

Excess reactivity (ρ_{ex}) is defined as the reactivity still available in the core when all movable poisons are removed from the core. The behaviour of excess reactivity in function of the core life time is shown in Figure 5.23[53] in the different core conditions: the shapes of the curves vs time are influenced by fuel depletion and fission products build-up during operation.

The total rods reactivity minus the excess reactivity value is the *shut-down margin*, that is the total amount of reactivity to insert in the core in order to reach the critical condition at zero power.

At the TRIGA reactor of TU Wien the excess reactivity measurement is performed in the clean and cold core condition and reactor critical at 10W power: the REG and SHIM control rods are partially inserted, while the TRANSIENT rod is completely extracted. In occasion of the first criticality on 2013, January 21th, the measured values resulted to be 2.59$ for the *excess reactivity* and 3.21$ for the *shut-down margin*.

For evaluation of the above mentioned parameters with Serpent, criticality calculations were performed in the Core1 configuration. With four different calculations, the k_{eff} was obtained for the following rods configurations:

- TRANS, REG, SHIM fully extracted
- TRANS fully inserted; REG and SHIM fully extracted
- REG fully inserted; TRANS and SHIM fully extracted
- SHIM fully inserted; REG and TRANS fully extracted

The obtained results for k_{eff} and the corresponding reactivity values are shown in Table 5.12.

Configuration	**k_{eff}**	**ρ (PCM)**	**ρ ($)**
TRANS, REG, SHIM fully extracted	1.01985	0.01946	2.67
TRANS fully inserted; REG and SHIM fully extracted	1.00483	0.00480	0.66
REG fully inserted; TRANS and SHIM fully extracted	1.01083	0.01071	1.47
SHIM fully inserted; REG and TRANS fully extracted	1.00113	0.00113	0.15

Table 5.12: k_{eff} and the corresponding reactivity values obtained by Serpent calculation in the different control rods configuration for Core 1.

Consequently, the total reactivity worth of each control rod was deducted and compared with the measured results available from the criticality experiment (Table 5.13). The total worth of the control rods resulted in very good agreement with the experimental values.

	Control rod worth ($)	
Control rod	**Serpent**	**Experiment**
TRANS	2.01	**2.1**
REG	1.20	**1.2**
SHIM	2.51	**2.5**

Table 5.13: Total reactivity worth of each control rod obtained by Serpent calculation and compared with the results from the criticality experiment.

As it can be deducted, the calculated value obtained by Serpent for the *excess reactivity* is 2.67$ (vs. experimental value 2.59$), while for the *shut-down margin* is 3.05$ (vbs. experimental value 3.21$).

Considering that the Serpent model does not take into account materials impurities neither includes the non-saturable poisons (generated by previous irradiation) in the fuel elements composition, it can be concluded that these results reproduce the criticality experiment with very good agreement.

Conclusions

The work performed consisted in the modelling of the TRIGA reactor of the TU Wien with different Monte Carlo calculation codes and in the performance of several experiments at the reactor to obtain a substantial set of data to benchmark Monte Carlo calculation results.

The first set of experiments is related to the determination of neutron flux and neutron spectrum (Chapter 2) at several irradiation positions at the TRIGA reactor. By means of an extensive measurements campaign, different positions were characterized both in- and out-core. The in-core positions were defined along the vertical and radial core axes; the out-core positions extended from the Lazy Susan facility to one of the horizontal beam tubes (Beam Tube B). The measurements were performed adopting a method based on activation of different material foils followed by a flux de-convolution analysis using the iterative code SAND II. Neutron fluxes and neutron energy distribution measurement results subsequently became the data base for the validation of the Monte Carlo calculation models. Additionally, the knowledge of the neutron energy spectrum along the horizontal Beam Tube B was of interest for the study of a new thermal white neutron beam. The experimental data obtained were then utilized as input for the design of the new experimental facility, leading eventually to its installation.

The second set of experiments was related to the evaluation of transmutation rates (Chapter 4) of nuclides relevant for the study and analysis of nuclear fuel composition under irradiation. One experiment consisted in the irradiation of natural Uranium (U) and Thorium (Th) samples in the Lazy Susan irradiation facility. Following irradiation, the transmutation rates (production and depletion) inducted by neutrons were determined by means of gamma-ray spectrometry technique. In conclusion, for the Uranium foils, nearly all predicted fission products were detected and the activity values deducted. In the case of Thorium foils, the transmutation of Th-232 into U-233 was properly detected, while the fission of transmuted U-233 occurred only in limited amount: as a result, some fission products (Ba-140, La-140) were detected in very low amount with the used instrumentation.

Another experiment was the detection of fission products activity distribution along the axial dimension of irradiated fuel elements (FEs) at the TRIGA reactor. Except for the nuclide Cs-137, for all detected fission products (Ce-144, Ru-103 and Zr-95), the experimental results coherently showed how the activity depends on the different positions of the FEs in the core.

As expected, the total activity decreases moving from the inner to the outer core positions. Conversely, in the case of Cs-137, measurement results showed an increase of activity values from (inner) B ring position to (outer) C ring position. This is explained by the fact that the FEs in C, D and E rings were not actually fresh when inserted in the core. They were in fact slightly irradiated (burn-up <1%) in another reactor (period 1985-1989). Considering the time elapsed, those fuel elements can be considered fresh for the detection of short-lived fission products (such as Ce-144, Ru-103 and Zr-95), but not for Cs-137. Thus, the higher value of Cs-137 in the C ring can be explained by the contribution of Caesium produced in the 1980s and still present. Nevertheless, comparing Cs-137 activity results of FEs with a comparable irradiation history (i.e. FEs in C1, D1, E1 core positions), the measured activity values again decrease coherently moving from inner to outer ring core positions.

The MCNP6 TRIGA reactor model was developed (Chapter 3) for the core configuration (fully converted LEU - Low Enriched Uranium) at time of the performed experiments. The current model included, at the proper level of detail, all the components that can affect the evaluation of the in-core neutron flux distribution and the energy spectrum in different in-core positions as well as the reactor fuel burn-up and reactor critical parameters. The developed MCNP6 reactor model was used to calculate the neutron flux and neutron spectrum in the in-core and out-core positions that were characterized by the neutron flux and neutron spectrum measurement campaign.

For the 14 in-core irradiation positions, the comparison of results from the MCNP6 simulation and from the measurement show a good agreement within the experimental uncertainties (<9%). This is found both in comparing calculated with experimental neutron energy spectra as well as comparing specific neutron spectrum components (like thermal- and total-flux). As verified for the experimental values, the distribution of total- and thermal-fluxes calculated with MCNP6 along the vertical axis of the core shows a typical cosine behavior.

Among the out-core positions, the horizontal Beam Tube B was considered for MCNP6 calculations. Since from original data and drawings of the reactor, it was not clear if the Beam Tube B faces the graphite or a cavity in correspondence of the reflector, one of the purposes of the present evaluation was also to clarify this issue. The MCNP calculation in the horizontal Beam Tube B and subsequent comparison with experimental values shows that, while the simulation with the full graphite reflector is 2 times lower than the experimental values, the MCNP6 calculation performed with the empty volume in the graphite reflector best estimates the experimental neutron energy distribution. In this second case in fact, MCNP6 results are 9.7% lower than the experimental ones (referring to the thermal flux

component): this result can be considered a good achievement and indicates that, most likely, the Beam Tube B at TRIGA Vienna reactor faces an empty volume in the graphite reflector.
Also for the other out-of-core position, the Lazy Susan (LS1) position, MCNP calculated values underestimate (about 10% in the thermal region) the experimental ones. This result is considered valuable for the proper characterization of the LS1 irradiation position. In fact, the LS1characterization in terms of neutron flux was of interest because of its utilization in the irradiation of natural Uranium and Thorium foils. As those irradiations aimed to generate fission products in fissile materials, then, the thermal spectrum component is the most relevant.
Based on the above considerations, the new reactor model developed in MCNP6 was tested and benchmarked against experimental results (flux values and neutron energy spectra) in several irradiation positions, both in-core and out-core. In such a way, the MCNP6 model is validated and could be used to evaluate the neutron flux and spectrum in other reactor regions where a direct measurement is not possible, like for example inside the fuel elements.

As done with MCNP6, the Serpent-2 code was used to develop a new model of the TRIGA reactor. The validation of the Serpent-2 model was carried out in two steps.
The first step consisted in reproducing the neutron flux and neutron energy spectrum with Serpent at each position previously characterized by experimental measurement and by MCNP6 calculation. Additionally, the neutron flux was evaluated with Serpent within selected fuel elements. Serpent results were then benchmarked against the values obtained with the validated MCNP6 model.
The second step of the validation procedure consisted in the utilization of the Serpent-2 model to calculate the neutron-induced transmutation rates in uranium and thorium target foils and in irradiated fuel elements (FEs) under the same irradiation conditions of the measurements performed in Chapter 4. The obtained results were then compared with the experimental values to evaluate the capability of Serpent-2 model to reproduce the core behavior during irradiation/operation.
For the neutron flux evaluation, the comparison of the neutron flux values calculated with Serpent-2 and those obtained by the MCNP6 model shows a very good agreement. In the irradiation positions along the radial direction, the maximum difference between Serpent and MCNP6 is below 10%, with lower discrepancy in the core center for both the thermal- (2.5% difference) and the total-flux (0.5% difference). In the irradiation positions along the vertical direction, the maximum difference between the two simulations is below 8%. When

investigating the neutron flux within the fuel elements, the maximum difference between Serpent and MCNP6 is even lower (<3%), except for the external part of the fuel rod where 5% difference is reached for the thermal flux. Hence, the calculation shows that the Serpent model is a valuable tool to simulate the neutron flux in the reactor and can be used for further simulations.

For the transmutation rate evaluation, the first experiment of natural Uranium and Thorium sample irradiation was reproduced with Serpent. In case of the Uranium foils, most Serpent determined activities are in a good agreement with the experimental values: that is, Serpent results are comparable with the measurement results within the uncertainties (below 10%). In case of the Thorium foils, the Serpent simulation is still in fair agreement with the experimental results but with higher discrepancy (about 20% for Pa-233 and 30% for Ba-140 and La-140). In this case, it has to be noticed that some of the evaluated activities present very low absolute values and this explains the lower precision in the calculated and the experimental data.

The second transmutation rate evaluation performed with Serpent-2 was related to the fuel composition modification under irradiation. The irradiation of the investigated FEs was simulated starting from the new core loading (21/01/2013) to the date of reactor shut-down (01/04/2015), then cooling down was calculated to the date of measurement (December 2015). Some simulation simplification were assumed: e.g. the four core configurations during the referenced period were collapsed in a unique one corresponding to the one where the operational time was maximum; the core configuration at the date of first criticality was set with all fresh fuel elements, even if this does not exactly correspond to the reality, since major part of FEs were slightly irradiated (burn-up <1%) in another reactor (1985-1989). For each nuclide, results were provided in the investigated fuel elements (B2, B4, C1, D1, E1) as total activity and as axial profile along the z-axis (each fuel element was divided in 38 cylindrical cells, each of 1 cm height) for a fine comparison with the experimental data.

For all the fission products (Ce-144, Ru-104, Zr-95) considered for comparison with experimental data, except Cs-137, the different irradiation history of the fuel elements (previous irradiation in another reactor) does not affect the results. In fact, considered their half-lives, the respective quantities produced till 1989 are already decayed: therefore the measured activities derives only from the production at the TRIGA reactor of TU Wien and can be directly compared with the simulation results. As expected, for the long half-life nuclide Cs-137, the Serpent-2 concentration in C1, D1, E1 fuel elements is lower than the experimental concentration.

In conclusion, the comparison showed a good agreement between calculation and measurement results, with differences from 5% to maximum 20%: this result validates the methodology for the evaluation of the burn-up of the FEs.

In case of Zr-95, a specific simulation approach was needed due to its short half-life ($T_{1/2}$ = 64 days). Ideally, to obtain more accurate values for isotopes with half-lives like Zr-95, a more detailed irradiation history would be needed: nevertheless, a very detailed operation history and a much longer calculation time would be required. This is a common limit of burn-up simulation for those reactors that are operated and shut-down on daily basis, like the TRIGA reactor. The conclusion was that, willing to evaluate the activity of fission products with short half-lives (<100days), there is no need to run a very long and detailed simulation with Serpent. According to the performed calculation, the time period to be considered should be about 7 times the reference half-life. The Serpent calculation intervals can typically be set at 3 months of "real time": each interval can then be simulated by 2 calculation steps. The effective operational time of the reactor (during one 3 month interval) can be collapsed in the 1st calculation step, allowing the radioactive decay to take place for the remaining part of the time interval (2^{nd} calculation step). Considering the assumption and approximation done, among the performed Serpent calculations, this approach represented the best choice both for reproducing the experimental values of short half-lives (<100 days) fission products and for optimizing the overall calculation time.

Finally, the validated Serpent-2 reactor model was used to evaluate the critical parameters of the first LEU core configuration of the TRIGA reactor. For this calculation, the composition of previously irradiated FEs was updated according to the declared fuel burn-up (<1%). The calculation provided evaluation of the following parameters:

- Control rods worth:
  - TRANSIENT rod: 2.01$ (vs. experimental value 2.1$);
  - REGULATING rod: 1.20$ (vs. experimental value 1.2$);
  - SHIM rod: 2.51$ (vs. experimental value 2.5$);
- *Excess reactivity*: 2.67$ (vs. experimental value 2.59$);
- *Shut-down margin*: 3.05$ (vbs. experimental value 3.21$).

Considering that the Serpent-2 model does not take into account materials impurities neither includes the non-saturable poisons (generated by previous irradiation) in the fuel composition, it can be concluded that these results reproduce the criticality experiment with very good agreement.

List of Figures:

Bibliography

[1] John R. Lamarsh, Introduction to Nuclear Reactor Theory, Addison-Wesley Publishing Company, New York, 1972.

[2] Weston M. Stacey, Reactor Safety, in Nuclear Reactor Physics, Second Edition, Wiley-VCH Verlag GmbH Co. KGaA, Weinheim, 2007.

[3] http://www.ga.com/triga

[4] GA, "100-kW TRIGA Mark II Pulsing Reactor Mechanical Maintenance and Operational Manual," General Atomics, USA, 1962.

[5] G. Atomics, "Shipment documents from General Atomics," GA, USA, 1962-1988.

[6] General Atomic (GA), March 1964, TRIGA Mark II Reactor General Specifications and Description. General Atomic Company, U.S.A.

[7] R.H. Filby. *Isotopic and Nuclear Analytical Techniques in Biological Systems: A Critical Study - Part IX. Neutron Activation Analysis* (Technical Report). Pure & Appl. Chem., Vol.67, Co. 11:pp1929_1941, 1995.

[8] H. Böck. *Neutron Activation Foil Manual*, 1989. AIAU 89306.

[9] RSICC COMPUTER CODE COLLECTION - *SAND II Neutron Flux Spectra Determination by Multiple Foil Activation - Iterative Method*, Oak Ridge National Laboratory.

[10] A. Borio di Tigliole, A. Cammi, M. Clemenza, V. Memoli, L. Pattavina, E. Previtali, *Benchmark evaluation of reactor critical parameters and neutron fluxes distribution at zero power for the TRIGA Mark II reactor of the University of Pavia using the Monte Carlo code MCNP, (2010) Progress in Nuclear Energy 52(5),* pp. 494 – 502.

[11] Karl-Heinrich Beckurts, Karl Wirtz, *Neutron Physics*, Springer-Verlag Berlin Heidelberg GmbH 1964.

[12] D. Alloni, A. Borio di Tigliole, J. Bruni, M. Cagnazzo, R. Cremonesi, G. Magrotti, M. Oddone, F. Panza, M. Prata, A. Salvini, *Neutron flux characterization of the SM1 sub-critical multiplying complex of the Pavia University*, (2013) *Progress in Nuclear Energy 67*, pp. 98-103.

[13] RSICC COMPUTER CODE COLLECTION – *MCNP6 Monte Carlo N-Particle Transport Code System Including MCNP6.1, MCNP5-1.60, MCNPX-2.7.0 and Data Libraries,* Los Alamos National Laboratory and Oak Ridge National Laboratory.

[14] W.Mach et Alt., Installation of a Thermal White Neutron Beam Facility at the TRIGA Reactor in Vienna, 26th International Conference Nuclear Energy for New Europe (NENE), Bled-Slovenia, September 11-14, 2017.

[15] J.S. Hendricks & R.E. Prael, *Monte Carlo Next-Event Estimates from Thermal Collisions*, Nuclear Science and Engineering, 109(3), October 1991

[16] J.S. Hendricks, *MCNP S(a,b) detector scheme*, Los Alamos National Laboratory Report, LA-11952 (October 1990)

[17] R.C. Little, R.E. Seamon, Neutron-induced photon production in MCNP, Los Alamos National Laboratory Report LA-UR-83-1123 (Proceedings of the Sixth International Conference on Radiation Shielding Vol1, 151; Tokyo (Japan) 1983).

[18] F. B. Brown, "Fundamentals of Monte Carlo Particle Transport," Los Alamos National Laboratory report LA-UR-05-4983 (2005).

[19] S. Nakamura, Computational Methods in Engineering and Science, R. E. Krieger Publishing Company, Malabar, FL (1986).

[20] M. Cagnazzo, T. Stummer, M. Villa, and H. Böck. Validation of the MCNP6 Model at the Atominstitut TRIGA Reactor. In Research Reactor Fuel Management Conference (RRFM), 2015.

[21] CANBERRA Industries Inc. Genie 2000 Spectroscopy Software Customization Tools.CANBERRA Industries Inc., 3.1 edition.

[22] M. Verpelli A. L. Nichols, D. L. Aldama. Handbook of Nuclear Data for Safeguards:Database Extensions, August 2008. INDC, IAEA, 2008].

[23] Modern nuclear chemistry, W.Loveland, D.J. Morrissey, G.T. Seaborg, 2006 (Wiley).

[24] Böck H., Hammer, J., 1981. Gamma spectrometry of TRIGA fuel elements. Atomkernenergie, Kerntechnik. 39(3): 195.

[25] Böck H. et al., 2011. Gamma spectrometry inspection of TRIGA Mark-II Fuel using caesium isotopes. Nuclear Engineering and Design, 241(1): 118-123.

[26] MCA-527 Digital Multi-Channel Analyzer – User Manual. 2012-08-07, GBS Elektronik GmbH, Germany.

[27] 2012. WinSpec Spectroscopy Software. 4411-0048, Version 2.6B. December 11, 2012 Princeton Instruments.

[28] Böck H., Ashoub N., 1993. Gamma Spectrometry of TRIGA FLIP Fuel Elements, Regional Meeting: Nuclear Energy In Central Europe: Present and Perspectives, Portoroz, Slovenia.

[29] National Nuclear Data Center, Brookhaven National Laboratory. http://www.nndc.bnl.gov/ (accessed April 2017)

[30] 2016. Monographie BIPM-5, Table of Radionuclides (Vol. 8 – A = 41 to 198). Pages 191-198. Bureau International des Poids et Mesures, Pavillon de Breteuil, F-92310 Sevres.

[31] Nuclear Data Center, Japan Atomic Energy Agency (JAEA). http://wwwndc.jaea.go.jp/jendl/j40/j40.html, (accessed April 2017).

[32] IAEA-TECDOC-1401, 2004. Quantifying uncertainty in nuclear analytical measurements. Pages 103-126. International Atomic Energy Agency (IAEA).

[33] Barrera M. et al., 2017. Precise determination of HPGe detector efficiency for gamma spectrometry measurements of environmental samples with variable geometry and density. NUKLEONIKA 62(1): 47-59.

[34] D. Eichleitner. Nuclide Determination of TRIGA Fuel Elements by Gamma Spectroscopy. Bachelorthesis, Technische Universität Wien, 2015.

[35] D. Eichleitner, M. Cagnazzo, M. Villa, and H. Böck. Nuclide Determination of TRIGA Fuel Elements by Gamma Spectroscopy. In Research Reactor Fuel Management Conference (RRFM), 2016.

[36] Cagnazzo M., Borio di Tigliole A., Böck H., Villa M., Fission products detection in irradiated TRIGA fuel by means of gamma spectroscopy and MCNP calculation, Appl Radiation and Isotopes 135C(2018), 123-130 (in progress).

[37] J. Leppänen. Serpent - a Continuous-energy Monte Carlo Reactor Physics Burnup Calculation Code User's Manual, VTT Technical Research Centre of Finland, June 18, 2015.

[38] J. Leppänen. Introduction in SERPENT. http://montecarlo.vtt.fi/index.htm last Accessed: 2018 Jannuary, 15.

[39] J. Leppänen. Development of a New Monte Carlo Reactor Physics Code. PhD thesis, Helsinki University of Technology, 2007. ISBN 978-951-38-7019-5 (URL: http://www.vtt.fi/publications/index.jsp) Copyright © VTT Technical Research Centre of Finland 2007.

[40] Leppänen, J., et al. (2015) "The Serpent Monte Carlo code: Status, development and applications in 2013." Ann. Nucl. Energy, 82 (2015) 142-150.

[41] Woodcock, E. R., Murphy, T., Hemmings, P. J. and Longworth, T. C. (1965) "Techniques used in the GEM code for Monte Carlo neutronics calculations in reactors and other systems of complex geometry." ANL-7050, Argonne National Laboratory, 1965.

[42] Leppänen, J. (2017a) "On the use of delta-tracking and the collision flux estimator in the Serpent 2 Monte Carlo particle transport code." Ann. Nucl. Energy, 105 (2017) 161-167.

[43] Becker, B., Dagan, R. and Lohnert, G. (2009) "Proof and implementation of the stochastic formula for ideal gas, energy dependent scattering kernel." Ann. Nucl. Energy, 36 (2009) 470-474.

[44] Leppänen, J. (2009b) "Two practical methods for unionized energy grid construction in continuous-energy Monte Carlo neutron transport calculation." Ann. Nucl. Energy, 36 (2009) 878-885.

[45] Leppänen, J. and Isotalo, A. (2012a) "Burnup calculation methodology in the Serpent 2 Monte Carlo code." In proc. PHYSOR 2012, Knoxville, TN, Apr. 15-20, 2012.

[46] Viitanen, T. (2009) "Implementing a Doppler-preprocessor of cross section libraries in reactor physics code Serpent." M.Sc. Thesis, Helsinki University of Technology, 2009.

[47] Kaltiaisenaho, T. (2016) "Implementing a photon physics model in Serpent 2." M.Sc. Thesis, Aalto University, 2016.

[48] Fridman, E., Shwageraus, W. and Galperin, A. (2008b) "Efficient generation of one-group cross sections for coupled Monte Carlo depletion calculations." Nucl. Sci. Eng., 159 (2008) 37-47.

[49] Cetnar, J. (2006) "General solution of Bateman equations for nuclear transmutations." Ann. Nucl. Energy, 33 (2006) 640-645.

[50] Pusa, M. and Leppänen, J. (2010) "Computing the matrix exponential in burnup calculations." Nucl. Sci. Eng., 164 (2010) 140-150.

[51] M.Cagnazzo et al., “Serpent-2 reactor model validation at the Vienna Triga Mark II reactor”, Proceedings of European Research Reactor Conference (RRFM), 14-18 May 2017 in Rotterdam, Netherlands.

[52] H. Herzog Master Thesis “Development and Validation of a Serpent-2 model for the TRIGA Mark II reactor of the Technical University Vienna“, University of Vienna, April 2017.

[53] E.E.Lewis, Fundamentals of Nuclear Reactor Physics, © 2008 Elsevier Inc.

Pubblications and academic activity

Pubblications (related to the present thesis work):

Cagnazzo M., Borio di Tigliole A., Böck H., Villa M., *Fission products detection in irradiated TRIGA fuel by means of gamma spectroscopy and MCNP calculation*, Appl Radiation and Isotopes 135C(2018), 123-130 (in progress)

M.Cagnazzo et al., "*Serpent-2 reactor model validation at the Vienna Triga Mark II reactor",* Proceedings of European Research Reactor Conference (RRFM), 14-18 May 2017 in Rotterdam, Netherlands. © 2017 European Nuclear Society, Brussels, Belgium

D. Eichleitner, M. Cagnazzo, M. Villa, and H. Böck. *Nuclide Determination of TRIGA Fuel Elements by Gamma Spectroscopy*. Proceedings of Research Reactor Fuel Management Conference (RRFM), 2016, Berlin, Germany; 13-17 March; © 2016 European Nuclear Society, Brussels, Belgium; ISBN 978-92-95064-25-6

M. Cagnazzo, T. Stummer, M. Villa, and H. Böck. *Validation of the MCNP6 Model at the Atominstitut TRIGA Reactor*. Proceedings of Research Reactor Fuel Management Conference (RRFM), 2015, Bucarest, Romania, 19-23 April. © 2015 European Nuclear Society, Brussels, Belgium; ISBN 978-92-95064-23-2

Cagnazzo M., Raith C., Villa M., Böck H., *Measurements of the In-Core Neutron Flux Distribution and Energy Spectrum at the Triga Mark II Reactor of the Vienna University of Technology/Atominstitut*, Proceedings 23rd International Conference Nuclear Energy for New Europe - NENE 2014, Portoroz, Slovenia, September 8-11; © 2014 Nuclear Society of Slovenia; ISBN 978-961-6207-37-9

M. Cagnazzo, Raith C., T. Stummer, M. Villa, and H. Böck; *Measurements of neutron flux distribution and energy spectrum in the horizontal beam tube at the TRIGA MARK II reactor Vienna*, Proceedings of Research Reactor Fuel Management Conference (RRFM), 2014, Lubljana, Slovenia, 30March-3April. © 2014 European Nuclear Society, Brussels, Belgium; ISBN 978-92-95064-20-1

Other publications:

I am author of 26 international publications including articles in international journal, conferences proceedings with referee systems and reports. Out of these 26 publications, 7 are articles of International Journal; 18 are conference publications with referee system; 1 is the IAEA Safety Report Series n.75-*Implementation of a Management System for Operating Organization of Research Reactor* (2013).

Supervisor for the following thesis:

- MSc. Thesis *Development and Validation of a Serpent-2 model for the TRIGA Mark II reactor of the Technical University Vienna*, H. Herzog, University of Vienna, April 2017.

- Bachelor Thesis *Nuclide Determination of TRIGA Fuel Elements by Gamma Spectroscopy*, D. Eichleitner, Technische Universität Wien, November 2015.
- Bachelor Thesis Determination of changes in the composition of natural Uranium and Thorium samples by irradiation at the Triga Mark II research reactor at the Atominstitut-Vienna, S. Dal Cin, Technische Universität Wien, October 2015.
- MSc. Thesis *Neutron Activation Analysis Measurement in Different Energy Ranges at the TRIGA Mark II Reactor for Determination of the Neutron Spectrum*, C.Raith, Technische Universität Wien, May 2015

Other academic activities:

- Co-tenure of the course on *Nuclear Risk and Nuclear Emergency Management* in the post graduated Master on Risk and Emergency Managementat the IUSS (University Institute for Advanced Study, Pavia, Italy) – Academic Year 2012/2013 – 2013/2014
- Lecturer in the post graduated Master on *Nuclear and Ionising Radiations Technologies* (NIRT) at the IUSS (University Institute for Advanced Study, Pavia, Italy)– Period: 2005/2006 - 2006/2007 – 2008/2009 – 2009/2010 – 2012/2013

Conferences with oral presentation (during the present thesis work):

- Oral presentation at *Research Reactor Fuel Management Conference* (RRFM), 2018, Munich, Germany, 12-14 March.
- Oral presentation at *European Research Reactor Conference (*RRFM), 14-18 May 2017 in Rotterdam, Netherlands.
- Oral presentation at *Research Reactor Fuel Management Conference (RRFM),* 2015, Bucarest, Romania, 19-23 April.
- Oral presentation at *RRFM 2014 European Research Reactor Conference*, 30 March – 3 April, Ljubljana (Slovenia)
- Oral presentation at *23rd International Conference Nuclear Energy for New Europe* - NENE 2014, Portoroz, Slovenia, September 8-11

International meetings (during the present thesis work)::

- 1st Research Coordination Meeting (RCM) of the CRP T12029 "*Benchmarks of Computational Tools against Experimental Data on Fuel Burnup and Material Activation for Utilization, Operation and Safety Analysis of Research Reactors*" Vienna International Centre, Vienna, Austria, 13-17April 2015
- September 2017: invitation at the IAEA *Consultancy Meeting International Nuclear Management Academy Steering Committee and Advisory Board* , 25 - 27 September 2017, Vienna, Austria.
- November 2016: invited speaker at *Training Workshop on Integrated Management System for Research Reactors,* IAEA Headquarter, Vienna, 14 - 18 November 2016.
- April 2014: invitation to assist IAEA in the *Consultancy Meeting To explore the collaboration on implementation of Virtual Nuclear Management University*, 28 - 30 April 2014, Vienna, Austria.

- March 2014: Consultant at IAEA *Consultancy Meeting on Development of a CRP on 'Innovative Methods in Research Reactor Analysis: Benchmarks against Experimental Data on Fuel Burn-up and Material Activation*, Vienna, 24-28 March 2014.
- November 2014: invited speaker at *Training Workshop on the Implementation of a Management System for Research Reactor Operating Organizations*, 24-28 November 2014, IAEA, Vienna, Austria.

Acknowledgements

Foremost, I would like to express my deepest gratitude to my advisor Prof. Helmuth Böck for the continuous support and guidance during my Ph.D study and research, as well as for his sincere friendship over these years.

The same gratitude also goes to Dr. Mario Villa, in particular for having sustained me in all the experimental parts of this work and for the stimulating exchange of opinions and information, as well as for his sincere friendship over these years.

My warmest thanks goes to all the staff of the Atominstitut for the availability and patience in accommodating my requests and in helping me with anything I needed during my stay at the institute.

A special thanks to the students that I have supervised during the period of my Ph.D. (in particular Christina, Sandro, Daniel and Henriette) for their dedication and commitment in their studies, and also for their patience in considering all my advises and requests. It was my pleasure to work with all of them!

My acknowledgement goes also to the University of Pavia for having given me the opportunity to conduct this Ph.D. study and achieve an important result for both my personal and professional growth.

My warmest thanks to Dr. Andrea Rappoldi from the Italian Institut of Nuclear Physics for his help and advise in addressing software issues relevant for the analysis of same experimental data.

Thanks to my husband, Andrea, who not only was a constant source of support and encouragement during this study but also provided me with considerable scientific advice for the successful completion of this work.